An Open Source Engine for the Processing of Electron Backscatter Patterns

Philippe T. Pinard

Department of Mining and Materials Engineering
McGill University

A thesis submitted to McGill University in partial fulfilment of the requirements of the degree of Master of Engineering

Montreal, October, 2010

Contents

Abstract

Electron backscatter diffraction (EBSD) is a recognized characterization technique for the scanning electron microscope. Over the last quarter century, several major advancements improved this technique and expanded its applications to the fields of materials engineering and geological science. These improvements have been primarily related to the commercialization of EBSD systems. With their conviviality and ease of use, these systems have reached a broad audience and have contributed to the maturation of EBSD. However, from another perspective, they have also limited the development by the EBSD community: researchers facing atypical problems do not have the opportunity to modify and improve commercial systems to meet their specific needs. Innovation is left to the scientists and engineers working at EBSD companies. This work offers a solution to this problem by the development of an open source, freely available software, EBSD-Image, for processing of diffraction patterns acquired by an EBSD system.

Built on top of image analysis software, EBSD-Image provides a flexible and structured interface to implement new algorithms to process and extract information from diffraction patterns. Two applications are given to demonstrate the analytical benefits of the software. In one application, the calculation of different metrics to evaluate diffraction quality led to a more accurate characterization of the microstructure of Zr-2.5Nb pressure tubes. In the other, quantitative measurements of the deformation induced during metallographic specimen preparation were made, in addition to the development of a new quality metric to assess the deformation level in a sample.

Furthermore, this work presents tools to validate new algorithms via the generation of simulated diffraction patterns as well as utilities to process and analyze large data sets on a distributed computing grid. Two file formats are introduced to provide a more practical way of processing large numbers of diffraction pattern image files and to share the results of an analysis. Finally, an equation linking the two resolutions of the Hough transform for diffraction patterns of any size and a method to remove artifacts created by vertical Kikuchi bands in the Hough space are proposed.

Resumé

La diffraction d'électrons rétrodiffusés (EBSD) est une technique de caractérisation reconnue en microscopie électronique en balayage. Au cours du dernier quart de siècle, plusieurs progrès ont amélioré cette technique et ont élargi le spectre de ces applications dans les domaines du génie des matériaux et des sciences géologiques. Ces améliorations ont principalement été reliées à la commercialisation des systèmes EBSD. Avec leur convivialité et leur simplicité d'utilisation, ces systèmes ont permis de rejoindre un plus grand public et ainsi de permettre la maturité de l'EBSD. Toutefois, ils ont également limité la communauté scientifique de participer au développement de cette technique. Les chercheurs qui font face à des problématiques inhabituelles n'ont pas la possibilité de modifier et de perfectionner les systèmes commerciaux pour répondre à leurs propres besoins. L'innovation est réservée aux scientifiques et aux ingénieurs travaillant pour les compagnies d'EBSD. Avec le développement d'un logiciel gratuit à code source libre pour le traitement des diagrammes de diffraction acquis par un système EBSD, EBSD-Image, ce travail propose une solution à ce problème.

Conçu à partir d'un logiciel d'analyse d'images, EBSD-Image offre une interface flexible et structurée pour l'implémentation de nouveaux algorithmes afin de traiter et d'extraire un maximum d'informations des diagrammes de diffraction. Deux exemples d'application sont présentés pour démontrer les avantages analytiques du logiciel. L'évaluation de la qualité de la diffraction a permis, pour l'un des deux exemples, de caractériser avec une plus grande exactitude la microstructure des tubes de forces d'alliage Zr-2.5Nb et, pour l'autre, de mesurer quantitativement le niveau de déformation induit lors de la préparation métallographique d'échantillons ainsi que de développer une nouvelle mesure de la qualité pour évaluer la déformation.

En outre, ce mémoire présente des outils pour la validation de nouveaux algorithmes par la génération de diagrammes de diffraction simulés et des fonctions utilitaires pour le traitement et l'analyse d'un large ensemble de données sur une grille de calcul. Deux formats de fichier sont introduits afin de fournir une méthode plus pratique pour la manipulation d'un grand nombre de fichiers et de permettre le partage des résultats d'une analyse. Finalement, une équation reliant les deux résolutions de la transformée de Hough pour des diagrammes de diffraction de n'importe quelle dimension et une méthode pour éliminer les artéfacts dans l'espace de Hough engendrés pour les bandes de Kikuchi verticales sont proposées.

Acknowledgments

I would like to express my gratitude to Dr. Pierre Hovington, Marin Lagacé and Professor Raynald Gauvin for their indispensable help throughout my thesis. It has been a great privilege to work with them. I learned a lot from their expertise and from the enriching discussions I had with them. Their vision, guidance and counsel were essential in the achievement of this project.

I am also grateful to the Natural Science and Engineering Research Council of Canada (NSERC), le Fonds québécois de la recherche sur la nature et les technologies (FQRNT) and Hydro-Québec for their financial support during my masters degree. I would also like to thank the Microbeam Analysis Society (MAS) and the Microscopical Society of Canada (MSC/SMC) for their travel awards.

This work would not have been possible without funding from the Research Institute of Hydro-Québec (Institut de recherche d'Hydro-Québec, IREQ) and especially Denis Thibault, the manager of this project. My acknowledgments extend to my coworkers at IREQ: Dr. Michel Trudeau for funding the work on Zr-2.5Nb pressure tubes, Chantal Baril, Alexandre Lapointe and Lisa Rodrigue for their knowledge on sample preparation, René Veillette for his assistance on the microscope, Benoît Morin for his expertise and support on operating the computer grid, and Stṕhane Godin, Hélène Gauthier, Adrien Guery and Laurent Tôn-Thât for their help with my work. I would like to acknowledge Prof. Philippe Bocher and Dr. Florent Bridier from École de technologie supérieure for their kindness in letting me use their microscope for several acquisitions.

I am particularly appreciative to Dr. George Vander Voort for his encouragement, advice and enlightening discussions on various aspects of my master and the field of materials engineering. I am also thankful to Scott Stizman for his assistance and support of my work.

I also want to thank my colleagues Derek Blais, Renaud Daenzer, Dr. Hendrix Demers and Camille Probst for the good times spent together and their advice before and during my masters. I thank Nalini Singh for reviewing my thesis.

Finally, I thank my family and friends for their unconditional support.

Abbreviations

API	Application programming interface
ASCII	American standard code for information interchange (encoding)
CANDU	Canada Deuterium Uranium
CCD	Charge coupled device
CIF	Crystallography information file (file format)
DD	Detector distance
DL	Deformed layer
EBSD	Electron backscatter diffraction
EbsdMMap	EBSD multiple map
EBSP	Electron backscatter pattern
EDS	Energy dispersive spectroscopy
FEG	Field emission gun
GUI	Graphical user interface
LOM	Light optical microscope
PC	Pattern center
px	Pixel
RAM	Random access memory
SBL	Shear band layer

SEM Scanning electron microscope

SMP Stream map (file format)

SNR Signal to noise ratio

TEM Transmission electron microscope

XML Extensible markup language (file format)

XRD X-ray diffraction

List of Tables

List of Figures

Chapter 1

Introduction

Electron backscatter diffraction has become an established characterization technique in the scanning electron microscope, and is widely used in the fields of materials and geological science. Its main advantage over other characterization techniques is that it allows the crystallographic information of a sample to be correlated with its microstructure. Common applications of EBSD are: grain analysis, grain boundary engineering, local strain measurement, and second phase distribution.

While the transmission electron microscope can also extract the same data, it has some drawbacks [1]. Firstly, the equipment and expertise needed to get an artifact and defect free sample make sample preparation for TEM quite challenging. Second, its small sampling size makes statistical analysis of the data, such as texture analysis, impractical. The main advantage of the TEM is its high resolution. Another technique for texture measurements is X-ray diffraction. Contrary to TEM, it has a large sampling volume, but a much lower resolution. As such, XRD measurements cannot be directly correlated to the microstructure as only the volume fraction and the texture of the different phases in a sample are measured. EBSD provides the middle-ground between these two techniques. What EBSD lacks in resolution with respect to TEM is compensated with an important increase in statistics, while the higher resolution of EBSD outweighs the larger sampling volume of XRD for many applications. The difference in the sampling and resolution of the three techniques makes them complementary to each other.

The EBSD technique consists of analysing patterns created by the diffraction of backscattered electrons, as the electron beam of the SEM is rastered over a sample. The patterns are recorded by a camera and analyzed by software. A major advancement in the early 1990s was the development of software to automatically extract the phase and orientation from these diffraction patterns [2–4]. This process is referred to as au-

tomated indexing. The first EBSD systems were commercialized by the HKL company (now Oxford Instruments), followed by TexSEM Laboratories (now Ametek EDAX). Over the years, improvements in microelectronics and the development of new cameras with greater sensitivity and increased speed has contributed to the expansion of the technique [5]. As proof of the growing market of EBSD, new microanalysis companies (Bruker and Thermo Scientific) are now offering EBSD systems.

These systems are designed to reach a broad audience of users and cover a large range of applications. For conviviality and simplicity, several parameters and acquisition steps are often hidden from the user. As a consequence, they are forced to treat the software as a "black box". For specific applications, such default parameters are inadequate and should be optimized to achieve better accuracy. Furthermore, with the advance in camera technology, commercial software are moving towards the use of faster acquisition rates [6, 7]. Hence, more complex image processing algorithms which increase the overall accuracy are often discarded because they would also increase the overall acquisition time.

These limitations were pointed out by Tao in the closing statements of his Ph.D. thesis on the mapping of small orientation differences in lattices using EBSD [8]. As a solution, he proposed the idea of a "dummy" EBSD software, complementary to commercial software, that would allow off-line processing (after acquisition on the microscope) of diffraction patterns with direct user inputs. He highlighted the following advantages of such system: saving SEM time, adjustment of parameters to improve indexing and better discrimination of bad points. These potential improvements are in line with those recently presented by Schwarzer [7] who designed an in-house (not distributed) EBSD system [9].

The motivation for this work is built on the philosophy described by these two authors. A software, entitled EBSD-Image, was developed to serve as a research and development tool for the EBSD community. Its main objective is to give a high level of flexibility to the user. The scope of this software encompasses Tao's concept of "dummy" EBSD software. EBSD-Image consists of a simulation and an analysis engine. The former simulates diffraction patterns using the kinematic diffraction model. As will be shown, in Chapter 3, simulated diffraction patterns are a useful tool in understanding the algorithms implemented in EBSD software. The analysis engine (Chapter 4) is responsible for processing diffraction patterns in order to extract information such as the orientation, phase and quality metrics. EBSD-Image is a cross-platform, open source and freely available software. It is distributed under the Free Software Foundation General Public License

version 3 (GPL v3). To our knowledge, it is the first open source software dedicated to the processing of diffraction patterns. By making the software open source, we hope to create a community around it that will contribute to its growth. For documentation, source code and installation packages, we invite the reader to consult EBSD-Image's website: `www.ebsd-image.org`.

The literature review (Chapter 2) offers an overview of the EBSD technique from the theory behind the formation of diffraction patterns to the applications of this technique to problems in materials science. A large portion of this chapter is dedicated to explaining the processing steps involved in the analysis of diffraction patterns by EBSD software. Understanding the modes of operation of an EBSD system is imperative to the development of the simulation and analysis engines of EBSD-Image. Chapter 3 describes the crystallographic and geometrical considerations related to the simulation of diffraction patterns. The evaluation of diffraction pattern quality is given as one application of the engine as a research tool. The following chapter discusses the reasoning and concepts behind the analysis engine. The structure of the engine is defined to illustrate its flexibility and expandability. Details about the implementation and modifications made to the algorithms used in the analysis engine are given. Finally, two applications of the aforementioned engines are given in the last chapter. These examples are chosen to highlight new analytical possibilities that can be gained EBSD-Image.

Chapter 2

Literature Review

This literature review focuses on four aspects of the electron backscatter diffraction technique: (i) the formation of diffraction patterns (ii) the software required to perform EBSD analysis (iii) the evaluation of the diffraction quality and, (iv) an overview of other third-party software currently available.

First, we will summarize the physical models explaining the diffraction of backscatter electrons inside a bulk sample as well as the formation of diffraction patterns. In the past 25 years, one of the major advancements of this technique was the development of computer software to replace manual interpretation of patterns. The requirements of performing such tasks will be described; only the general concepts common to most modern EBSD systems will be discussed, leaving the explanation of more detailed implementations for later chapters. An important parameter for any analytical technique is its resolution. To complete the description of the technique, Appendix A reviews the models and experimental measurements performed to evaluate the resolution of EBSD and its limiting factors.

A promising field of research for the future development of EBSD is the extraction of additional information from diffraction patterns to better analyze the microstructure, deformation level of materials, *etc*. One method of obtaining this information is the calculation of quality metrics to evaluate how well a sample is diffracting. We will give the definition of common quality metrics and summarize some of their applications published in the literature. Finally, an overview of current third-party software (programs not distributed by EBSD manufacturers) will be given to situate this work with respect to other developments in the EBSD community.

2.1 Formation of Diffraction Patterns

The origin of diffraction patterns in a SEM is closely related to the Kikuchi patterns observed in TEM. Both are the product of diffuse scattering of electrons from the incident beam and diffraction of these electrons by crystallographic planes of the sample. Diffuse scattering refers to the incoherent scattering of the high energy electrons of the incident beam in all directions within the specimen [10].

One difference between TEM and SEM Kikuchi patterns is that the diffuse scattering mainly occurs in the forward direction in TEM whereas the scattering causes backscattering in SEM. The Kikuchi pattern is therefore visualized below the specimen in TEM observation conditions. For SEM, it is the backscatter electrons (electrons exiting the specimen from the same surface incident electrons enter) that are responsible for the formation of the Kikuchi patterns.

However, in either technique, an important characteristic of diffuse scattering is that scattered electrons span all the possible angles with respect to a crystallographic plane [10]. Only those that respect Bragg's Law will diffract. The Bragg's Law is defined by Equation 2.1 where d is the plane spacing, θ the critical diffraction angle or Bragg angle, n the order of the reflection and λ the wavelength of the incident beam.

$$2d \sin \theta = n\lambda \tag{2.1}$$

The equation implies that only the electrons traveling at an angle θ relative to the plane will undergo diffraction. The result is the formation of diffraction cones (referred to as Kossel cones) as shown in Figure 2.1. There is one cone on each side of the crystallography plane. The cones are separated by an angle of 2θ (*i.e.* an opening of $180° - 2\theta$).

It is the intersection of the Kossel cones with the camera/screen that creates a pair of Kikuchi lines which are referred to as a Kikuchi band. The trace of the crystallographic plane is therefore half way between the lines. The curvature of the cones is barely noticeable in TEM or SEM due to the small wavelength λ of the electrons which leads to very small Bragg angles [5, 10]. The wavelength is inversely proportional to the beam energy [10].

To understand the intensity of the Kikuchi lines and that of the Kikuchi bands, the Bloch waves model is used [11, 12]. The effect of electron waves on a periodic lattice can be solved using the superposition of Bloch waves travelling within the lattice. Near the Bragg condition, two Bloch waves dominate: (i) a wave having its maximum values in

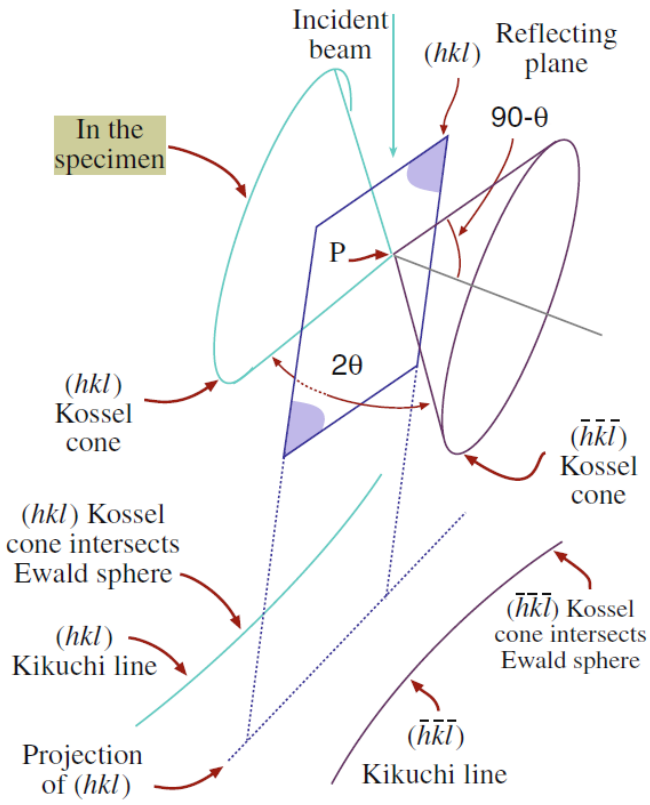

Figure 2.1: Schematic representation of the election diffraction inside a specimen and the formation of Kossel cones [10].

line with the rows of atoms (ii) a wave having its maximum values in line with the spacing between the rows of atoms (the minimum values are in line with the rows of atoms). The two types of waves are depicted in Figure 2.2. The intensity of the first wave is strongly attenuated by the atoms and results in a strong backscatter signal. On the other hand, the second wave travels deeper inside the lattice and produces less scattering — this is referred as electron channelling. The relative intensity between the two waves varies with the incident angle [11].

The formation of Kikuchi bands can be summarized by considering three cases. First, if the incident angle of the wave is exactly equal to the Bragg angle, the two waves have the same intensity. At larger angles, the second type of Bloch wave is preferentially excited and the scattering intensity decreases as the wave travels deeper inside the lattice. Finally, for incident angles smaller than the Bragg angle, the first type of wave dominates, leading to an increase of the electron scattering. The variation in the degree of scattering is responsible for creating the intensity profile of a Kikuchi band (Figure 2.3) [11]. This phenomenon cannot be explained using Bragg's Law and requires the use of Bloch waves.

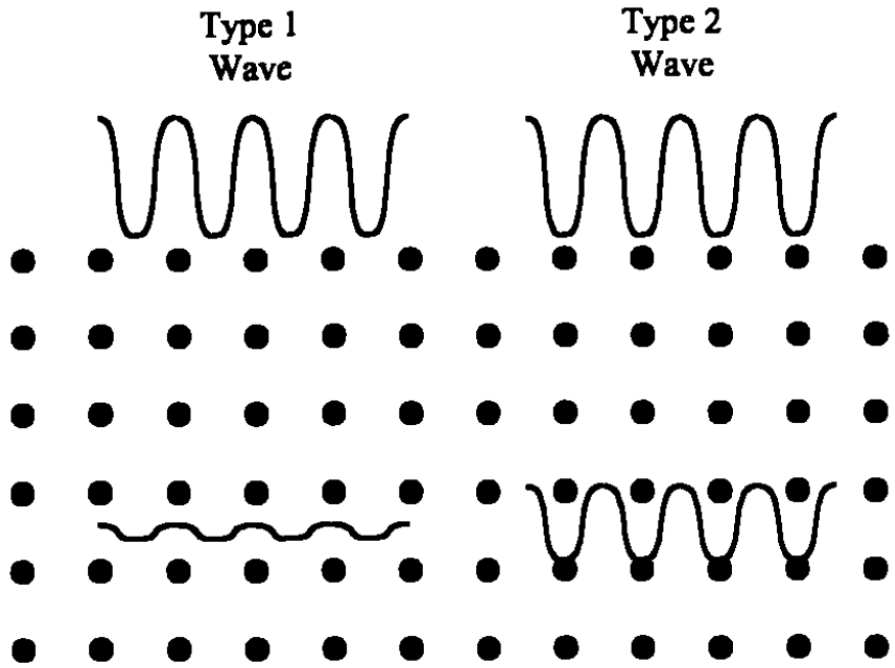

Figure 2.2: Schematic representation of the propagation of the Bloch waves of type 1 and 2 inside a lattice [11].

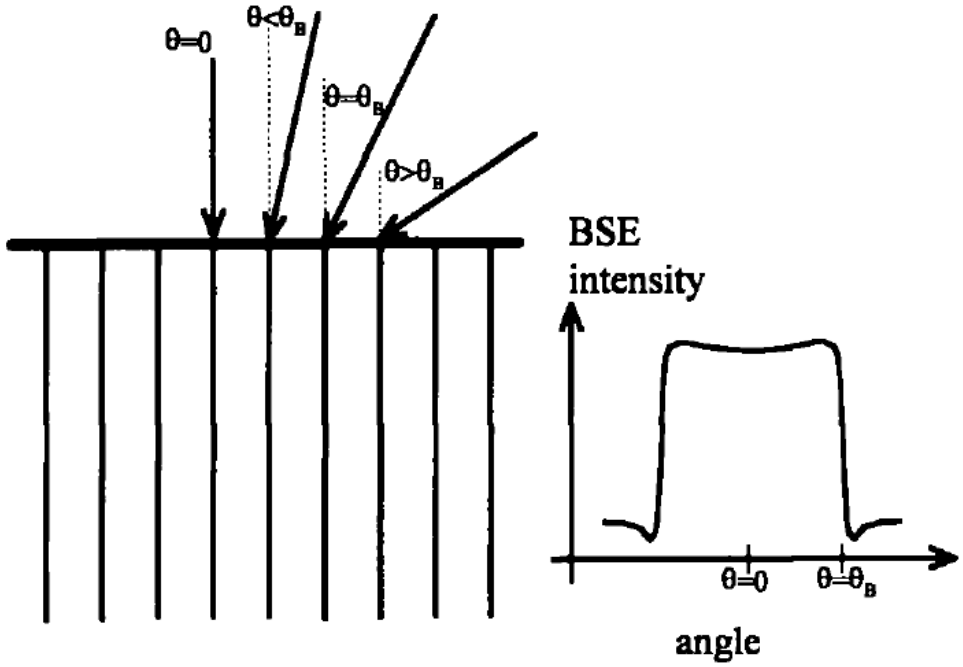

Figure 2.3: Variation of the intensity profile of a Kikuchi band for different incident angles θ [11]. The Bragg angle is identified as θ_B.

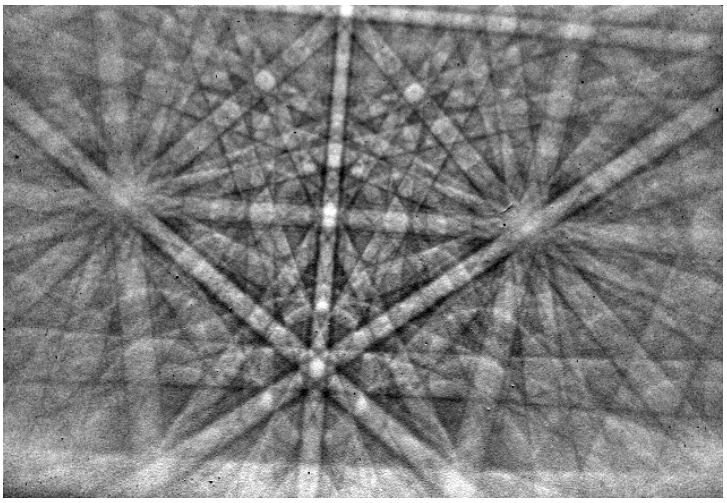

Figure 2.4: Example of a diffraction pattern of a germanium single crystal acquired at 20 keV

In summary, Bragg's Law defines the geometry and position of the Kikuchi bands inside a diffraction pattern, whereas the intensities within that pattern are derived from a channelling model based on Bloch waves. A high quality diffraction pattern acquired in a SEM of a germanium single crystal is shown in Figure 2.4. The variation of intensity inside the Kikuchi bands can be observed. As will be discussed in upcoming sections, the EBSD technique is entirely based on the analysis of these diffraction patterns.

2.2 Automated Measurement

The analysis of a sample using an EBSD system necessitates several processing steps and a close integration with the scanning electron microscope. Fortunately, commercial EBSD systems are automated and designed to facilitate the acquisition. After the set-up of the parameters by the user, the software takes care of moving the electron beam, recording the diffraction patterns, identifying the phases, calculating the orientations and compiling all the results. The hardware requirements of an EBSD system and the important parameters influencing the acquisition of diffraction patterns are given in Appendix B to focus, in this section, on the specifications of an EBSD software.

The EBSD software is responsible for controlling the hardware to acquire a series of diffraction patterns and for processing them to extract the phase(s) and orientation(s) of one or many regions on a sample. This process consists of three principal steps: (i) the acquisition of diffraction patterns (ii) the bands detection (iii) the indexing. Acquisition

refers to the automation of the microscope, the camera and the digitalization of diffraction patterns collected by the camera. The bands detection is the localization of the Kikuchi bands in the diffraction pattern — this information is required to perform the indexing. The latter is defined as the association of a phase and an orientation to a diffraction pattern by finding the best matching solution to its Kikuchi bands.

Improvements in the speed of the camera and the development of new acquisition conditions are constantly changing the technique and its limits. The explanations in the following paragraphs are therefore related to a typical, currently available EBSD system. For more in-depth explanations, we refer the reader to the book entitled "Electron Backscattered Diffraction in Material Science" (Schwartz et al., 2009)[13]. The latter, as well as the review paper of Robert Schwarzer [9], also covers the historical background of the technique which will not be discussed in this work.

2.2.1 Acquisition

An important part of the automation of an EBSD system is the acquisition of electron backscatter patterns (EBSP). EBSD is a mapping process; information is collected at different points on an imaginary grid placed on top of the sample. The size of the grid as well as the horizontal and vertical spacing between the points will determine the number of points collected, the resolution and the time of the acquisition. A diffraction pattern is acquired at each point of this grid by either mechanically moving the stage or by electronically moving the electron beam with the microscope's scan coils. The former is used for low magnification mapping to cover a large area of the sample. The latter is the most commonly used method since it provides better accuracy on the positioning of the beam. The diffraction patterns are first stored in the computer's memory, but can later be stored on the hard drive. The storage method will be further investigate in section 4.3.

To cover large areas on a sample, several mappings can be acquired one after the other and juxtaposed at the end by a stitching algorithm. The software mechanically moves the stage from one mapping area to another. The accuracy advantage of the beam scanning mode of operation is combined with the large coverage of a mechanical scanning acquisition [5].

2.2.2 Bands Detection

The band detection and indexing steps are typically performed right after the acquisition of each diffraction pattern. However, as suggested by Schwarzer [7] and this work, it can be advantageous to execute these calculation intensive steps after all the diffraction patterns have been acquired. The advantages are all linked with the decrease in the total acquisition time of a given mapping. A faster acquisition leads to reduced operating costs (less time spent on the microscope); samples that are less prone to drift problems, ideal of in-situ experiments, *etc*. Another advantage, which will be highlighted in this work, is the use of better algorithms which may not be optimized for high speed acquisition. This shifts the current focus of commercial software to have the fastest acquisition speed towards the use of better algorithms to instead give more precise, quality mappings. However, an obvious disadvantage of off-line processing is the inability to evaluate *a priori* the quality of a mapping (*i.e.* the hit rate).

Regardless of whether band detection is performed on or off-line, the goal of this step is unchanged: identifying the Kikuchi bands of a diffraction pattern. It is this information that the indexing step requires to associate a phase and an orientation to a diffraction pattern. More precisely, the angle between the different bands are used since they are "unique for a particular crystal structure and crystal lattice orientation" [5]. Although it might appear trivial for the trained human eye to locate Kikuchi bands, it is far from being a straightforward task for a computer algorithm. The noise in the pattern, diffuseness of the band edges, non-uniform intensity distribution inside the bands and variation in the band width all increase the challenge. Typical edge detection algorithms such as the Canny filter[14] are incapable of reliably detecting the Kikuchi bands.

The most common method used by all commercial software is to change the parametrization of the diffraction pattern. The Cartesian image space of the diffraction pattern is transformed such that the Kikuchi bands are represented as peaks (*i.e.* areas of high intensity). Peaks are easier to identify than bands from the point of view of a computer algorithm. This idea was first proposed by Krieger Lassen [3]. The transformation used for band detection in EBSD is either the Hough transform [15, 16] or the Radon transform [17, 18]. The Hough transform is a special case of the Radon transform [18]. Although the transformations are not calculated in the same way, their result is the same. In the following paragraphs, we will discuss the Hough transform in greater detail. The same explanations would apply to the Radon transform [9].

A typical parametrization of a line is by its slope and intercept ($y = mx+b$). However, this definition does not apply for vertical lines as their slope tends towards infinity. Duda

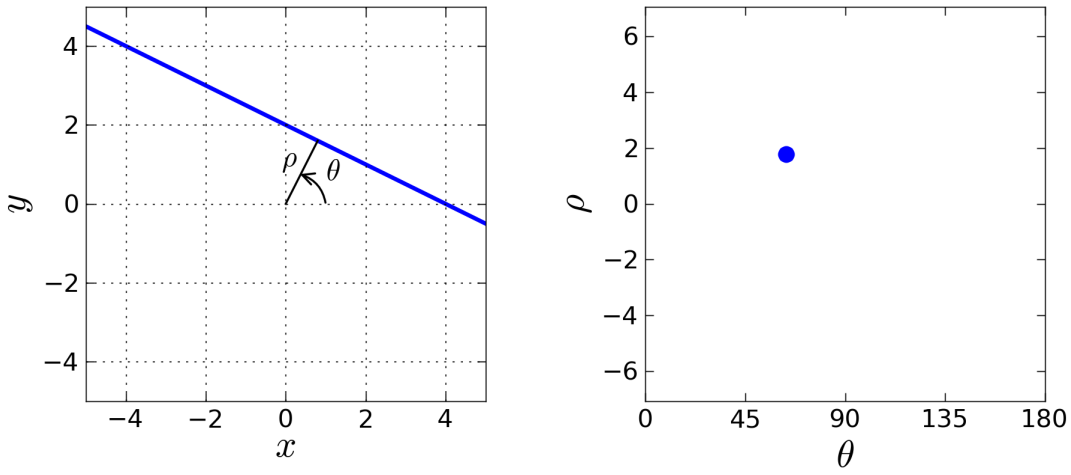

Figure 2.5: Schematic representation of Duda & Hart's parametrization of a line.

& Hart [16] proposed a new parametrization which describes a line with its shortest distance ρ from the origin and its angle θ with respect to the horizontal axis. Figure 2.5 illustrates the definition of θ and ρ for a given line. Note that the origin is taken to be at the center of the image.

Different boundary conditions can be chosen for θ and ρ. If θ varies between 0 and 2π, ρ is bounded between 0 and R, where R is half the diagonal of the image. On the other hand, if θ varies between 0 and π, ρ must take negative values to represent line located below the x-axis. The boundaries for ρ are therefore inclusively between $-R$ and R. Both sets of boundary conditions are equivalent. However, the latter is more common since it requires less computation. As it will be shown later in this section, the time needed to compute the Hough transform is proportional to the θ increment.

With this parametrization, the image space is transformed to the Hough space. The image space is the one of the diffraction pattern where the origin is taken at the center of the image. It is a discrete space made up of a certain amount of pixels in the x and y directions. The intensity of those pixels can be seen as the third dimension. Similarly, the Hough space has three dimensions. The x and y axes of the image space are replaced by the θ and ρ axes while the third dimension now represents the intensity of the Hough space. By definition, the Hough space is continuous since within their boundaries θ and ρ can take any value. The Hough space is quantized to allow for computerized treatment. As for the image space, the discrete Hough space has a certain amount of pixels in the θ and ρ direction. A more in-depth discussion on the quantization of the Hough space is

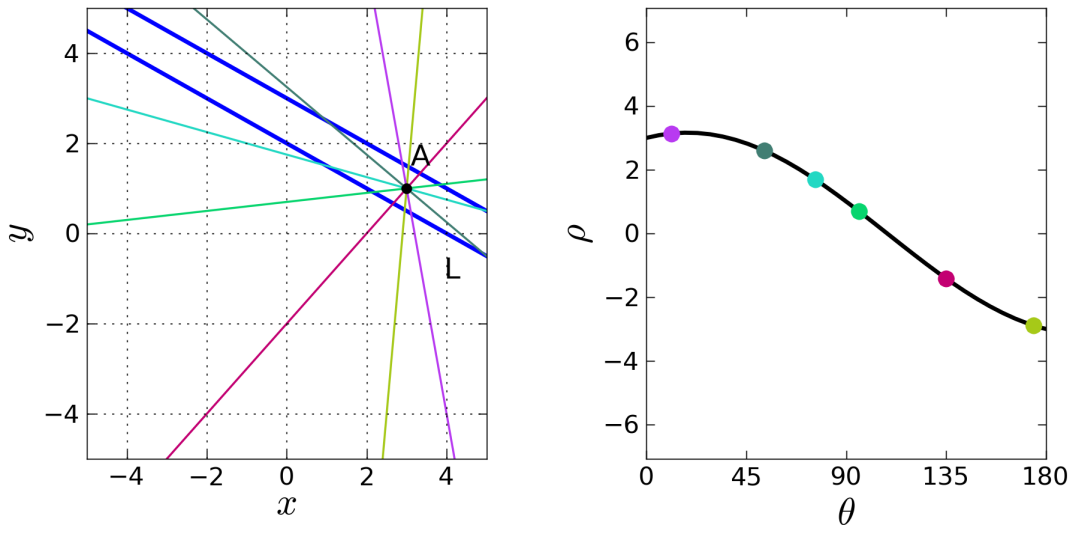

Figure 2.6: Schematic representation of the image space (left) with a band $\mathcal{L}$ and a pixel $\mathcal{A}$ and the Hough space (right) with the corresponding sinusoidal curve.

given in section 4.5.1.

The transformation is performed by calculating ρ using Equation 2.2 for each pixel (x_i, y_i) in the image space and for each θ_j in the Hough space, where the subscript i refers to the index of the pixels in the image space and j to the index of the pixels in the Hough space.

$$\rho = x_i \cos\theta_j + y_i \sin\theta_j \tag{2.2}$$

Effectively, this transformation converts each pixel of the image space into a sinusoidal curve in the Hough space. The calculated ρ value is rounded to the closest pixel ρ_j. The intensity of the pixels (θ_j, ρ_j) that are part of the sinusoidal curve are augmented by the intensity of the corresponding pixel (x_i, y_i) in the image space. The accumulation of these intensities give rise to peaks in the Hough space which corresponds to the θ and ρ coordinates of the bands in the image space.

The understanding of these results is not straightforward. An obvious question is why sinusoidal curves of individual, uncorrelated pixels in a band intersect in the Hough space at a specific and unique position? To answer this question, we shall refer to Figure 2.6 where the image and Hough space are respectively shown on the left and right of the figure.

From the definition of the Hough transform, each pixel in the image space is trans-

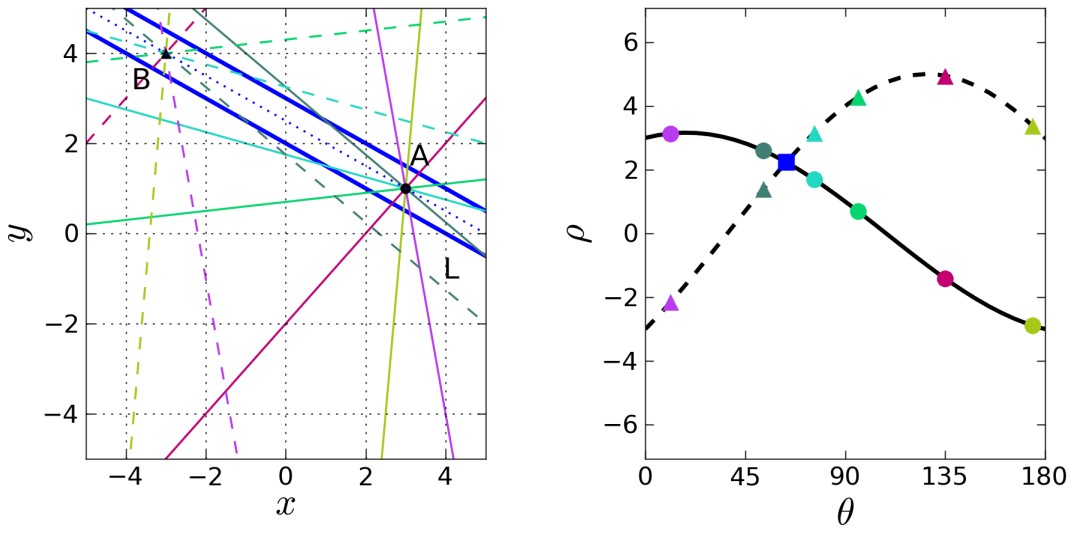

Figure 2.7: Schematic representation of the image space (left) with a band $\mathcal{L}$ and pixels $\mathcal{A}$ and $\mathcal{B}$, and the Hough space (right) with the two corresponding sinusoidal curves

formed into a sinusoidal curve in the Hough space. The curve represents all the possible unidimensional lines that can be passing through that pixel in the image space. A few lines are drawn in Figure 2.6 with their corresponding position in Hough space represented by circle markers. Only a small fraction of the lines are fully contained in the band, the rest of the lines cross it, but most of their pixels are outside the band. If this geometrical construction is repeated for another pixel, $\mathcal{B}$, of the band $\mathcal{L}$, the same result is obtained. Figure 2.7 extends Figure 2.6 by showing the lines passing by $\mathcal{B}$ and their equivalent representation in Hough space using triangular marker. All the lines or curves related to pixel $\mathcal{B}$ are drawn as dashed lines.

The lines inside of band $\mathcal{L}$ and passing by pixel $\mathcal{B}$ are the same lines that are also passing by pixel $\mathcal{A}$. In Hough space, these lines end up having the same coordinates θ and ρ, forming a peak. The intersection of the sinusoidal curves therefore corresponds to the lines that are fully inscribed inside the band in the image space. The intensity at this intersection is higher than the background because of two interlinked reasons: (i) the sinusoidal curve of the pixels in the band have a higher intensity that the one of the pixels outside of it (ii) the intensity of many sinusoidal curves is added at this intersection.

If the band would have a width of 1 px, the area covered by its corresponding peak in Hough space would be approximately equal to $1\,\text{px}^2$ [3]. However, the bands in a

diffraction pattern are wider than 1 px. This results in the formation of a peak covering a large area. The center of a peak corresponds to the center of its corresponding band. From our previous explanation, the height and width of the peak will depend on the lines that pass through the pixels of the band and that are fully inscribed inside it. We shall leave the derivation of the peak dimensions and the consequences of this phenomenon on the bands detection for a later discussion in section 4.5.1.

Moving away from the conceptual Hough transform, the Hough space representation of an experimental diffraction pattern of a silicon single crystal (Figure 2.8) is shown in Figure 2.9. The location of the most intense Kikuchi bands can be clearly identified in Hough space by the bright peaks while other peaks are more faint and barely noticeable. It is the task of the peak detection algorithm to segment out the high intensity peaks from the background and disregard possible false peaks (see Section 4.5.2 for the description of two detection algorithms). The segmentation of Figure 2.9 is shown in Figure 2.10. To evaluate the result, the corresponding line of each peak in Figure 2.10 is overlaid on the original diffraction pattern in Figure 2.11. The lines and the peaks are colour-coded to illustrate their relationship.

2.2.3 Indexing

The first step of any indexing algorithm is to calculate for each phase selected by the user, the list of all the possible angles between the crystallographic planes (often referred to as the look-up table) [2–4]. In the following explanations, we will assume for simplicity that the analyzed material has only one phase. As demonstrated by Boisen and Gibbs [19], the interplanar angle θ between planes (h_1, k_1, l_1) and (h_2, k_2, l_2) for any crystal system is given by their dot product:

$$\cos\theta = \frac{\mathcal{C}\,(h_1, k_1, l_1) \cdot \mathcal{C}\,(h_2, k_2, l_2)}{\|(h_1, k_1, l_1)\|\,\|(h_2, k_2, l_2)\|} \tag{2.3}$$

where C is the Cartesian matrix. Only the angles between the most intense planes are calculated since they will be the ones detected as Kikuchi bands in the diffraction pattern. The threshold on the number of planes to use is usually a parameter that is left to user discretion.

The second step is to calculate the angles between the Kikuchi bands in the diffraction pattern (*i.e.* the experimental angles). More precisely, this operation is to find the angles between the normals of the crystallographic planes that form the Kikuchi bands. The calibration of the camera is used to convert the equation of the line passing by the center

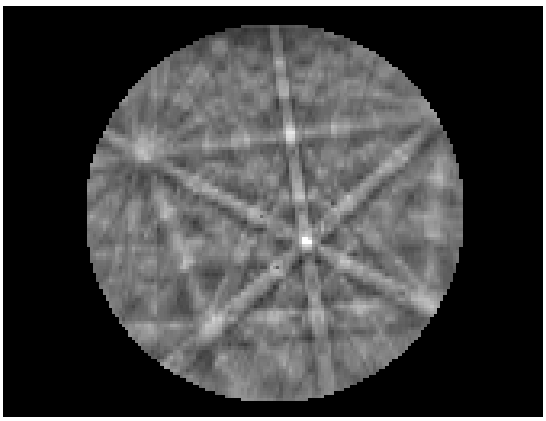

Figure 2.8: Diffraction pattern of a silicon single crystal.

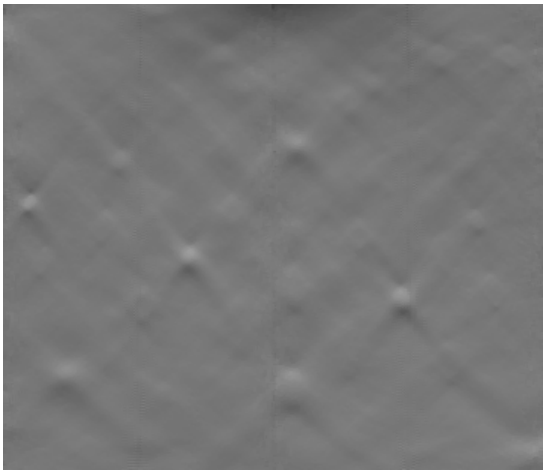

Figure 2.9: Corresponding Hough space of the diffraction pattern.

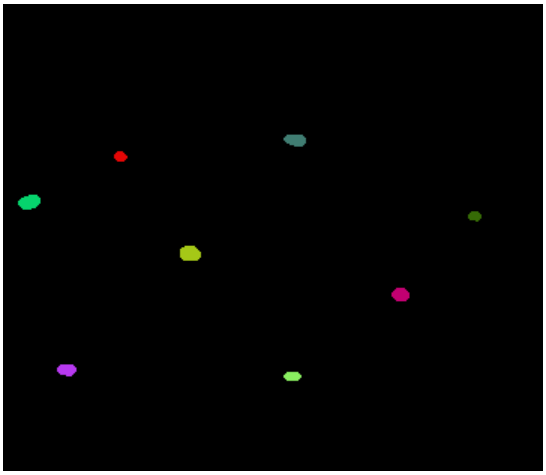

Figure 2.10: Segmentation of the peaks in Hough space.

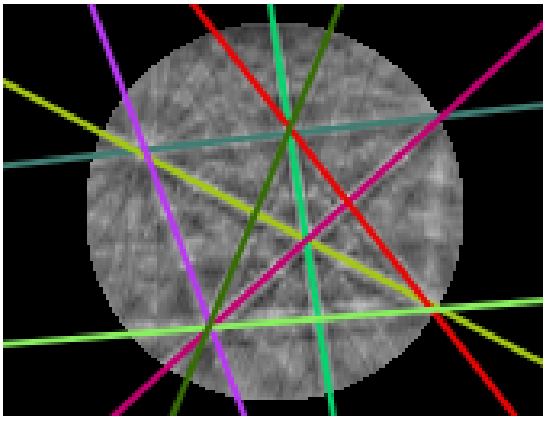

Figure 2.11: Overlay of the corresponding lines of the segmented peaks on the diffraction pattern.

of a Kikuchi band to a 3D vector representing the normal of a crystallographic plane. The angle between two normals is also calculated with the dot product.

The next step of indexing is the comparison of experimental and theoretical angles to find one or many solutions. The implementation of the comparison depends on the indexing algorithm. From the authors' knowledge, there are two main algorithms that are currently being used. We shall give a brief overview of the two methods. For a more detailed description, we refer the readers to the Ph.D. theses of Wright [4] and Krieger Lassen [3]. It is however highly probable that the implementation of these algorithms in the current commercial EBSD software has changed over time.

The first method was proposed by Schmidt [2] and was further improved upon by Krieger Lassen [3]. From the normals of the two most intense Kikuchi bands, a set of possible crystallographic planes is found by finding the closest matching angle in the look-up table. From this set of potential solutions, rotation matrices between the crystal and the camera frame are calculated. To eliminate solutions, the theoretical normals of the Kikuchi bands in the diffraction pattern is calculated for each rotation matrix. The theoretical and experimental normals are then compared and the solution with the smallest mismatch is selected. A measure of the fit is returned to evaluate the error on the indexing.

The major difference between this method and the one of Wright [4] is that the latter finds a set of solutions using three bands instead of two. From the experimental normals, all the possible triplets (groupings of three) are determined. For each of these experimental triplets, a set of potential solutions is found from the look-up table. The method uses a voting scheme which gives a vote to each solution. After this operation is performed on all the triplets, the best solution is the one with the most votes. A confidence index on the identified solution is calculated by a comparison between the first and second solution with the most votes. If the first solution has a lot more votes than the second one, the solution is highly accurate. On the other hand, if the two solutions have a similar amount of votes, the solution is ambiguous. Allegedly, this voting scheme and the use of triplets allows for better deconvolution of overlapping diffraction patterns [20]. However, this method has more difficulty discriminating between solutions from low symmetry crystal structures than the one of Schmidt and Krieger Lassen - this is the case for geological specimens [21].

2.3 Quality Metrics

The primary use of diffraction patterns is to perform phase identification and orientation measurements. For these applications, the angles between the Kikuchi bands and, on some occasions, the width of the bands are used, as explained previously. However, more information can be extracted from diffraction patterns by looking at the variation of their quality. A general definition of the term "quality" from an EBSD point of view would be an appreciation of how well a crystal is diffracting. Different features of a diffraction pattern can be evaluated to assess its quality: intensity, contrast, sharpness of Kikuchi bands, noise level, *etc*. As such, different quality metrics can be designed to highlight these features for each diffraction pattern in a mapping. The metrics evaluate the quality of a diffraction pattern by calculating a numerical value representing the amount, strength or intensity of one or many specific features. An interesting parallel can be made between different quality metrics obtained from diffraction patterns and the different electron signals found in modern SEMs, namely secondary (upper or lower detector) and backscattered electrons detector (low and high angle). Electron signals give different ways of evaluating the interaction of the electron beams with the sample, whereas quality metrics offer a similar evaluation of the diffraction of the primary electrons with the crystallographic structure.

Quality metrics are complementary information to the crystallographic orientation obtained by pattern indexing. Other applications of quality metrics will be detailed in this section. They include examples for: (i) evaluating the strain level (ii) discriminating crystallographically similar phases (iii) estimating the accuracy of the measurements. Then we shall give the formal definition and current understanding of several quality metrics that will be used later in this work.

2.3.1 Area of Use

When a crystal is deformed, the dimensions of its lattice are distorted. This non-uniformity in the lattice leads to a greater distribution of the angles at which a crystallographic plane diffracts. Effectively, the Kossel cones emanating from the sample have a greater variation. On the diffraction pattern, this is manifested by blurring the Kikuchi bands edges [22, 23]. Furthermore, from the Bloch waves theory, this distortion inhibits the propagation of the Bloch waves resulting in a decrease in contrast of the Kikuchi bands [22, 23]. Wilkinson and Dingley [22] observed this phenomenon by comparing the intensity profile of the Kikuchi band of specific planes from undeformed and strained

specimens. Although they found that specimen contamination in the SEM was a significant source of error, the Kikuchi band contrast and sharpness were found to decrease as the amount of deformation increased. A similar study was performed by Keller et al. [23] using the image quality value calculated by the TSL software. The image quality is a measure of the Kikuchi bands' intensities which is linked with the sharpness of the bands. Their measurements of the strain fields around an AlGaAs layer inside a GaAs matrix correlates with their finite element predictions. These two examples show that quality metrics based on the Kikuchi band profile or total intensity can evaluate the amount of deformation.

The analysis of the microstructure of commercial steels is a common application for EBSD. Although diffraction patterns of ferrite grains (body centered cubic crystal structure) can easily be differentiated from retained austenite grains (face centered cubic), EBSD is incapable of separating martensite or bainite regions from the ferrite grains. Martensite or bainite are obtained by rapid cooling from the austenite phase leaving the carbon atoms (soluble in the austenite phase) trapped inside a body centered cubic crystal structure. This result is the formation of a metastable body centered tetragonal structure. The c/a ratio of the tetragonal lattice is very close to unity [24] and is therefore very close to a cubic lattice. This slight variation of the c/a ratio is undetectable in normal EBSD operating conditions. The crystal structure of martensite, bainite and ferrite are indistinguishable from one another.

However, the dislocation density of bainite or martensite is higher than that of ferrite [25]. The higher dislocation density deteriorates the quality of the diffraction pattern due to the higher lattice distortion. On average, diffraction patterns of ferrite therefore have a higher quality than those of bainite and martensite. This principle was verified via nano and microhardness measurements by Wu et al. [26]. The separation of bainite from martensite is more complex since the difference in their dislocation densities is smaller. Ryde concludes that the discrimination between these two phases could only be performed by "analyzing the directions of the carbide precipitates with a high resolution microscope" [24].

Szabó and Szalai [27], Wu et al. [26], Ryde [24], and Petrov et al. [25] used a quality metric related to the average intensity of the Kikuchi bands to successfully segment the ferrite from the martensite in duplex or TRIP-assisted steels. They used different methods to achieve the segmentation, but each of them consist of assigning the pixels with a quality lower than a threshold value to martensite and the others to ferrite. The quality metric was either the image quality as calculated by the TSL OIM software, the

band contrast as calculated by the Oxford HKL Channel 5 software or the band slope also calculated from Oxford's software. The band contrast is said to be closely related to the image quality. The band slope is related to the "slope of the intensity change between the background of the pattern and the band"[24].

As mentioned by Wu et al. [26], the effect of grain boundaries on phase segmentation must be taken into account. As with martensite or bainite, diffraction patterns near or at grain boundaries also have a lower quality. Wu et al. proposed a normalizing method combined with a multi-peak model for evaluating the area fraction of the different phases. The accuracy of the technique is, however, influenced by the presence of residual strain which would lower the quality of certain regions. Petrov et al. did a similar study to Wu et al. on a TRIP-assisted steel. They compared their EBSD results with optical micrographs and magnetic measurements. The area fractions of the retained austenite, bainite and ferrite calculated for these techniques were in good agreement with each other. They attributed the discrepancies to the variability in the size of the observed areas (largest for the magnetic measurements and smallest for EBSD). Finally, Ryde used the average image quality inside each grain to separate the martensite from the ferrite grains. This method was in good agreement with the microstructure observation. For the same sample, he also found that the band slope gave a better discrimination than the image quality.

The use of quality metrics for phase discrimination in steels was also studied by Wright and Nowell [28] as well as the effect of quality metrics on grain boundaries determination and strain measurements. Aside from image quality, they looked at the variation of the average, standard deviation and entropy of the diffraction patterns as originally proposed by Tao [8]. Their observations on an Al−Cu, extruded copper and steel samples showed that the image quality is the best quality metric to differentiate grain boundaries and strain while the pattern intensity average provides better phase contrast. The authors also noted an important point about quality metrics: their dependence on the crystallographic orientation. Two grains of the same phase and with the same strain level can have two different values of a quality metric. This difference is due to the variation of the Kikuchi bands' intensity from one set of crystallographic planes to another. However, this difference is "generally much smaller than the one due to phase, grain boundaries or strain"[28].

2.3.2 Formulation

Several quality metrics will be used in this work for phase identification and strain measurements. Some of them are proprietary to an EBSD software package and their definition is unknown or ambiguous. The following paragraphs attempt to give an overview of all currently available quality metrics that are part of an EBSD software or that were published in the literature. Quality metrics can be split into two categories based on which information they are extracted from.

The first kind are directly derived from the diffraction pattern. In other words, they are calculated from the pixels of a diffraction pattern. The average, the standard deviation and the entropy as used by Wright, Nowell and Tao [8, 28] are good examples. The average measures the mean intensity of the diffraction pattern which is related to the overall backscatter yield. It is also sensitive to surface topography, contamination, camera gain and current drift [28]. The standard deviation of any image is the measure of the contrast and noise. In the case of a diffraction pattern, this quality metric is related to the contrast between the Kikuchi band and the background. The Shannon entropy [29] is based on information theory. It is an estimation of the compressibility of an image. A uniform image would have an entropy of zero whereas an image with many intensity variations would have a high entropy. Its relation with a diffraction pattern is not well understood. Another quality metric directly related to the diffraction pattern was proposed by Krieger Lassen in his Ph.D. thesis [3]. It consists of evaluating the level of low frequencies in a diffraction pattern by using the Fourier transform. It is therefore related to the amount of noise in an image. High quality diffraction patterns have a stronger low frequency components than low quality patterns. He applied this concept to evaluate recrystallized and non-recrystallized regions on an aluminum sample. Finally, the signal to noise ratio is the comparison between the amount of significant information and noise in an image [30]. It is a technique used to evaluate the quality of electron micrographs, [31] which can also be applied to diffraction patterns. It is calculated using the cross-correlation between odd and even rows of a given image [30].

Other quality metrics are derived from the Hough space, more precisely from the intensity of the peaks. The intensities in the Hough space correspond to the intensity along a line in the diffraction pattern. In that sense, the intensity of the peaks corresponds to the intensity of the Kikuchi bands. Since these quality metrics rely on the computation of the Hough transform and peak detection, they are influenced by the resolution and post-treatment performed on the Hough space. They are however independent of the indexing algorithm. The image quality is defined as the average intensity of all the

detected peaks [28, 32]. Allegedly this definition is used in the TSL OIM software. Similarly, the pattern quality, used in the Oxford INCA Crystal software, is defined as the mean intensity of the three most intense peaks divided by the standard deviation of the Hough transform [33]. The calculations behind the band contrast or the band slope are not published in the literature. From a personal communication with one of the founding engineers of the HKL software, the band contrast would be the difference between the intensity of the most and the seventh most intense peaks [34].

Table 2.1 summarizes the equation to calculate the aforementioned quality metrics.

2.4 EBSD Software

Apart from commercial software, there are several third-party software that can be found for post-processing of EBSD mappings using the different output files of commercial software. A quick overview of these software and their applications is detailed in this section.

VMAP designed by Humphreys [35] is available upon request. It is a complement to the HKL post-treatment software. Orientation maps, pole figures, identification of high and low angle boundaries, and mis-orientation are some of its features.

Another visualization program is *MTEX*, a quantitative texture analysis toolbox for MATLAB [36]. It uses MATLAB computing and plotting capabilities to calculate pole figures, orientation distribution functions (ODF) and different representations of EBSD maps from Euler angles, Rodriguez, axis-angle, *etc*. Scripting to process many data sets is possible via the MATLAB interface. This toolbox is an active open-source project.

Another open source project is *open-ebsd*. It is dedicated to the analysis and visualization of three dimensional EBSD data; 3D EBSD consists of the acquisition of several slices of the same area. This is often performed with a dual beam microscope (combination of a focused ion beam column with a SEM). It implements correction algorithms for misindexed data points, misalignment between slices, clean-up procedures, and grain detection for 3D data sets.

ARPGE (Automatic Reconstruction of Parent Grains from EBSD data) is a program to automatically reconstruct parent grains from orientation relationships [37]. For example, prior austenite grains of a bainitic steel using the Nishiyama-Wassermann orientation relationship. This reconstruction is performed in three steps: (i) identification of the grains in the EBSD mapping (referred to as daughter grains) (ii) nucleation of parent grains sites according to the selected orientation relationship(s) (iii) growth of

Quality Metric	**Equation**	**Variables**
Average	$Q = \frac{1}{WH} \sum_{i=0}^{W-1} \sum_{j=0}^{H-1} I_{ij}$	W: width of the pattern H: height of the pattern I_{ij}: intensity of the pixel (i, j)
Standard Deviation	$Q = \sqrt{\frac{1}{WH-1} \sum_{i=0}^{W-1} \sum_{j=0}^{H-1} \left(I_{ij} - \bar{I}\right)}$	
Entropy	$Q = -\sum_{i=1}^{N} P_i \ln P_i$	P_i: the probability of having a pixel with the color i N: number of color
Fourier	$I = \frac{\sum_{u=-n/2}^{n/2-1} \sum_{v=-n/2}^{n/2-1} S(u,v)(u^2+v^2)}{\sum_{u=-n/2}^{n/2-1} \sum_{v=-n/2}^{n/2-1} S(u,v)}$ $I_{\max} = \frac{1}{n^2} \sum_{u=-n/2}^{n/2-1} \sum_{v=-n/2}^{n/2-1} (u^2 + v^2)$ $Q = 1 - \frac{I}{I_{\max}}$	$S(u, v)$: power spectrum (u, v): coordinate in the Fourier transform n: width and height of the Fourier transform
Signal to noise ratio	$r = \frac{\frac{1}{N} \sum_{i=0}^{N-1} (x_i - \bar{x})(y_i - \bar{y})}{\sqrt{\frac{1}{N} \sum_{i=0}^{N-1} (x_i - \bar{x})^2 \frac{1}{N} \sum_{i=0}^{N-1} (y_i - \bar{y})^2}}$ $Q = \frac{r}{1-r}$	x: pixels of image 1 $\bar{x}$: average of the pixels of image 1 y: pixels of image 2 $\bar{y}$: average of the pixels of image 2 r: cross-correlation between image 1 and 2
Image quality	$Q = \frac{1}{N} \sum_{i=0}^{N-1} H(\theta_i, \rho_i)$	N: number of detected Hough peaks $H(\theta_i, \rho_i)$: intensity of Hough peak i
Pattern quality	$Q = \frac{1}{3\sigma_h} \sum_{i=0}^{2} H(\theta_i, \rho_i)$	σ_h: standard deviation of the Hough space $H(\theta_i, \rho_i)$: intensity of Hough peak i (decreasing order)
Band contrast	$Q = H(\theta_0, \rho_0) - H(\theta_6, \rho_6)$	$H(\theta_i, \rho_i)$: intensity of Hough peak i (decreasing order)
Band slope	$Q = ?$	

Table 2.1: Definitions of quality metrics found in the literature.

the parent grains up to a specified tolerance angle. The software is sold by the French Atomic Energy and Alternative Energies Commission (CEA).

CrossCourt is the software developed following the publication of the article on lattice strain measurement by Wilkinson and Dingley [38]. Using a cross-correlation between the a priori recorded diffraction patterns, the software calculates the strain and lattice rotation tensor as well as the local strain to a prevision of 1×10^{-4} radians. *CrossCourt 3.0* is commercially distributed by the BLG Productions company.

Finally, *ACOM*, Automated Crystal lattice Orientation Mapping, is a hardware and software package developed by Schwarzer from TU Clausthal in Germany. As described in a review paper [9] and in a more recent article [7], it is a complete replacement of commercial EBSD software as it offers the integration between the microscope, camera and acquisition software as well as the indexing of the diffraction patterns. To our knowledge, this system is not distributed and is only used for his personal needs.

Chapter 3

Simulation Engine

Diffraction patterns acquired by an EBSD system are influenced by many factors which ultimately impact the results obtained during an acquisition. The five principal ones are: (i) the crystalline lattice, (ii) the orientation of the crystal, (iii) the electron beam energy, (iv) the position of the different components inside the microscope (beam, sample and camera), and (v) the acquisition parameters. Understanding the effects of these factors on the formation of diffraction patterns is an important first step towards the development of an analysis engine. The choice of the operations and their parameters in the analysis engine are dependent on the intrinsic characteristics of diffraction patterns.

To evaluate these characteristics, a simulation engine was developed to create computer-generated diffraction patterns. All of the aforementioned factors could be controlled in the engine. For simplicity, the kinematic diffraction model [39] is used in this engine instead of the more complete, but more computationally intensive, dynamic diffraction theory as described by Winkelmann [40]. The latter would, however, offer a much closer match to the diffraction patterns recorded experimentally. Nevertheless, the simulated patterns presented in this work can be used as a benchmarking tool to evaluate the algorithms used inside the analysis engine.

This chapter discusses the calculations involved in the generation of a diffraction pattern from crystallographic considerations to a graphical representation of the Kikuchi bands. An overview of the graphical interface designed to facilitate the simulation of such patterns will then be presented. We will conclude this chapter by using the simulated patterns to evaluate the effect of noise and band sharpness on different quality metrics. This study is a first step towards the quantitative evaluation of deformation induced during metallographic preparation, which will be discussed in a later chapter.

3.1 Generation of Diffraction Patterns

In the formation of a diffraction pattern, three questions must be answered: (i) which crystallographic planes are diffracting? (ii) what is their intensity? (iii) how are they represented in a diffraction pattern? The first two questions are related since a plane is said to be diffracting if its intensity is greater than zero. To calculate the intensity, the crystal structure of the specimen must be taken into consideration as well as the position of the atoms inside the lattice. The term "reflector" is used to represent a diffracting plane with its associated intensity. The calculations required to find the reflectors for a given system is discussed in the next section. The answer to the last question depends on the relative position of the specimen with respect to the acquisition camera as well as the orientation of the crystal inside the specimen. The process of representing a reflector in a diffraction pattern is explained in the later section.

3.1.1 Reflectors

The kinematic theory stipulates that the diffracting intensity, I, of a plane (hkl) is proportional to the square of the structure factor, F_{hkl}, given in Equation 3.1,

$$I \propto |F_{hkl}|^2 = \left| \sum_i^N f_i(hkl) \exp\left\{2\pi i \left[(h,k,l)\cdot(x_i,y_i,z_i)\right]\right\} \right|^2 \tag{3.1}$$

where $f_i(hkl)$ is the atomic structure factor of atom i for the plane (hkl) and (x_i, y_i, z_i) is the position of atom i in the lattice containing N atoms [39]. The structure factor is the scattering power for the whole crystal which includes the contribution of each atom in the lattice. To find the intensity of all the possible crystallographic planes, two parameters are required: the position of the atoms in the lattice and the atomic structure factor for these atoms.

The position of the atoms will depend on the analyzed phase, but more specifically on the space group of the phase which gives the symmetry equivalent positions. It is important to consider all the possible positions (general and symmetry equivalent) in the calculation of the structure factor to reveal the systematic absences created by lattice centering and the translational symmetry elements. For a given phase, the engine therefore requires the user to input the general positions of the atoms and the associated space group. The symmetry equivalent positions are automatically generated before performing the calculations, and are obtained by applying different transformations related with the symmetry elements associated with the space group. Each consists of a matrix

and a translation vector. The list of these transformations was taken from the *Python Macromolecular Library (mmLib)* [41].

The atomic scattering factor is the experimentally measured scattering power of individual atoms. It is dependent on the atomic number and the interatomic plane spacing. We shall pause the explanation of the atomic scattering factor to introduce the interatomic plane spacing.

The spacing between two planes of atoms is simply the distance between two parallel crystallographic planes. It is calculated for any crystal system by first calculating the metrical matrix, G, of the unit cell. The metrical matrix is used to express the unit cell coordinate system ($\vec{a}$, $\vec{b}$ and $\vec{c}$ basis) in a conventional orthonormal coordinate system [19]. The latter is referred to as the reciprocal space of the lattice. Equation 3.2 gives the formulation of the metrical matrix, where a, b and c are the lattice parameters in angstroms and α, β, γ are the angles between the bases of the unit cell coordinate system.

$$G = \begin{bmatrix} a^2 & ab\cos\gamma & ac\cos\beta \\ ab\cos\gamma & b^2 & bc\cos\alpha \\ ac\cos\beta & bc\cos\alpha & c^2 \end{bmatrix} \tag{3.2}$$

With this matrix, the spacing of the plane (hkl), d, for any crystal system is simply:

$$s^2 = \begin{pmatrix} h & k & l \end{pmatrix} G^{-1} \begin{pmatrix} h \\ k \\ l \end{pmatrix} \tag{3.3}$$

$$d = \frac{1}{s} \tag{3.4}$$

Given the plane spacing and knowing the atomic number of a given atom, the atomic scattering factor can be obtained from the tabulated values found in the International Tables for Crystallography [42]. In this reference, the coefficients of an exponential fit of the atomic scattering factor curves are given to facilitate their use in algorithms such as this simulation engine. Figure 3.1 shows the variation of the atomic scattering factors as a function of the inverse of the plane spacing for copper, iron and titanium.

The atomic scattering factor decreases as the plane spacing decreases. The plane spacing also decreases as the indices of a plane increases. Therefore, the most intense Kikuchi bands in a diffraction pattern will be those with small indices. For example, the plane spacing for a (111) plane of silicon has a plane spacing of 3.135 Å whereas the plane (222) has a plane spacing of 1.568 Å. To find all the reflectors, one can start by

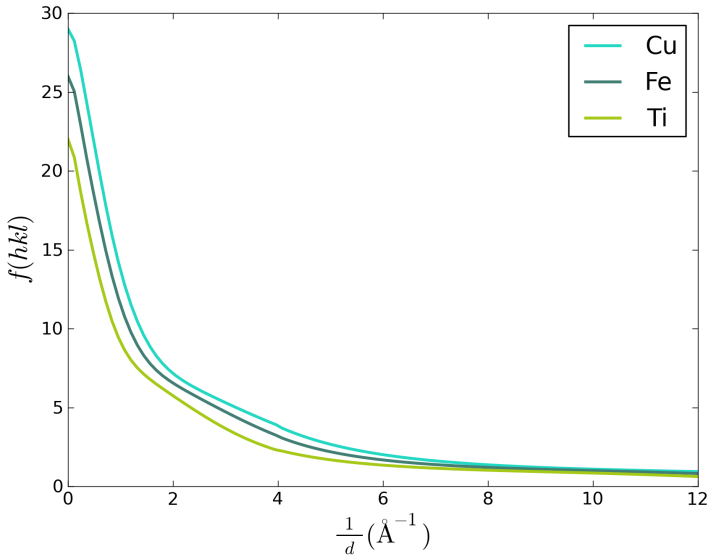

Figure 3.1: Variation of the atomic scattering factor as a function of the inverse plane spacing for copper, iron and titanium.

evaluating the intensity of the {100}, {110}, {111}, {200} plane families and steadily increase the indices towards planes with lower plane spacing. If a plane has an intensity different than zero, it is added to the list of reflectors. The reflectors are ordered from the most intense to the least intense reflector, since bright Kikuchi bands have a greater probability of being detected than the darker bands.

3.1.2 Reference Frame

Another consideration before drawing the Kikuchi bands in the diffraction pattern is the reference frame or coordinate system in which the specimen and camera are positioned. The relative location between the two will determine the position of the Kikuchi bands. We define our reference frame as follows: the z-axis pointing towards the pole piece of the microscope, the y-axis pointing in the direction of the camera and the x-axis defined by the right hand rule. Depending on the configuration in the microscope, the camera could be moved to another position via a rotation transformation. The position of the camera is given by a translation vector from the origin. To follow the typical EBSD nomenclature, the detector distance, $\mathcal{DD}$, is the distance along the y-axis between the origin and the camera, and the pattern center, $\mathcal{PC}$, is the x and z coordinates of the translation vector.

For the sake of our simulation engine, the intersection point between the beam and the specimen is taken to coincide with the origin of the reference frame. Also, the orientation that is used in the simulation is assumed to be the rotation of the crystal after the correction for specimen alignment in the reference frame and the 70° tilt. In other words, the orientation of the simulation is not the orientation of the crystal in the specimen. It is the crystal orientation that was adjusted with respect to the sample reference frame and then tilted to 70°.

3.1.3 Kikuchi Band

With the list of reflectors, the Kikuchi bands can be drawn inside a canvas to create the diffraction pattern. The method used to draw the bands first finds the equation of the line passing through the middle of the band. The width can then be calculated to draw the complete band. The normal to the plane (hkl) is $\vec{n} = (h, k, l)$ and the equation of that plane passing through the origin is:

$$\vec{n} \cdot (x, y, z) = 0 \tag{3.5}$$

$$hx + ky + lz = 0 \tag{3.6}$$

The intersection of this plane with the plane of the acquisition camera is a line corresponding to the middle of the band created by this plane. To find the line equation, we can replace (x, y, z) in Equation 3.6 by $(x, \mathcal{DD}, z)$ since y coordinate is fixed at the detector distance $\mathcal{DD}$:

$$n_x x + n_y \mathcal{DD} + n_z z = 0 \tag{3.7}$$

$$z = -\frac{n_x}{n_z} x - \frac{n_y}{n_z} \mathcal{DD} \tag{3.8}$$

Equation 3.8 is incomplete, because it does not take into account the possible translation of the camera in the x-z plane (*i.e.* the pattern center). With this correction, x coordinate becomes $x - \mathcal{PC}_x$ and $z \to z - \mathcal{PC}_z$. Rewriting the equation, we obtain:

$$z = \left(-\frac{n_x}{n_z}\right) x + \left(\frac{n_x}{n_z}\mathcal{PC}_x - \frac{n_y}{n_z}\mathcal{DD} + \mathcal{PC}_z\right) \tag{3.9}$$

The slope of the intersecting line is therefore $m = -\frac{n_x}{n_z}$ and the intercept $k = \frac{n_x}{n_z}\mathcal{PC}_x - \frac{n_y}{n_z}\mathcal{DD} + \mathcal{PC}_z$.

Equation 3.9 is undetermined when $n_z = 0$. This situations corresponds to a vertical line $x =$ constant. By solving Equation 3.7 with $n_z = 0$, we obtain:

$$n_x(x - \mathcal{PC}_x) + n_y\mathcal{DD} + (0)(z - \mathcal{PC}_x) = 0 \tag{3.10}$$

$$x = -\frac{n_y}{n_x}\mathcal{DD} + \mathcal{PC}_x \tag{3.11}$$

Again there is a special case when $n_z = 0$ and $n_x = 0$, which corresponds to a plane parallel to the detector's plane. There is of course no Kikuchi band for this case.

Now, to determine the width of a Kikuchi band, we need to determine the scattering angle θ using Bragg's Law (Equation 2.1). The wavelength λ is determined from the electron's incident energy (considering relativistic effects) and the plane spacing d from Equation 3.4.

The intersection of the two Kossel cones with the camera determines the width of a Kikuchi band (Figure 2.1). The intersection of a cone with a plane results in an hyperbola. However, as mentioned previously, since the scattering angle is small for electron energies used in SEM, the hyperbolae can be approximated as two straight lines. To simplify the calculations, this approximation is used and the cones are replaced by two planes separated by an angle 2θ.

Figure 3.2 illustrates the reference frame and coordinates that will be used to geometrically solve the width of a Kikuchi band. Note that in Figure 3.2, the origin was translated to the pattern center $(\mathcal{PC}_x, \mathcal{DD}, \mathcal{PC}_z)$ to facilitate the calculations by establishing easier geometrical relationships with respect to the camera (illustrated by a green rectangle). The point of incidence of the electron beam is then referred to as point $\mathcal{I}$. Point $\mathcal{A}$ and $\mathcal{B}$ are two points along the line in the middle of the Kikuchi band. Let $\vec{N}$ be the normal of the plane formed by points $\mathcal{I}$, $\mathcal{A}$ and $\mathcal{B}$. It also corresponds to the normal of the crystallographic plane. The point $\mathcal{P}$ is also along the same line but it is located at the half distance between the two inflexion points of the hyperbolas. In other words, it is the point where the distance between the two hyperbolae would be at its minimum. The points $\mathcal{I}$, $\mathcal{P}'$ and $\mathcal{P}''$ are located on the same line, which is at an angle θ (scattering angle in Equation 2.1) from the vector $\overrightarrow{\mathcal{IP}}$. The norm of the vector $\overrightarrow{\mathcal{PP}''}$ is therefore equal to half the width of the Kikuchi band. The other half would be the norm of the vector $\overrightarrow{\mathcal{PP}'''}$ (not shown in Figure 3.2) which would be located below point $\mathcal{P}$.

To convert the scattering angle θ to a distance on the camera equal to half the width of the Kikuchi band, we first find the smallest distance between the Kikuchi line and the point of incidence $\mathcal{I}$. This is geometrically expressed by the norm of the vector $\overrightarrow{\mathcal{IP}}$. The

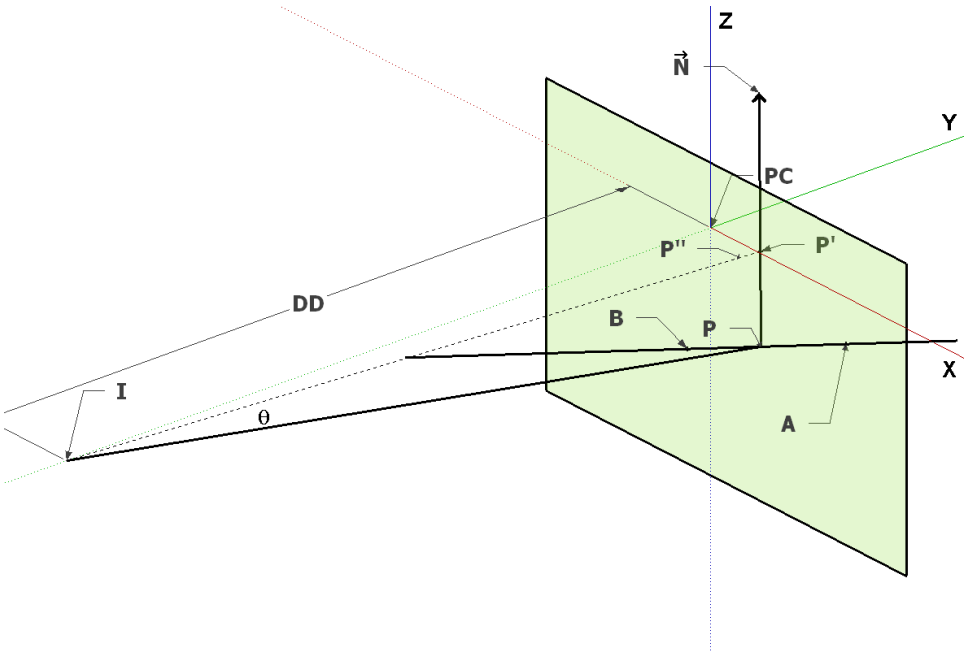

Figure 3.2: Schematic representation of a diffracting crystallographic plane ($\vec{N}$), the camera screen (green rectangle) and the point of incidence (I) of the electrons on the sample. Point $\mathcal{A}$ and $\mathcal{B}$ are two points along the line in the middle of the Kikuchi band.

distance between a point and a line is given by the general Equation 3.12 [43], where $\vec{x}_0$ is the point, and $\vec{x}_1$ and $\vec{x}_2$ are two points on the line.

$$\left\|\overrightarrow{I\mathcal{P}}\right\| = \frac{\|(\vec{x}_2 - \vec{x}_1) \times (\vec{x}_1 - \vec{x}_0)\|}{\|\vec{x}_2 - \vec{x}_1\|} \tag{3.12}$$

In our reference frame, $\vec{x}_0$ is the point of incidence I, and $\vec{x}_1$ and $\vec{x}_2$, are two points on the Kikuchi line ($\mathcal{A}$ and $\mathcal{B}$). The selection of these two points depend on the slope and intercept of the middle line. Figure 3.3 summarizes how point $\mathcal{A}$ and $\mathcal{B}$ are selected.

Equation 3.12 can be re-written using the newly defined points.

$$\left\|\overrightarrow{I\mathcal{P}}\right\| = \frac{\left\|\vec{N}\right\|}{\left\|\overrightarrow{\mathcal{AB}}\right\|} \tag{3.13}$$

From Figure 3.2, we can deduce the following orthogonality relations:

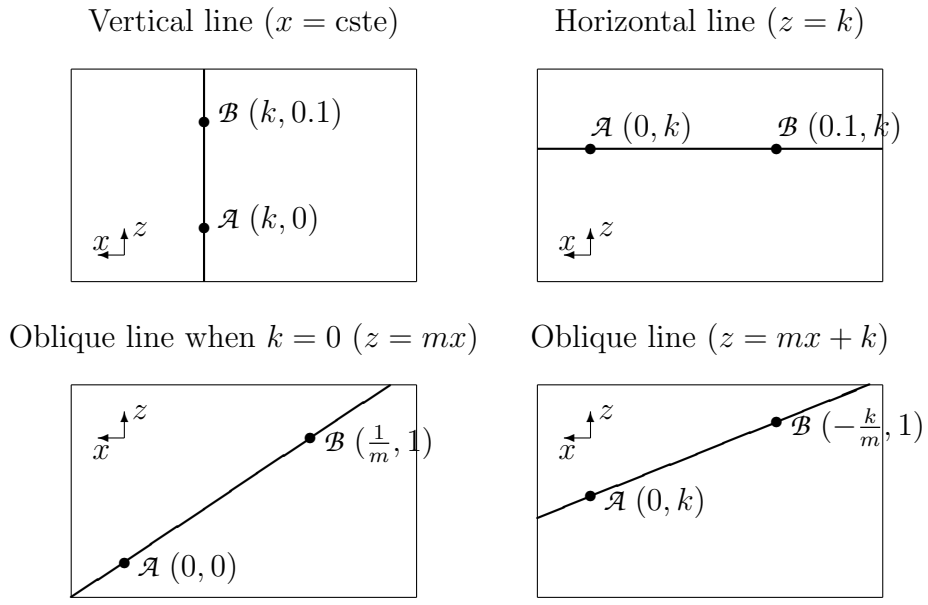

Figure 3.3: Four different representations a line $y = mx + k$ with two points.

$$\overrightarrow{\mathcal{IP}} \cdot \vec{N} = 0\ (\angle \mathcal{IPP}' = 90°) \tag{3.14}$$

$$\overrightarrow{\mathcal{AB}} \cdot \vec{N} = 0\ (\angle \mathcal{APP}' = \angle \mathcal{BPP}' = 90°) \tag{3.15}$$

$$\overrightarrow{\mathcal{IP}} \cdot \overrightarrow{\mathcal{AB}} = 0\ (\angle \mathcal{IPA} = \angle \mathcal{IPB} = 90°) \tag{3.16}$$

Except when the middle line passes through the pattern center, the normal $\vec{N}$ is never parallel to the screen of the camera, forming an angle $\angle \mathcal{P}''\mathcal{PP}'$. The angle is zero when $\mathcal{P}$ is located at the pattern center. We shall refer to this angle as α.

To solve for the half width of the band, $\left\|\overrightarrow{\mathcal{PP}''}\right\|$, we introduce the vector $\vec{S}$, which is defined as a vector parallel to the detector screen and perpendicular to $\overrightarrow{\mathcal{AB}}$. The coordinates of $\vec{S}$ are therefore $(N_x, 0, N_z)$. Figure 3.4, which is a projection in the x-direction of Figure 3.2, illustrates the definition of $\vec{S}$ and α.

The angle α can be calculated using the dot product of vectors $\vec{S}$ and $\vec{N}$.

$$\alpha = \arccos \frac{\vec{S} \cdot \vec{N}}{\left\|\vec{S}\right\| \left\|\vec{N}\right\|} \tag{3.17}$$

The vectors $\vec{S}$ and $\vec{N}$ form a scalene triangle $\triangle \mathcal{PP}'\mathcal{P}''$. Knowing that the $\angle \mathcal{PP}'\mathcal{P}'' = 90° - \theta$ and $\angle \mathcal{P}'\mathcal{PP}'' = \alpha$, the $\angle \mathcal{PP}''\mathcal{P}'$ is equal to $90° + \theta - \alpha$, the Sine Law can be used to find the following relation:

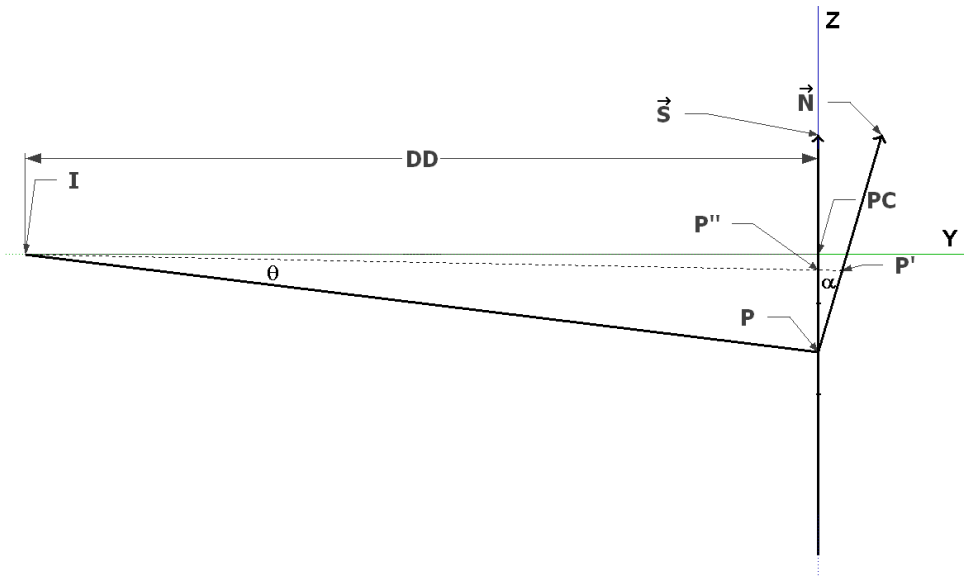

Figure 3.4: Projection of Figure 3.2 to calculate the upper half-width of the Kikuchi band ($\|\mathcal{P}''\|$).

$$\frac{\sin\left(\frac{\pi}{2}+\theta-\alpha\right)}{\left\|\overrightarrow{\mathcal{P}\mathcal{P}'}\right\|}=\frac{\sin\left(\frac{\pi}{2}-\theta\right)}{\left\|\overrightarrow{\mathcal{P}\mathcal{P}''}\right\|} \tag{3.18}$$

Knowing that $\left\|\overrightarrow{\mathcal{P}\mathcal{P}'}\right\| = \left\|\overrightarrow{I\mathcal{P}}\right\| \tan\theta$ and solving for $\left\|\overrightarrow{\mathcal{P}\mathcal{P}''}\right\|$, the upper half width of the Kikuchi band, we obtain:

$$\left\|\overrightarrow{\mathcal{P}\mathcal{P}''}\right\| = \left\|\overrightarrow{I\mathcal{P}}\right\| \tan\theta \frac{\sin\left(\frac{\pi}{2}-\theta\right)}{\sin\left(\frac{\pi}{2}+\theta-\alpha\right)} = \left\|\overrightarrow{I\mathcal{P}}\right\| \tan\theta \frac{\cos\theta}{\cos\left(\alpha-\theta\right)} = \left\|\overrightarrow{I\mathcal{P}}\right\| \frac{\sin\theta}{\cos\left(\alpha-\theta\right)} \tag{3.19}$$

As for the lower half width, we can use the same relationships used above to calculate its value:

$$\left\|\overrightarrow{\mathcal{P}\mathcal{P}'''}\right\| = \left\|\overrightarrow{I\mathcal{P}}\right\| \frac{\sin\theta}{\cos\left(\alpha+\theta\right)} \tag{3.20}$$

Equations 3.19 and 3.20 show that the half-widths of a Kikuchi band are not equal. When drawing filled Kikuchi bands, we approximate that the full width is equal to the sum of the half-widths. The error on this approximation can be written as a function of α and θ:

$$\begin{aligned} \text{error} &= \frac{\left\|\overrightarrow{\mathcal{P}\mathcal{P}'''}\right\| - \left\|\overrightarrow{\mathcal{P}\mathcal{P}''}\right\|}{\left\|\overrightarrow{\mathcal{P}\mathcal{P}'''}\right\| + \left\|\overrightarrow{\mathcal{P}\mathcal{P}''}\right\|} \\ &= \tan\alpha \tan\theta \end{aligned} \tag{3.21}$$

The error will be greater for large bands (large θ) and for bands located far from the pattern center, or geometrically speaking, for bands with a large α angle. To estimate the order of magnitude of this error, we calculate the maximum error based on typical values of α and θ. Assuming that the pattern center is at the center of the camera, the band with the greatest error is located at a distance equal to the radius R of the camera. From Figure 3.4, R can be visualized as $\left\|\overrightarrow{\mathcal{P}\ \mathcal{P}\mathcal{C}}\right\|$. For this limiting case, it can be shown that:

$$\tan\alpha = \frac{R}{\mathcal{D}\mathcal{D}} \tag{3.22}$$

As mentioned previously, the scattering angle θ is very small due to the small wavelength of the incident electrons. Using the small angle approximation, we obtained $\tan\theta \approx \theta$. Equation 3.22 can be re-written as:

$$\text{error} = \frac{R\theta}{\mathcal{D}\mathcal{D}} \tag{3.23}$$

The position of the EBSD camera is usually close to the sample. A good estimate for the detector distance would be that $\mathcal{D}\mathcal{D} = R$. Using Bragg's Law (Equation 2.1), the scattering angle for the (111) crystallographic plane of silicon is equal to 0.013 32 rad. Therefore, the maximum error is approximately equal to 1%, which confirms that our initial assumption has an negligible effect of the position of the Kikuchi bands in the diffraction pattern.

The interior of the band is filled with the diffracting intensity calculated with the structure factor. For each reflector, this procedure is repeated and the bands are drawn one on top of the other. To prevent over-saturation of the image, the intensity of the pattern is normalized between the most and least intense band.

3.2 Interface

To facilitate the simulation of diffraction patterns, a simple graphical interface was developed to select the parameters. The interface allows the simulation of many diffraction

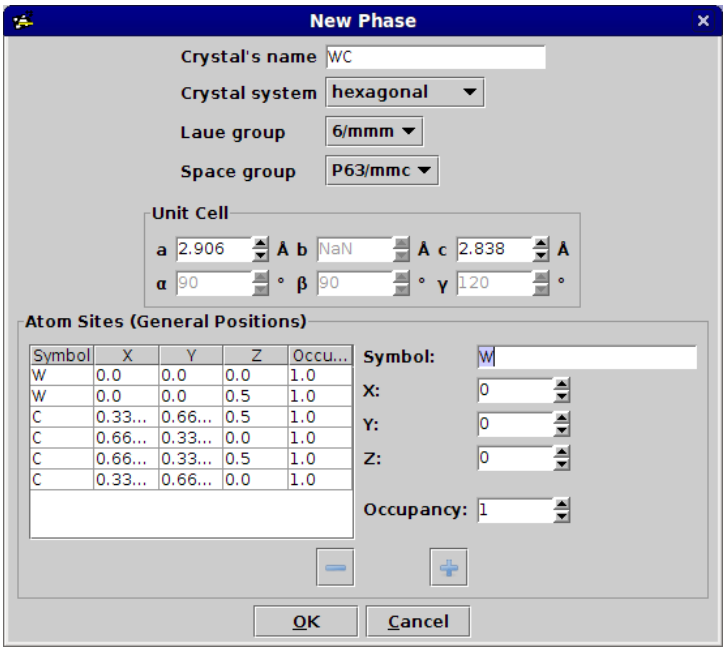

Figure 3.5: Screenshot of the dialog to create a new phase

patterns at once to evaluate the combined effect of the parameters. First, the user must select the phase(s) for the simulation by either opening an existing phase, manually creating a new one or importing one from a Crystallography Information File (CIF). The latter is the recognized format from the International Union of Crystallography. Online databases contain thousands of crystal structure in the material and geological world saved in this file format [44, 45]. If a phase cannot be found, a dialog guides the user through inputting the lattice parameters and angles, space group and position of the atoms (Figure 3.5).

The other parameters of the simulation are the energy of the electron beam, the relative position of the camera, the size of the diffraction pattern, the scattering factors and the orientation of the crystal. A useful feature of the interface is the random orientations generator, which allows for the creation of many different diffraction patterns. Using Gruber's method [46], a random orientation is generated from three random numbers (r_1, r_2 and r_3) ranging between 0 and 1. As the rest of the orientation representations in EBSD-Image, the method creates a quaternion (see Appendix C) representing the orientation as follows:

$$\mathcal{Q} = \left[\!\!\left[\frac{\cos(2\pi r_1)}{\sqrt{r_3}}, \frac{\sin(2\pi r_2)}{\sqrt{1-r_3}}, \frac{\cos(2\pi r_2)}{\sqrt{1-r_3}}, \frac{\sin(2\pi r_1)}{\sqrt{r_3}} \right]\!\!\right] \tag{3.24}$$

The output of the simulation engine is either a list of grayscale images, one for each diffraction pattern, or a SMP file (a specific file format for the analysis engine which will be discussed later).

3.3 Evaluation of Quality Metrics

Quality metrics are designed to evaluate the quality of the diffraction pattern as the human eye would. In other words, the algorithm behind a quality metric is performing calculations on the diffraction pattern, its Hough transform or its detected peaks to obtain a number representing the overall quality of the pattern. Many different algorithms have been developed to perform this task. As we will show in this demonstration, they all have different sensitivity and are influenced by different factors.

To evaluate quality metrics, a set of patterns were simulated at different orientations but at the same energy and camera position. These factors would influence the width of the Kikuchi bands. For our comparison, it is better to keep them constant to evaluate the quality metrics using a fixed set of experimental conditions. The use of different orientations is, however, important since quality metrics are influenced by the intensity of the different Kikuchi bands present in the pattern [28]. As simulated, the patterns are assumed to have the highest possible quality. To deteriorate their quality, two techniques were used: random Gaussian noise and a smoothing filter. The former consists of randomly varying the intensity of each pixel in an image. The variation is based on a Gaussian distribution with a specified standard deviation. The greater the standard deviation, the greater the intensity variation and the noisier the image. Figure 3.6 and 3.7 respectively show the original simulated pattern and the same simulated pattern where a random Gaussian noise with standard deviation of 60 was applied.

The second method, the smoothing filter, has the effect of blurring the Kikuchi bands [14]. The filter is replacing the intensity of a pixel by the average of its neighbors. When applied on the whole image, the effect is a decrease in the sharpness of the edges. As the number neighbors used in the calculations is increased, the greater the smoothing and the blurring of the image. Figure 3.8 shows the result of a 9x9 smoothing filter on Figure 3.6.

To evaluate the quality metrics, random Gaussian noises with standard deviations from 0 to 100 and smoothing filters with kernel sizes from 3x3 to 19x19, will be independently applied to a set of ten simulated patterns. Then the different quality metrics will be calculated on each deteriorated pattern. To remove the dependence of the quality

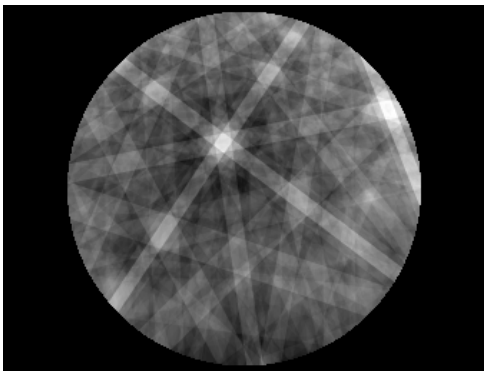

Figure 3.6: Simulated diffraction pattern.

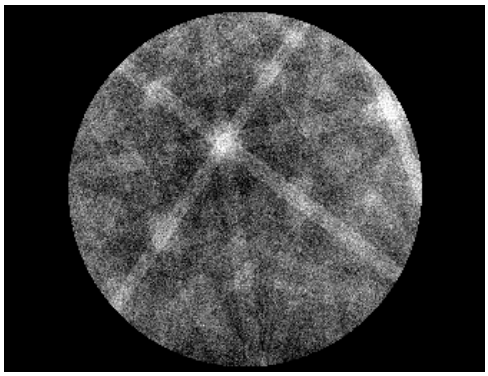

Figure 3.7: Simulated diffraction pattern after the addition of a random Gaussian noise with a standard deviation of 60.

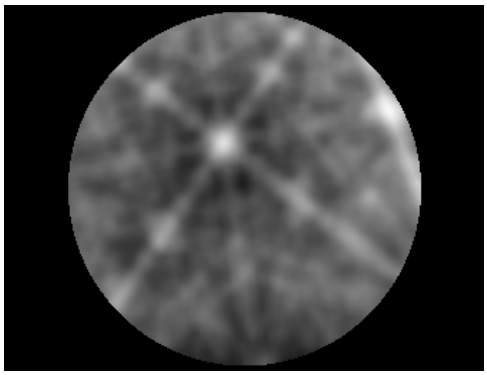

Figure 3.8: Simulated diffraction pattern after the convolution of a 9x9 smoothing filter.

metrics on crystallographic orientation, the values from the simulated patterns at different orientations are averaged for a given mode of deterioration. Since the absolute value of the quality metrics is irrelevant to this analysis, measurements are compared with the initial simulated pattern as a ratio. In other words, the ratio is taken between the quality value at a deterioration level i (Q_i) and the quality value of the original pattern without any deterioration (Q_0). Figure 3.9 illustrates the results for the effect of the random Gaussian noise on the following quality metrics: pattern average, pattern standard deviation, pattern entropy, Fourier transform, signal to noise ratio, image quality, pattern quality index, band contrast and band slope. The last two quality metrics were calculated using the HKL Channel 5 software. Figure 3.10 gives the results for the effect of the smoothing filter on the same quality metrics.

First of all, we expect the trend for any quality metric to be monotonically decreasing

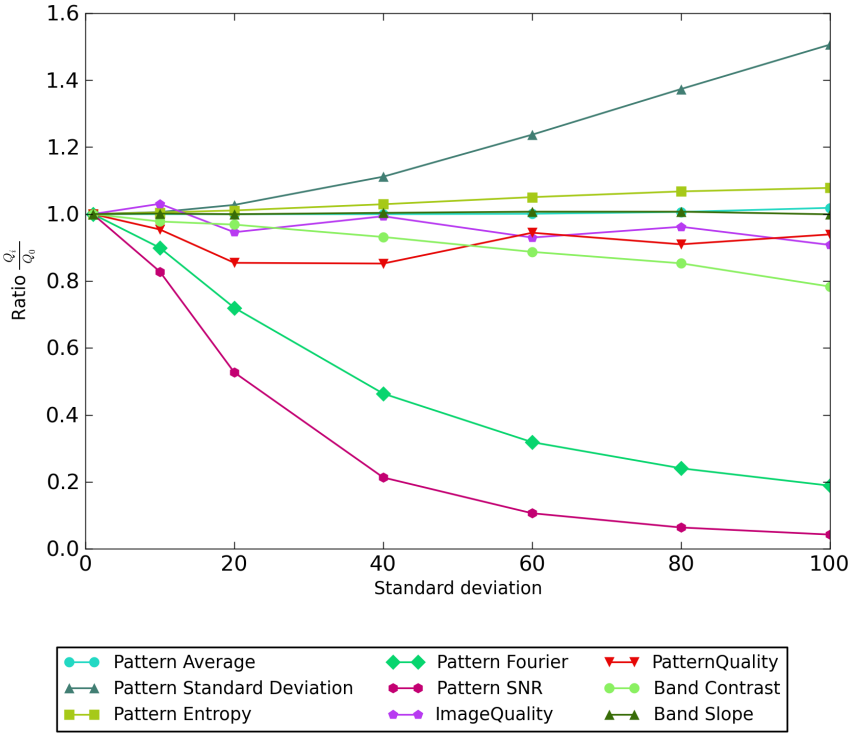

Figure 3.9: Variation of the quality metrics as a function of the standard deviation of the random Gaussian noise.

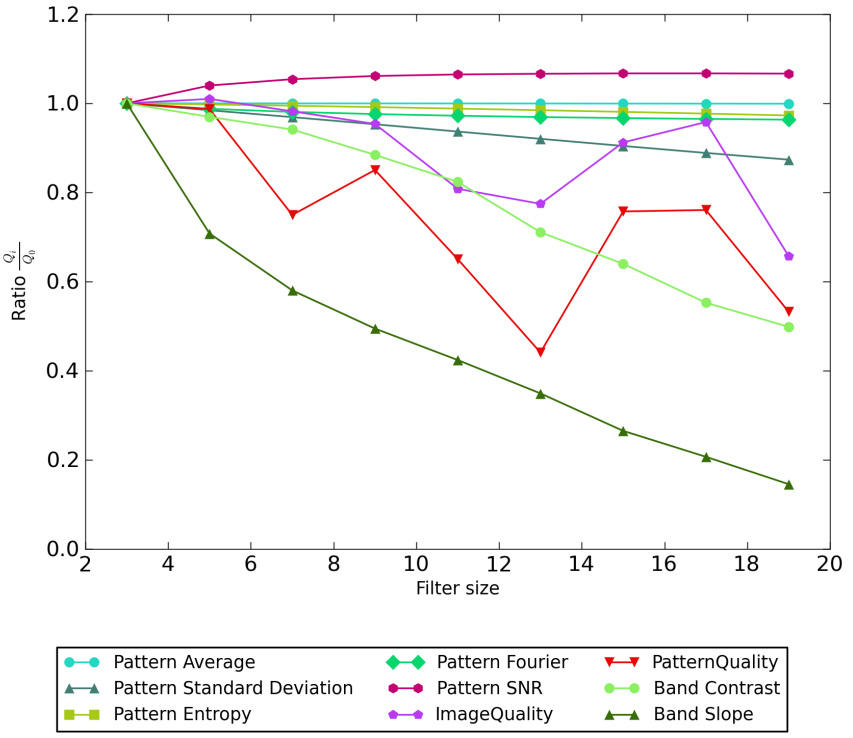

Figure 3.10: Variation of the quality metrics as a function of the size of the kernel for the smoothing filter.

as a function of the noise's standard deviation or the smoothing filter. The overall comparison of these results suggest that most of the quality metrics are more dependent on the sharpness of the Kikuchi bands than on the level of noise in the diffraction pattern. The signal to noise ratio is the exception to this rule. This quality metric provides a good measure of the level of noise, but has an inverse relation with the image's blurring. Since the noise level is constant (not existent) in the smoothed diffraction pattern, an increase of the SNR would indicate an increase of the "signal" of the image. The quality metric related to the Fourier transform of the diffraction pattern is also a good measure of the noise level. In blurred images, it can also correctly evaluate the decrease in quality. However, the ratio between the deteriorated and initial pattern is much less than for the noisy images. We can conclude that it is more sensitive to the noise than the sharpness of the Kikuchi bands. This is the reverse for the band contrast, the image quality and the pattern quality which are insensitive to the noise but show a stronger dependence with the size of the smoothing filter. The decrease of the image and pattern quality metrics is however non-monotonic. These variations could be associated with the fact that they are calculated using the peaks detected in the Hough transform instead of being a direct evaluation of the diffraction pattern. The peaks used in the calculations may vary as the quality decreases and influence the final value. This explanation, however, does not hold for the case of the band contrast and band slope, which are also calculated from the Hough transform. The proprietary nature of these quality metrics prevents us from better understanding their behavior. The standard deviation and entropy of the diffraction pattern provide a good evaluation of the blurring of the Kikuchi bands. Even if their absolute difference between a good and a bad diffraction pattern is smaller than for other quality metrics, such as the band slope, they are proportionally related to the size of the smoothing filter. Finally, the average of the pixels in the diffraction pattern is the only quality metric which seems to be unaffected by the noise or the smoothing filter. This metric is a measure of the average intensity of the diffraction pattern. This value is therefore constant regardless of the deterioration imposed on the diffraction patterns.

In conclusion, the use of simulated patterns to evaluate quality metrics showed that they are more sensitive to the sharpness of the Kikuchi bands rather than the noise level in the diffraction pattern. If the latter is of interest, the signal to noise ratio should be used. Quality metrics directly using the intensity of the pixels in the pattern (standard deviation, entropy, Fourier transform) exhibit a smaller quality different between the before and after deterioration pattern than those calculated from the Hough transform (band contrast, image quality, pattern quality). However, their relation with the level

of deterioration is more proportional. The variation in the quality metrics based on the Hough transform is perhaps related to the detection and identification of the peaks and their intensity. The results of this study will be compared with experimental measurements on deformed samples where we should expect to find a similar gradient of high and low quality diffraction patterns.

Chapter 4

Analysis Engine

The analysis engine is the core of EBSD-Image. It can be summarized as a chain of operations used to process stored EBSD patterns and extract various information from them. Its main objective is to give a high level of flexibility and expandability to the users and serve as a research and development tool for the EBSD community. The analysis engine leaves to the users the choice of operations and their parameters. One can therefore decide which algorithms to use to analyze his/her EBSD patterns. This gain in flexibility is a definite advantage over commercial software, especially in the analysis of non-conventional or more challenging material. The engine is also designed to facilitate the implementation of new algorithms. Advanced users with a basic programming background can create their own operations to analyze their diffraction patterns. More details about these two principal features of the engine will be given in the structure section of this chapter. Another characteristic of the analysis engine, and the whole EBSD-Image project, is the availability of the source code. This transparency removes the black box aspect of commercial software where the algorithms used are proprietary and unknown. By being open source, the analysis engine can be evaluated, criticized and improved by the community for the benefit of all users.

The development of the analysis engine to process electron diffraction patterns (EBSP) can be separated into three parts: (i) the selection of the platform on which the engine will be built upon (ii) the structure of the engine and how an analysis is performed (iii) its implementation inside the graphical and command line interface. Two file formats are also introduced, one to store and manipulate diffraction pattern images and the other to store the results of an analysis. Finally, this chapter will discuss the design choices behind key algorithms of the analysis engine.

4.1 Platform

Many algorithms involved in the processing of electron backscattered diffraction patterns as well as the post-treatment and analysis of EBSD mappings are directly derived from image analysis routines. This includes standard operations such as erosion, dilation, convolution, thresholding and more advanced ones such as the Hough and Fourier transform. It is for this reason that the analysis engine is built on top of the image analysis software, RML-Image (`www.rmlimage.com`), giving the users more tools to analyze their results and extract additional information. This contrasts with other EBSD software which are uniquely designed towards EBSD specific operations. This new software distribution was named EBSD-Image since it is a combination of EBSD and image analysis software.

RML-Image was developed by Marin Lagacé from Hydro-Québec Research Institute and is distributed freely. It consists of an application programming interface (API) and a graphical user interface (GUI), giving the flexibility to run the application on a personal computer as well as on a mainframe. More particularly, it has three main features that were interesting for the elaboration of EBSD-Image: (i) written in a cross-platform language, (ii) flexible plug-in and macro interface, and (iii) comprehensible structure for data storage.

RML-Image, and consequently EBSD-Image, is written in Java, a well established cross-platform and object-oriented language with a large and active community. This gives the ability to easily run EBSD-Image on different platforms opens the possibility to do EBSD analysis on distributed heterogeneous systems as it will be discussed in Section 4.4.2. The Java programming language is also in line with the primary objectives of EBSD-Image geared towards flexibility, expandability and ease of development.

Another feature of RML-Image is the pluggable interface and macro scripting. The former gives advanced users the possibility to develop and implement their own specific algorithms directly in the software. Menu items and tool-bar buttons can be customized to quickly access these algorithms. Macro scripting is targeted towards intermediate users who do not want to dive into the core of the software, but would like to run a series of operations automatically. A typical example would be to run the same set of operations on several images.

Finally, RML-Image offers a comprehensible structure for storing and manipulating data. The main abstraction of the software is referred to as a map. It consists of any kind of image or two dimensional array of data. By definition, a map has specified dimensions (width and height) and contains an array of values or pixels. The dimensions

Short name	Long name	Type of pixel	Use(s)
BinMap	Binary map	1-bit (0 or 1)	Thresholding, masks
ByteMap	Byte map	8-bit (0 to 255)	Greyscale images
IdentMap	Identification map	16-bit (0 to 65534)	Objects map
RGBMap	Color map	24-bit	Any color image
RealMap	Real map	32-bit float	Store real values in a map

Table 4.1: Basic types of map in RML-Image.

are expressed in pixels (px). The values can be bytes (8-bit), floats (32-bit), complex numbers, *etc*. In a broader sense, a map is a matrix that can be displayed as an image. The important difference with other image analysis software is that a map in RML-Image can only contain one type of value. A map is therefore a well defined object with distinct properties and implementations. This structure allows algorithms, file handlers, and display interfaces to be specific to one kind of map. Understanding the behavior of any function is simplified since the inputs and outputs of that function are clearly defined by the type of map. Table 4.1 summarizes the basic types of map in RML-Image. For more information on these maps and their use in the image analysis routines, the readers should refer to the RML-Image user manual.

4.2 Structure

The process of analyzing EBSPs, which shall be referred to as an experiment, consists of three steps: (i) taking a series of diffraction patterns (inputs), (ii) performing some operations (engine), and (iii) outputting one or several results (outputs). In other words, for each diffraction pattern in an EBSD mapping, a series of operations is performed on that EBSP and some results are extracted from it. Typical operations can be the Hough transform, peak detection, indexing as well as various other computations. Quality metrics (image quality, band contrast, *etc*.), orientation and phase are a few examples of potential results from the engine. These operations and results are similar to those found in commercial EBSD software. The difference with EBSD-Image lies in the flexibility given to the users, who can choose which operations they want to perform and which results they want to obtain.

An operation is defined as the process of taking one or more inputs and returning one or more outputs. All the operations are designed such that all the inputs/parameters are given default values, but can also be changed by the user. The default values are there to

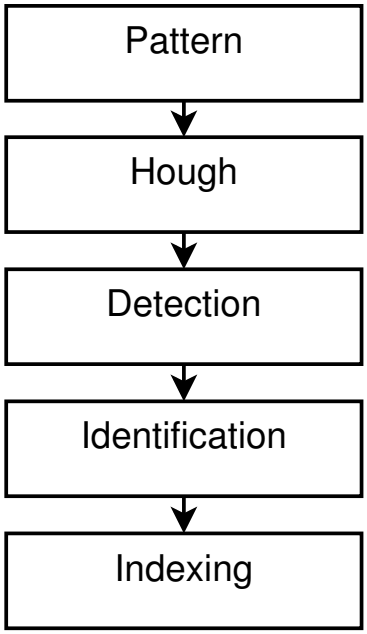

Figure 4.1: Five major steps of the analysis engine.

help less experienced users set-up an experiment. However, experienced users still have the possibility to adapt an experiment to fit his/her needs. The inputs and outputs of the operations are closely related to the type of map. Maps are used to transfer data and information between operations.

4.2.0.1 Steps

To organize the operations, the engine has a specific structure to guide it from one operation to another — it follows a logical chain of events. We divided the process of going from a diffraction pattern to the indexing of that pattern into five major steps (Figure 4.1). This division allows for the separation of operations performed on EBSPs into well defined steps.

The first step is, of course, to load in memory the diffraction pattern as an 8-bit grayscale image. It also involves enhancement algorithms to improve the quality or reduce the noise in the pattern, as well as the selection of a region of interest in the pattern to ignore noisy edges.

The second step is related to the Hough transform, which transforms the pattern's image space into the Hough space. Kikuchi bands inside the pattern are transformed to peaks, which are more easily detected [3]. Different implementations of the Hough transform can be chosen to produce a map representing the Hough space, a *HoughMap*.

The next step consists of locating the peaks in the *HoughMap*. Enhancement algorithms such as a butterfly mask can be used to facilitate the peak detection [3]. Ultimately, a thresholding operation is performed to create a binary map only containing 0's and 1's. The detected peaks are assigned a value of 1, while the rest of the *HoughMap* is set to 0.

With the binary map, the position (θ and ρ) and intensity of each peak can be measured. This is referred to as the identification step. Operations to clean unwanted peaks or to look for specific peaks may be performed as part of this step. The peak intensity can serve to evaluate diffraction quality of a pattern, whereas the position of the peaks, combined with the detector calibration (pattern center and detector distance), will be the inputs of the next step: the indexing.

Using the identified peaks, the orientation and the phase of the diffraction pattern is calculated from the provided phases. A goodness of fit value is also returned to evaluate how closely the solution(s) match(es) the identified peaks. The orientation is saved inside three Euler maps (one map for each angle) or four quaternion maps (one for each coefficient). The phase is saved in a special type of map, a *PhasesMap*.

After each of the five major steps, the result operations can be defined. For instance, the average, standard deviation and entropy of the initial EBSP image can be calculated in the first step after loading the pattern. The image quality, pattern quality or other quality metrics related to the Hough peaks are possible results from the peak identification step. Obviously, the orientation would be a result of the indexing step. All these results are stored inside individual maps (one map per result). In other words, the pixels of the map are the values of the results operations. For an experiment, all these maps are grouped together in a special type of map, an *EbsdMMap*, which shall be discussed later in the file format section. The *EbsdMMap* can be seen as the single final output of the experiment containing all the calculated results.

4.2.0.2 Categories

To clarify the inputs and outputs of each operation in the structure, the five steps are split in four categories of operations, except the first step (Pattern) which only has two categories. The categories follow this logic: (i) a set of operations to pre-process the input(s) (ii) a single operation which defines the step (iii) a set of operations to post-process the output(s) from the single operation (iv) a set of operations to compute and extract result(s) from the output(s). These categories are respectively referred in the software as: (i) pre (ii) op (iii) post and (iv) results. The first step only has the last two

categories, since pre-processing is impossible before loading the diffraction pattern image and the loading operation of the pattern is implicitly defined inside the engine.

The single operation defining the step refers to the main operation of a step. For example, the main operation of the Hough step is the Hough transform. It is also the operation that transforms the type of input(s) the following operations will receive. For instance, the Hough operation takes a grayscale image and transforms it into a *HoughMap*; the peak detection operation takes a *HoughMap* and transforms it into a binary map; the peak identification operation takes a binary map and transforms it into an array of Hough peaks; and finally the indexing operation takes an array of Hough peaks and transforms it in an array of possible solutions. On the contrary, the input(s) and the output(s) of all the operations in the pre and post categories are of the same type. As for the results category, the input(s) maybe different depending on the step, but the output(s) are always of the same type, *i.e.* a number or an array of numbers.

This structure ensures that each operation in a category will always have a common input and the same output(s). With the exception of the second category, all the others can contain zero or many operations. A unique operation is absolutely required for the second category. All these restrictions are strictly enforced internally in the software.

Custom operations can be created by the users. As long as an algorithm respects the implementation of one aforementioned category, it can be inserted into EBSD-Image. Researchers can develop their own algorithms and test them without having to create a full EBSD software. The source code of EBSD-Image is structured and documented to facilitate such development. We invite you to read the developer manual to obtain a complete guide of how to implement new algorithms. The manual gives more details of the analysis engine's structure and conventions to follow.

Table 4.2 summarizes the engine's structure by giving a description of each category as well as some examples of operations.

4.3 File Formats

EBSD-Image introduces two file formats to facilitate the analysis of diffraction patterns and the post-processing of the results obtained from them. They are created since no other publicly known and available file format could provide the desired requirements. Far from being proprietary to EBSD-Image, they are designed to be simple and easily implementable by other software.

Step	Category	Description	Examples
Pattern	Post	Process the diffraction pattern after it being loaded	Mask, binning
	Results	Compute results from the diffraction pattern	Average[1], standard deviation[1], entropy[1], Fourier[2]
Hough	Pre	Process the diffraction pattern before the Hough transform	Median
	Op	Perform the Hough transform	Hough transform[2]
	Post	Process the Hough transform	Crop Hough space
	Results	Compute results from the Hough transform	Range
Detection	Pre	Process the Hough transform prior to the peak detection	Butterfly[2], Contrast expansion
	Op	Detect the peaks in the Hough transform	Top hat[3], standard deviation thresholding
	Post	Process the detected peaks to remove unwanted peaks	Opening
	Results	Compute results from the detected peaks	Shape factor, area, distribution
Identification	Pre	Process detected peaks prior to their identification	Dilation
	Op	Identify Hough peaks (position and intensity) from the detected peaks	Local centroid, center of mass[2]
	Post	Process the identified Hough peaks	Clean-up double peaks
	Results	Compute results from the identified Hough peaks	Image quality[1], pattern quality[4], peaks count
Indexing	Pre	Process the Hough peaks before the indexing	Select most intense peaks
	Op	Index the Hough peaks to potential solutions (phase and orientation)	Automated indexing[2]
	Post	Process the solutions to find the best one	Lowest misfit
	Results	Save orientation and phase of the solution	Euler angles

[1] From Wright and Nowell (2006).
[2] From Krieger Lassen's Ph.D. thesis (1994) .
[3] Implementation from Gonzalez and Woods (2007) .
[4] From Oxford INCA Crystal EBSD software. INCA is a registered trademark of Oxford Instruments plc.

Table 4.2: Definition of the categories in the analysis engine. For each category, typical examples of operations are given in the last column.

4.3.1 Stream Map File (SMP)

Diffraction patterns are the raw data of any EBSD acquisition. All other results such as quality metrics, orientation and phase maps are all derived from these patterns. In HKL Channel 5 and TSL OIM, the patterns are saved as individual files. Even with 100 000+ images, the space required to save all the EBSPs is no longer a problem with current hard drives. However, the number of files stored inside a single folder is a challenge for the operating system. Browsing a folder containing this amount of files is slow and highly inefficient. This problem becomes very apparent when one attempts to move or copy those folders.

To remedy to this situation, we propose a new simple file format to store and access EBSPs: the stream maps or SMP file. The thousands of small image files are replaced by one single, large SMP file. Images are saved in sequence from the upper left corner of a map down to the lower right corner. This eliminates the operating system's problems with listing a large quantity of files in a folder and is perfect for backup of EBSD data. Another important feature is that this file format allows random access to any EBSP inside the SMP. Only the index of the EBSP in the map is required to retrieve it. It prevents the need to load the whole file in memory. Since the images inside the SMP are uncompressed, the process of loading an image is also very quick. EBSD-Image takes care of the conversion from single pattern image files to an SMP file. The process is completely transparent to the user. Ultimately, the content of the SMP file can be exported back to single pattern image files, if needed. Currently, the file handler for this format is written in Java but it could easily be ported to any other programming language. The detailed technical specification of this file format is available in the online documentation.

4.3.2 EBSD multi-map (EbsdMMap)

Typically EBSD software use a proprietary binary file format to store the acquisition parameters, orientations, phases and quality indices (*e.g.* CRC file for HKL Channel 5 and OSC file in TSL OIM). Maps and subsequent calculations such as the grain size are derived from this file. It is therefore impossible for users without these software to display their results. In order to have a more open and flexible file format, EBSD-Image uses a different scheme to store its results. All the results from an experiment can be saved in maps. For example, one map to identify the location of each phase, one map for each of the three Euler angles, one map per quality metric, *etc*. In other words, each type of result is saved in a map. To regroup all these different maps, a new type of map

was created, the *EbsdMMap*. This is an abbreviation for an EBSD multi-map (short for multiple map). Before defining an *EbsdMMap*, we shall first introduce the concept of a multi-map since it differs slightly from a regular map.

A multi-map is an aggregate of different maps that share the same dimensions (width and height). All the maps are given an alias to represent them inside the multi-map. There is no restriction on the type or the number of maps in a multi-map. This concept allows related maps to be kept together and operations to be performed on all of them at the same time. A multi-map is stored on the user's hard drive as a ZIP file. It contains all the maps stored in their respective file format. Another file is also added to link the filename of the map to its alias inside the multi-map. The ZIP file offers the possibility to view all the maps inside the ZIP without using EBSD-Image. In many operating systems such as Microsoft Windows, the files can even be viewed directly within the ZIP without extracting them.

This type of map is particularly appropriate for EBSD since many different results are obtained from a single mapping, and all of these results can be stored inside a multi-map. The *EbsdMMap* object adds two new features to the multi-map: a list of metadata and a set of required maps. Metadata are parameters and properties related to an EBSD acquisition. They can be used to identify and interpret a mapping. At minimum, an *EbsdMMap* must have the following metadata: (i) beam energy (in electron-volt) (ii) magnification of the microscope (iii) tilt of the sample (in radians) (iv) working distance of the microscope (in meters) (v) step size of the mapping in x and y (in meters) (vi) rotation of the sample with respect to the camera (a quaternion) (vii) calibration of the pattern center and detector distance. The metadata are stored in a XML file inside the ZIP. This file format is human-readable and modifiable. It is a well known format for storing metadata. An *EbsdMMap* also requires the presence of five maps inside the multi-map. Four of these represent the crystal's orientation; there is one map for each of the quaternion's coefficients representing the orientation. The fifth map stores the location and the definition of the indexed phases. It is referred to as the *PhasesMap*. These maps are required since the orientation and the phases are the basic results of any EBSD mapping. They are also the basis of many types of post-processing calculations. Hence, these maps cannot be removed from an *EbsdMMap*. If no indexing was performed (*i.e.* no indexing operation was selected in the analysis engine), these maps are still present, but left blank. Examples of other optional maps that could be part of a *EbsdMMap* would be different quality metrics or another representation of the orientation such as the Euler angles.

4.4 Interfaces

To facilitate the setup of an experiment, EBSD-Image offers a simple but powerful graphical interface. The experiment can then be executed inside the graphical interface or sent to a main frame with distributed multiple processors. This section provides an overview of these two possibilities.

4.4.1 Graphical

For a new user, the first step will be to import an EBSD mapping and possibly EBSPs acquired using commercial software. EBSD-Image can import EBSD mappings from HKL Channel 5 and TSL OIM using their respective exportable ASCII format (CTF or ANG file). Along with the acquisition results, acquired EBSPs can be converted to a SMP file. The import wizard collects all the required information to create an EBSD multi-map. This includes the lattice parameters, the symmetry and the position of the atoms for each phase. This information must be entered manually in a dialog since the position of the atoms is not present inside the ASCII files. However, a phase definition can be imported from the standard file format of the International Union of Crystallography, the Crystallography Information File (CIF).

Once imported, the multi-map can be directly loaded inside EBSD-Image. The multi-maps appear in the tree component on the left-hand side of the desktop (Figure 4.2). All the maps present are listed and can be opened by clicking on them. Image analysis routines can be performed on a single map and/or on all the maps inside a multi-map. These include thresholding, boolean operations, identification of features, *etc.*

To run an experiment, a wizard guides the user through the set-up of all the parameters and operations. Preliminary parameters can be imported from previous EBSD acquisitions and will be saved in the EBSD multi-map resulting from the experiment. Some parameters may be optional for some operations, but essential for others. For instance, if no indexing operation is selected, it is pointless to set-up the list of phases and the camera's calibration. The next part of the wizard is to select the location of the diffraction patterns. As mentioned previously, the SMP file is the preferred option. However, a folder containing EBSPs or a single pattern image can also be selected.

The next five panels are to set-up the operations; one panel per main step. Each panel has the same appearance where the available operations are listed on the right while the selected operations appear on the left (Figure 4.3). Operations developed by the user will automatically appear in the available operations' list. When adding an operation to

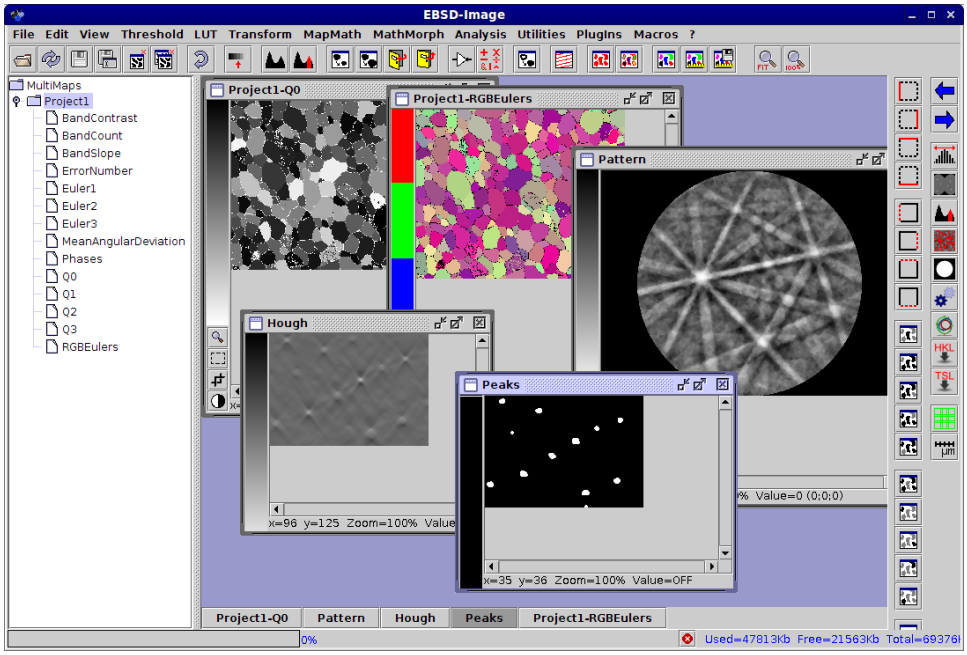

Figure 4.2: Screenshot of the graphical interface showing an opened multi-map and the results of some operations on a diffraction pattern.

the selected list, a dialog may pop up to specify other parameters. The default values are given as a starting point. The definition of the parameters can be found in the online documentation where each operation is explained in detail. It is not required to select an operation for each category. It is however important to realize that the experiment will only execute the operations that are required to obtain the selected results. For example, if a Hough transform operation is selected, but no result operation requires it to be performed, it would not be executed.

The last step of the wizard is to decide how the experiment will be run. The preview mode allows the user to check that all the operations are performed correctly. All the selected operations are executed on one diffraction pattern and the resultant map of each operation is temporarily displayed on the desktop. The diffraction pattern is selected by specifying its index in the mapping. After verifying the results, the user can either launch the experiment on all EBSPs or return to the wizard to modify its operations. By going back to the set-up wizard, the user can also select another diffraction pattern to preview. Another output option is to save the experiment parameters and operations to an XML file. With this file, the experiment can be launched at a later time in the graphical interface or run from a system of distributed multiple processors as will be explained in the following section. The last option is to run the experiment directly on

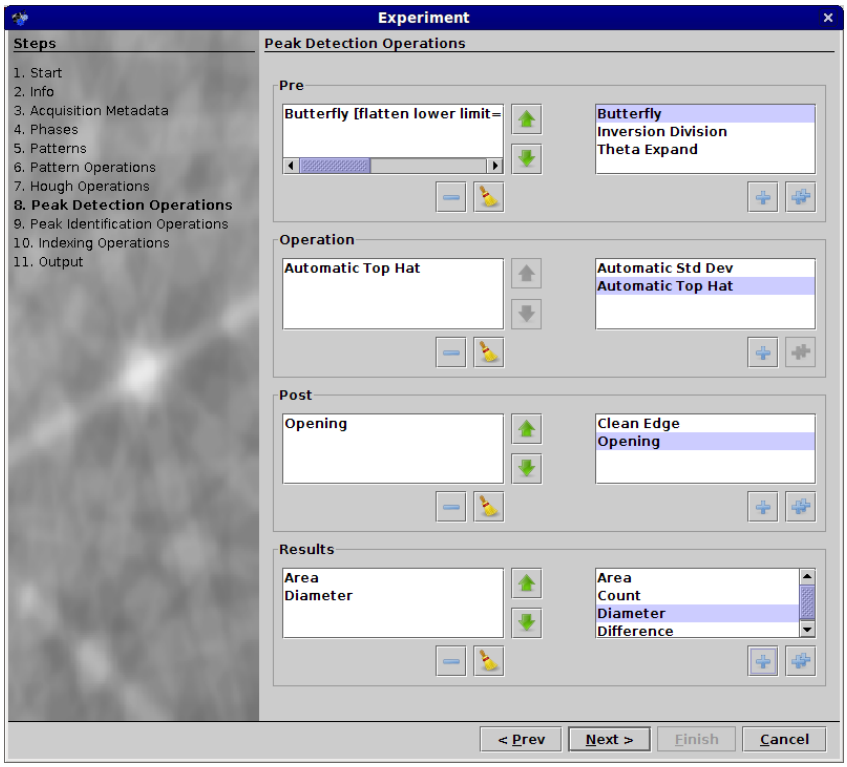

Figure 4.3: Screenshot of the wizard to select the operations of an experiment.

the desktop. A progress bar will then appear to track the progress of the experiment. The user can also visually check the progress by selecting a map from the experiment's multi-map. The results are refreshed every second.

4.4.2 Distributed

The EBSD analysis requires computer-intensive calculations, such as the Hough transform, to be performed on tens of thousands of images. With the current quest for the fastest acquisition camera, the number of diffraction patterns to analyze for a given mapping will keep on increasing, thus requiring more and more computing power. If one wants to benefit from more elaborate, but perhaps slower algorithms to analyze these diffraction patterns, processing large quantities of data can easily become a problem, or at the very least a limitation. Distributed computing on a grid or cluster of computers can be a solution to this problem. A distributed system consists of several processors connected together via an internal network. A program can either use several processors simultaneously (parallel computing) or be run on several processors independently (distributed computing). The latter is particularly well fitted for EBSD analysis since

each diffraction pattern is completely independent from the others. The processing of a diffraction pattern does not require knowledge of the other diffraction patterns in the mapping. The same set of algorithms can be independently applied on each individual diffraction pattern and the results combined only at the end. The main advantage to this kind of system is that the time required to analyze a series of diffraction patterns can be reduced by a factor approximately equal to the number of processors used. An analysis that would take two hours on a single processor computer can be reduced to ten minutes if a distributed system of twelve processors is used.

To facilitate the use of such a system, special routines were developed in EBSD-Image. The distributed interface of EBSD-Image requires the same inputs as the graphical interface, a SMP file and a series of operations. As such, we encourage the user to use the graphical interface to create the SMP file from the acquired stored EBSPs and to set-up the experiment file. The output of the distributed interface is also the same as the graphical interface, an *EbsdMMap* saved in a ZIP which can later be opened inside the graphical interface.

To accommodate different types of distributed systems, the distributed interface consists of three main programs. They perform the following tasks: (i) split the diffraction patterns and the experiment set-up file for each processor (ii) run the analysis on each processor (iii) merge the results into a single output. The first task is necessary to give each processor a unique set of diffraction patterns. Technically, the single SMP file is split into smaller SMP files. If all the processors were loading the diffraction patterns from the same SMP file, this could create concurrency problems and slow down the analysis. The experiment set-up file is automatically adjusted to tell each processor which SMP file to use and which diffraction patterns to analyze. The result of this first task is a series of completely independent experiments. Each experiment is then run in the analysis engine on different processors. An *EbsdMMap* is created for each experiment. Once the analysis of all the experiments is completed, the results are merged by combining the pixels from the different *EbsdMMap*'s. Figure 4.4 summarizes the operation of the distributed interface.

This implementation was successfully tested on the computing cluster of the Hydro-Québec Research Institute which consists of 1000 processors (AMD Opteron 2218 processor, 8 Gb of RAM per processor, Linux Centos 4.4 operating system, Sun Grid Engine nodes management system). The results presented in the following chapter on the applications of EBSD-Image were all calculated using this cluster.

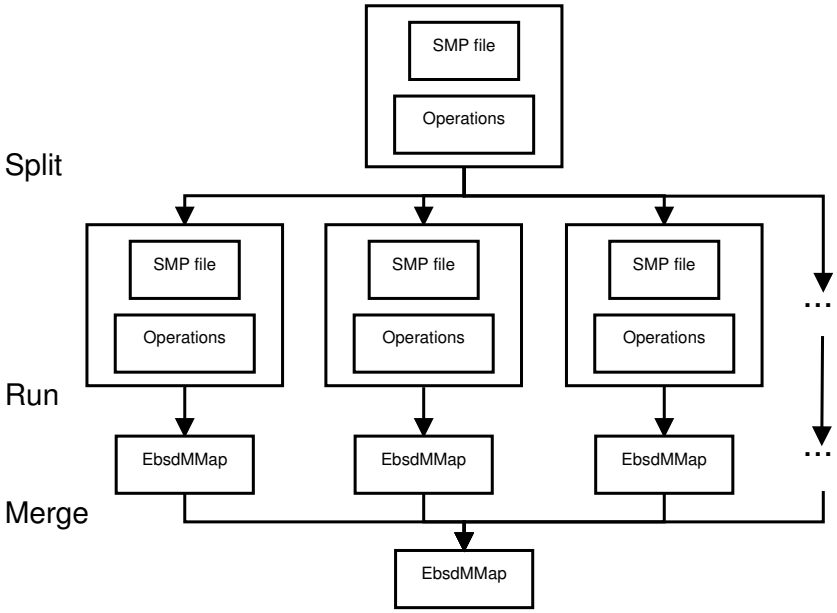

Figure 4.4: Operation diagram of the distributed interface.

4.5 Implementation

The following paragraphs detail how strategic and more complex algorithms are implemented in the analysis engine. The implementation of these algorithms is an important aspect of the analysis engine; users must understand them in order to decide which ones to use. Trivial algorithms are not presented in this section. Their complete description can be found in the online documentation of the software. Six algorithms will be discussed: the Hough transform, two peak detection algorithms, two operations to prevent the detection of false positive peaks and two peak identification methods. The present version of EBSD-Image contains a prototype implementation of the indexing algorithm described by Kriger Lassen. As it requires more testing and some fine tuning, it will not be presented in this work.

4.5.1 Hough Transform

As explained previously in section 2.2.2, the Hough transformation is used in EBSD to convert Kikuchi bands in the diffraction pattern into peaks in the Hough space. Practically, each pixel in the original grayscale diffraction pattern image is transformed into a sinusoidal function (Equation 2.2, $\rho = x\cos\theta + y\sin\theta$). The function carries a third dimension which is the intensity of its original pixel. The Hough space is the accumula-

tion of these functions and their intensities. To prevent biasing problems as reported by Krieger Lassen [3] and Tao [8], the intensity at each coordinate θ and ρ in Hough space is equal to the average (instead of the sum) of the intensity of all the sinusoidal functions passing by this coordinate. The intensity of a coordinate in Hough space is therefore the average intensity of the pixels along its corresponding line in image space.

In EBSD-Image, we defined the Hough space to be bound in θ between 0 (included) and π (excluded) and in ρ between $-R_{\max}$ and $R_{\max}$ (both included), where $R_{\max}$ is equal to half the diagonal of the original image. Although the Hough space is continuous and infinite in nature, these limits eliminates redundancy and empty space.

To perform further calculations on the Hough space, it must be quantized. The quantization converts the continuous space into a discrete representation, which can be visualized as an image. We refer to this representation as the *HoughMap*. The width of the map corresponds to the θ axis whereas the height is the ρ axis. By definition, the height always has an odd number of pixels so that the value of $\rho = 0$ corresponds to the line in the middle of the map. The quantization is first performed spatially by selecting a resolution for θ ($\Delta\theta$) and and one for ρ ($\Delta\rho$). For example, a $\Delta\theta$ resolution of $1\,^\circ/\text{px}$ will result in a image with a width of 180 px. The height will depend on the size of the original map and the selected $\Delta\rho$ resolution. The Hough space is further quantized in the third dimension to values between 0 and 255 (8-bit).

Although practical, the quantization leads to a loss of resolution and potentially distortion of the Hough space. For instance, depending on the $\Delta\rho$ and $\Delta\theta$ selected, the peaks may have a different shape. Lam et al.[47] define two types of peak distortion. A peak with a larger height than its width is the result of "spreading" whereas "extension" results in a peak with a larger width than height. Spreading comes from an over-quantization of ρ or under-sampling of θ. Extension is the complementary effect where θ is over-sampled or ρ is under-quantized. Choosing a resolution that produces "squared" peaks is important because algorithms designed to help the detection of Hough peaks assume this characteristic.

Such algorithm was introduced by Krieger Lassen [3] and is referred to as the butterfly mask. The peaks in Hough space have a characteristic shape: a bright center and four wings extending in the θ direction (Figure 4.5). This leaves two regions with lower values above and below the peak. A common pattern recognition method is to create a mask that matches the shape of the desired features and performs a convolution between this mask and the image. An example of such mask is given in Equation 4.1 [3]. The result is an image where the intensity of the desired features is increased with respect to the

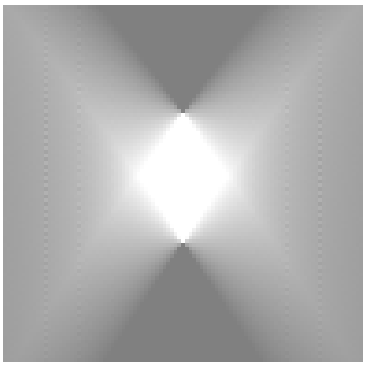

Figure 4.5: Characteristic shape of a Hough peak.

background and other undesired features of the image. The peak detection is simplified due to this increase of contrast. However, to obtain a good match, the mask must correspond to the shape of the peaks in Hough space. Thus, the choice of the Hough resolutions must take into consideration the shape of the mask, and vice-versa. Although the convolution mask can take any shape it is typically square, which as a result, imposes the constraint on the quantization of the Hough space to create square peaks.

$$\begin{bmatrix} -10 & -15 & -22 & -22 & -22 & -22 & -22 & -15 & -10 \\ -1 & -6 & -13 & -22 & -22 & -22 & -13 & -6 & -1 \\ 3 & 6 & 4 & -3 & -22 & -3 & 4 & 6 & 3 \\ 3 & 11 & 19 & 28 & 42 & 28 & 19 & 11 & 3 \\ 3 & 11 & 27 & 42 & 42 & 42 & 27 & 11 & 3 \\ 3 & 11 & 19 & 28 & 42 & 28 & 19 & 11 & 3 \\ 3 & 6 & 4 & -3 & -22 & -3 & 4 & 6 & 3 \\ -1 & -6 & -13 & -22 & -22 & -22 & -13 & -6 & -1 \\ -10 & -15 & -22 & -22 & -22 & -22 & -22 & -15 & -10 \end{bmatrix} \tag{4.1}$$

In addition to the Hough resolution, the aspect ratio of a peak is also dependent on the width of the Kikuchi band, the peak's position in Hough space and the dimensions of the diffraction pattern [3]. Equation 4.2 summarizes the relation between the aspect ratio ($\mathcal{AR}$), the resolutions ($\Delta\theta$ and $\Delta\rho$), the width of a Kikuchi band (b), the position of the peak (θ, ρ) in Hough space and the size of the diffraction pattern (width w and height h). This equation is derived from the definition of the aspect ratio: the ratio between the number of pixels in ρ and θ in the *HoughMap*.

$$\mathcal{AR} = f\left(b, \theta, \rho, w, h\right) \frac{\Delta\theta}{\Delta\rho} \tag{4.2}$$

Ideally, the aspect ratio of a peak should be close to unity for typical widths of Kikuchi bands, for a large portion of the Hough space and for diffraction patterns of any size. If the solution of function f is known, only one of the two resolutions is required to calculate the value of the other. We found it to be more intuitive to ask the user to specify the $\Delta\theta$ and internally calculate the $\Delta\rho$, as the execution time is proportional to $\Delta\theta$. The goal of this study is, therefore, to look at the effects of the different parameters on the aspect ratio of the peaks and find a simple relationship between $\Delta\theta$ and $\Delta\rho$.

To analyze the influence of the peak position in the Hough space on the aspect ratio, simulated diffraction patterns containing only one Kikuchi band were used. The slope and position of the Kikuchi band in the diffraction pattern were selected to cover the whole Hough space. The patterns were created by drawing a white line of a certain width on a gray background (intensity of 128). Then the Hough transform was performed using different resolutions. Finally, the single peak in the *HoughMap* was thresholded and its dimensions were used to calculate the aspect ratio. To visualize the variation in aspect ratio, values were color-coded and plotted as a function of θ and ρ.

Figure 4.6 illustrates the final result for a diffraction pattern of 672 by 512 px and a Kikuchi band with a width of 40 px. $\Delta\theta$ and $\Delta\rho$ were equal to $0.1\,^\circ$/px and 1 px/px, respectively. The aspect ratio varies as a function of θ and ρ having maximum values near 45 and 135°. This variation can be explained by the different possible band length in the diffraction pattern. Oblique bands crossing the center of the diffraction pattern are longer than horizontal or vertical bands crossing the center or those near the edges. Figure 4.7 shows how the length of a band influences the variation in θ. Longer bands produce peak spreading which increases the aspect ratio. This is a problem since the region of the Hough space with an aspect ratio close to 1 is small and non-uniform, regardless of the relation between $\Delta\theta$ and $\Delta\rho$

For rectangular EBSD cameras, it is a common practice to select a circular region of interest to eliminate background noise coming from the edges of the camera. This is, of course, not needed for circular cameras. Our simulations of the aspect ratio on such diffraction patterns also show that the circular mask eliminates the variation of the aspect ratio as a function of θ. Figure 4.8 illustrates results for the same parameters as Figure 4.6, after a circular mask with a diameter equal to the height of the pattern was applied before performing the Hough transform.

The variation in the θ direction is removed since the circular mask fixes a maximum length for the bands (*i.e.* the diameter of the mask) regardless of their orientation in the diffraction pattern. However, peak spreading still occurs for bands located further

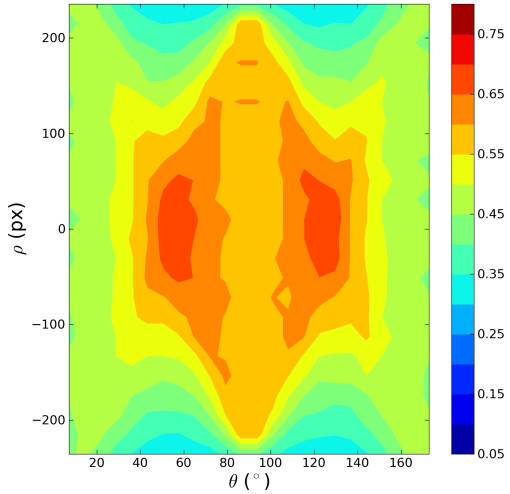

Figure 4.6: Variation of the aspect ratio of the peaks in Hough space for a diffraction pattern of 672 by 512 px, a Kikuchi band with a width of 40 px, $\Delta\theta = 0.1\,^\circ/\text{px}$ and $\Delta\rho = 1\,\text{px/px}$.

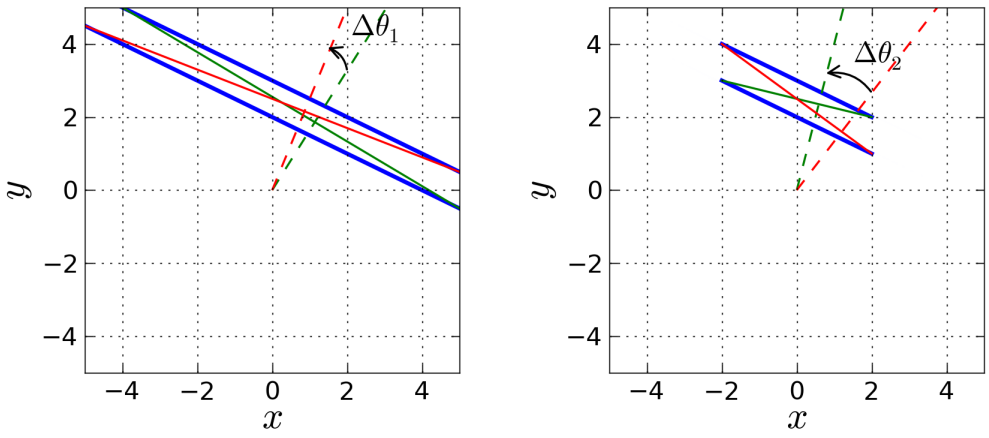

Figure 4.7: Schematic demonstrating the influence of the length of a band on the width of a Hough peak ($\Delta\theta$). In both figures, the band is drawn with two solid blue lines. The red and green lines are the furthest away from the central line of the band while being fully inscribed inside the band. The dashed lines represent the lines perpendicular to the red and green line. The shorter is the band, the greater is the width of the Hough peak.

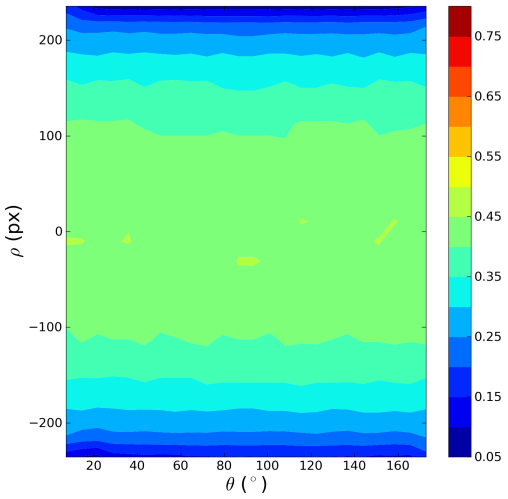

Figure 4.8: Variation of the aspect ratio of the peaks in Hough space for a diffraction pattern of 672 by 512 px, a Kikuchi band with a width of 40 px, $\Delta\theta = 0.1\,^{\circ}/\text{px}$, $\Delta\rho = 1\,\text{px/px}$ and a circular mask with a diameter of 512 px.

away from the center of the image. Nevertheless, the circular mask has the benefit of extending the region of constant aspect ratio. Also, from the point of view of accurate band detection, this variation is potentially useful since small bands located far away from the center are not as relevant as longer bands passing through the center. These small bands are also often noisier and could lead to the detection of false peak. The use of a butterfly filter will therefore not enhance these peaks to the same degree as those close to the center. It is therefore important, for accurate peak detection, to apply a circular mask on rectangular diffraction patterns.

In his Ph.D. thesis, Krieger Lassen [3] derives two equations to express the height and width of the peaks in the Hough space for circular diffraction patterns. With these relationships, the function $f(b, \theta, \rho, w, h)$ of Equation 4.2 can be re-written as

$$f(b, \theta, \rho, w, h) \Rightarrow f(b, \rho, R) = \frac{b}{2\arctan\left(\frac{b}{2\sqrt{R^2-\rho^2}}\right)} \tag{4.3}$$

where b is the band width, ρ is the ρ coordinate of the peak and R is the radius of the circular mask. This relationship closely matches the results obtained by the simulated diffraction patterns. Figure 4.9 compares the variation of the aspect ratio distribution as a function of ρ for the same circular mask radius and band width.

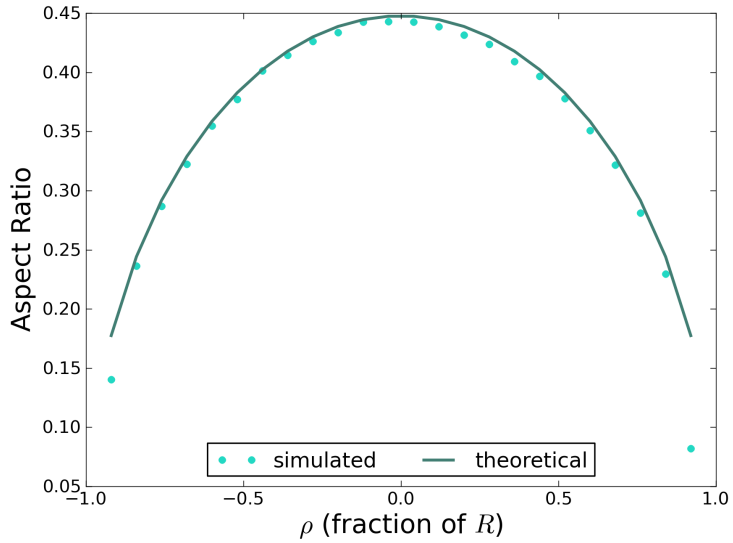

Figure 4.9: Comparison of the aspect ratio variation with theρ coordinate for the simulated measurements and the theoretical relationship given by Equation 4.3.

Using the theoretical relationship, the influence of the three remaining parameters (radius of the circular mask, ρ coordinate and band width) can be more easily studied. An important characteristic of how diffraction patterns are acquired is that, for a given set of experimental conditions (accelerating voltage, type of sample, position of the camera), the ratio between the size of the diffraction pattern and the average width of its Kikuchi bands is constant. This is explained by the acquisition process where the size of the diffraction pattern is dependent on the selected binning. Therefore, a band with a width of 40 px in a diffraction pattern without binning would have a width of 10 px if the size of the diffraction pattern is reduced by a factor of 4. It is therefore possible to express the band width as a function of the diffraction pattern size or, equivalently, of the radius of the circular mask (assuming the later has a diameter equal to the height of the diffraction pattern). It is also important to mention that detectable Kikuchi bands (bands with an intensity above the background) have a width much smaller than the radius. For normal experimental conditions, their width is typically less than one eighth of the height of the diffraction pattern and more than a few pixels. The ρ coordinate can vary between $-R$ and R. However, as mentioned previously, its useful range is smaller since small bands located at the periphery of the circular mask have a smaller weight in the peak detection.

Since the band width and ρ coordinate depend on the circular mask radius, it can

be shown that $f(b, \rho, R)$ is linearly dependent on the radius. The proof is detailed in Equation 4.4. This implies that previous results from Figures 4.6, and 4.8 are valid for any size of diffraction pattern. From now on we will, therefore, refer to the units of the band width and the ρ coordinate as a fraction of R instead of a number of pixels.

$$\begin{aligned} f(b, \rho, R) &= \frac{k_1 R}{2 \arctan\left(\frac{k_1 R}{2\sqrt{R^2-(k_2 R)^2}}\right)} \\ &= \frac{k_1 R}{2 \arctan\left(\frac{k_1 R}{2R\sqrt{1-k_2}}\right)} \\ &= \frac{k_1 R}{2 \arctan\left(\frac{k_1}{2\sqrt{1-k_2}}\right)} \\ &= \frac{k_1 R}{k_3}, k_3 = 2 \arctan\left(\frac{k_1}{2\sqrt{1-k_2}}\right) \\ &\propto R \end{aligned} \tag{4.4}$$

Using Equation 4.3, Figure 4.10 illustrates the variation of $f(b, \rho, R)$ as a function of the band width and the ρ coordinate. The band width was varied between one hundredth and one quarter of the circular mask radius. The ρ coordinates cover the range from $-R$ to R.

This distribution shows that $f(b, \rho, R)$ is more dependent on the ρ coordinate than on the band width. Figure 4.11 focuses on the variation of the band width for given ρ's. The effect of the band width only becomes important for high ρ values. For a ρ less than 80% of the circular mask radius, the band width variation is less than 1.5%. We can conclude that the main factor in Equation 4.3 is the ρ coordinate of the peak in the Hough space or, equivalently, the distance of a Kikuchi band from the center of the diffraction pattern.

Going back to our initial problem of finding a function relating the $\Delta\theta$ and $\Delta\rho$, one simple solution of Equation 4.3 is to find an average value for the band width and the ρ coordinate. A better approximation is to find an average value of the aspect ratio over a range of band widths and ρ coordinates. This translates mathematically by solving the following integral:

$$\langle f(b, \rho, R) \rangle = \int_{b_0}^{b_1} \int_{\rho_0}^{\rho_1} \frac{b}{2 \arctan\left(\frac{b}{2\sqrt{R^2-\rho^2}}\right)} \, \mathrm{d}b \, \mathrm{d}\rho \tag{4.5}$$

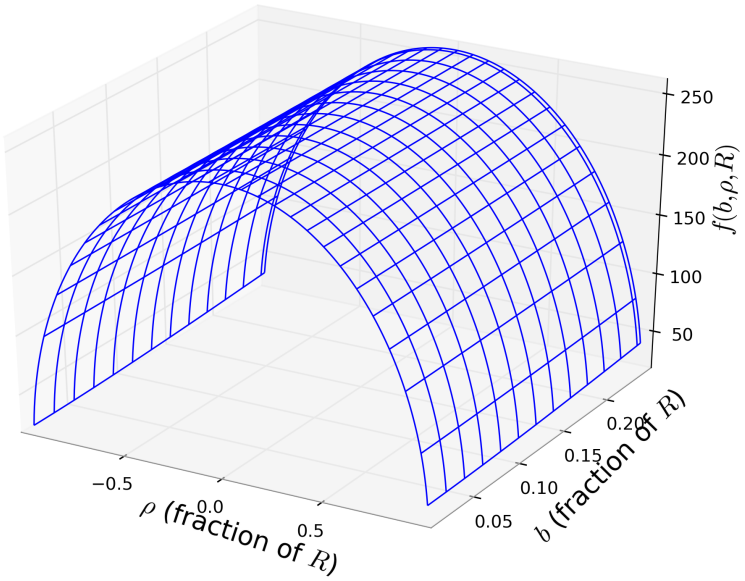

Figure 4.10: Aspect ratio variation with the band width and the ρ coordinate in accordance with Equation 4.3.

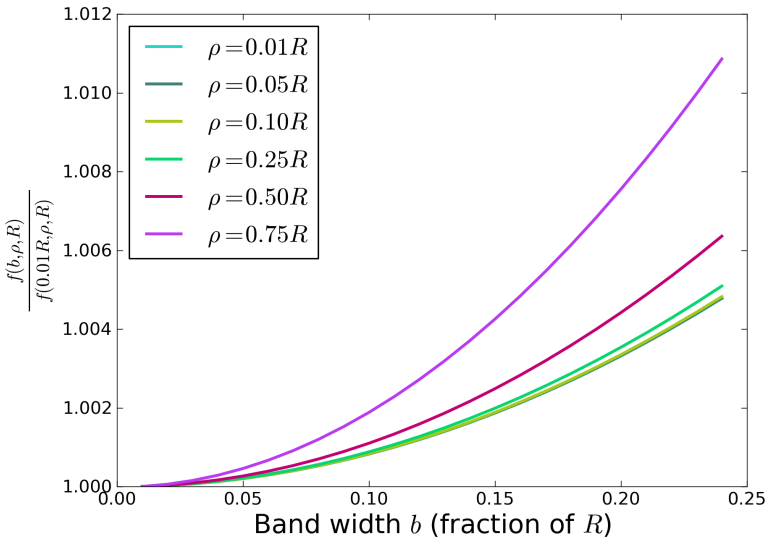

Figure 4.11: Aspect ratio variation with the band width for different ρ coordinates in accordance with Equation 4.3.

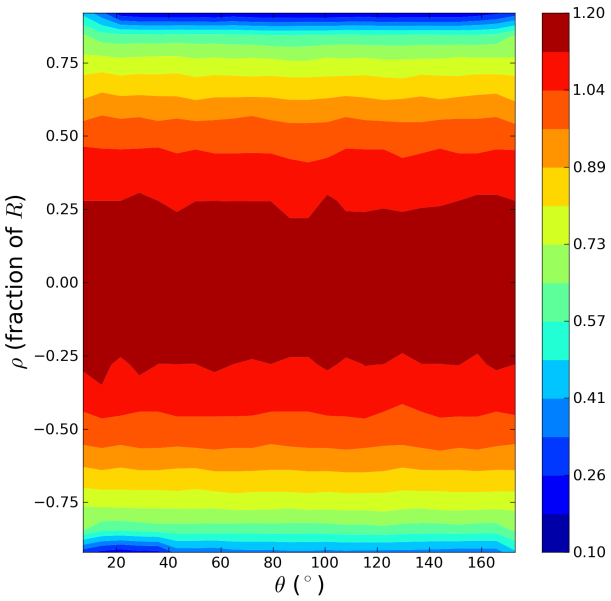

Figure 4.12: Variation of the aspect ratio of the peaks in Hough space for a diffraction pattern of 672 by 512 px, a Kikuchi band with a width of 40 px, $\Delta\theta = 0.1\,^\circ/\text{px}$, $\Delta\rho$ calculated using Equation 4.6 and a circular mask with a diameter of 512 px.

By combining the latter with Equation 4.2, the relation linking $\Delta\rho$ to $\Delta\theta$ can be established as:

$$\Delta\rho = \left[\int_{b_0}^{b_1} \int_{\rho_0}^{\rho_1} \frac{b}{2\arctan\left(\frac{b}{2\sqrt{R^2-\rho^2}}\right)} \,\mathrm{d}b\,\mathrm{d}\rho \right] \Delta\theta \tag{4.6}$$

It is not possible to solve the integral analytically, therefore a numerical method is required. The Java implementation from Robert Dodier [48] of the numerical integration library QUADPACK [49] developed by Piessens et al. is used to solve the integral. The boundary conditions can be modified by the user to match their experimental conditions. However the following default values are provided as a first estimation: $b \in [0.01R, 0.25R]$ and $\rho \in [-0.9R, 0.9R]$. Similar to Figures 4.6 and 4.8, the variation of the aspect ratio in the Hough space with these default values is shown in Figure 4.12.

4.5.2 Peak Detection

The obvious step after performing the Hough transform is to detect peaks to find the position of the Kikuchi bands in the diffraction pattern. The process of selecting features from an image is called thresholding. It separates the desired features from the rest of the image. In the current revision of the analysis engine, two peak detection algorithms were implemented.

The first is an adaptation of the top hat algorithm presented by Gonzalez and Woods [14]. This algorithm consists of three steps. First, a duplicate of the original image (Figure 4.13) is made. Then all the important features of an image are removed by applying a series of opening operations on the image (Figure 4.14) until only the background remains in the image. Finally, by subtracting the duplicate of the original image from the latter (containing only the background), the white areas, in occurrence the peaks, are amplified with respect to the background (Figure 4.15). It is therefore easier to threshold the peaks using an automatic thresholding algorithm. Our analysis revealed that the average between the min error [50] and the Kapur [51] thresholding value gives a reliable peak detection for most diffraction patterns. False peaks are sometimes detected, but can be removed later using peak cleaning operations such as the peak shape, which will be discussed later.

The second peak detection algorithm uses the statistical distribution of the Hough space to select peaks out of the background. It makes the assumption that the peaks have a significantly higher intensity than the average intensity of the Hough space. By "sig-

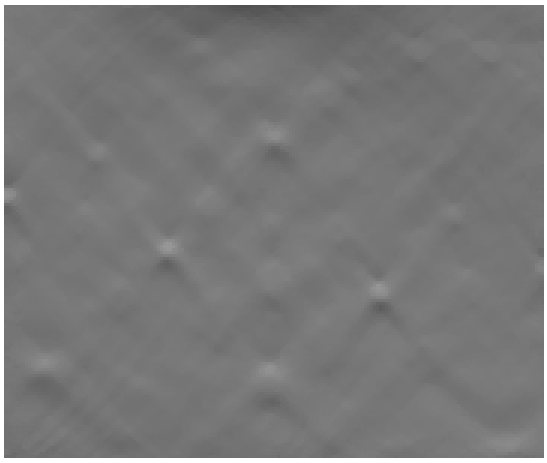

Figure 4.13: Original *HoughMap* to illustrate the top hat and standard deviation peak detection algorithm.

Figure 4.14: *HoughMap* after five openings. All the features of the original *HoughMap* are removed.

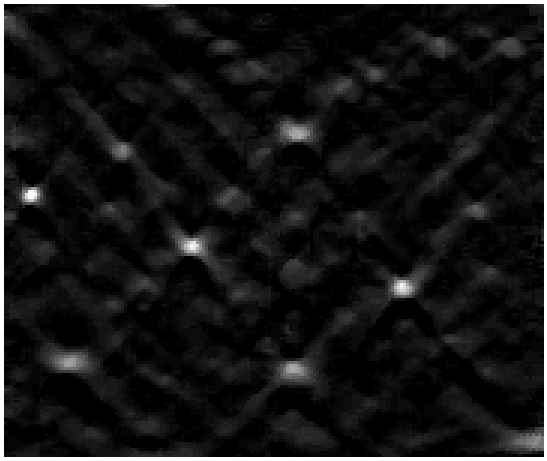

Figure 4.15: Result of the top hat peak detection algorithm applied on the original *HoughMap*. The contrast of the peaks is increased.

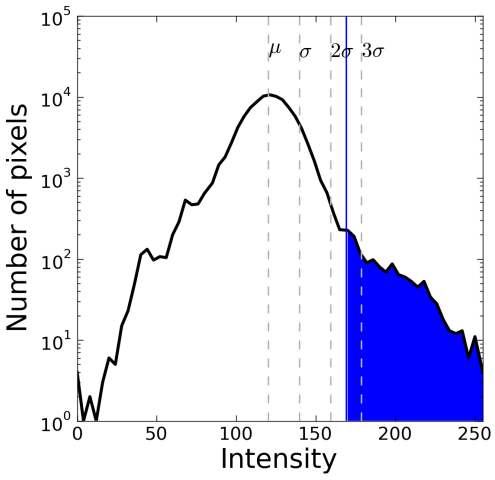

Figure 4.16: Intensity distribution of the original *HoughMap*.

Figure 4.17: Result of the standard deviation peak detection algorithm applied on the original *HoughMap*.

nificantly higher", we imply that the intensity is greater than the average μ by a multiple of the standard deviation σ of the Hough space. It is up to the user to decide this level of confidence. Figure 4.16 illustrates graphically how the peaks are selected by showing the intensity distribution (histogram) of a *HoughMap* (Figure 4.13). In this particular example, the level of confidence was selected to be 2.5 times the standard deviation. The resultant binary map showing the thresholded peaks is shown in Figure 4.17.

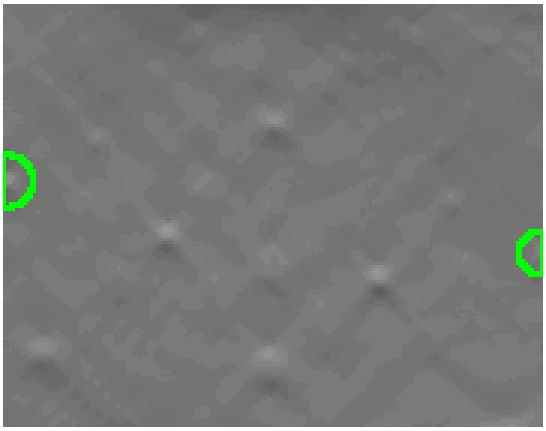

Figure 4.18: *HoughMap* before expansion in θ. A peak is split in two.

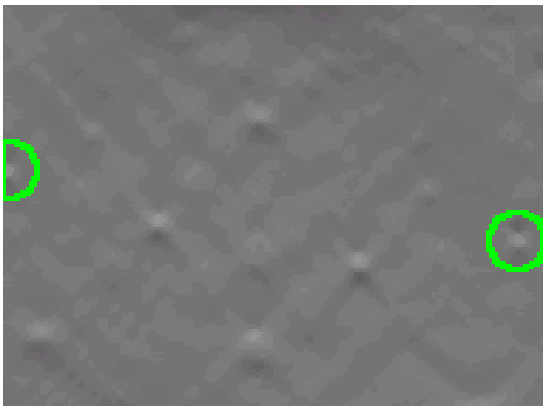

Figure 4.19: Expansion of the *HoughMap* in θ. The split peak is reconstructed.

4.5.3 Peak Clean-Up

Apart from the quantization previously discussed, the representation of the continuous Hough space in an image leads to another type of artifact: double peaks. For example, a perfectly vertical Kikuchi band in a diffraction pattern located near the left side of the pattern has two solutions after the Hough transformation: one near 0° with a negative ρ or another near 180° with a positive ρ. In reality the Hough space is circular in θ, but when represented in an image it is bounded between 0 and 180°. These two positions are therefore equivalent. If this effect is not taken into consideration, two Kikuchi bands will be detected instead of one. There is also the possibility that the detection algorithm will fail to detect any peak since they are incomplete. To prevent this problem for vertical Kikuchi bands, two operations must be performed in tandem. First, the *HoughMap* (Figure 4.18) is expanded in θ pass 180° by a certain amount, typically 5 to 10°. One half of the split peaks near 180° is now complete and can be properly detected on its own (Figure 4.19). Then, after identifying the position of all peaks in the *HoughMap*, peaks found in the expanded region of the *HoughMap* are brought back inside the original θ range (0 to 180°). If two peaks are located at the approximately same position, only one is retained and used in subsequent operations.

Another clean-up operation available in EBSD-Image is related to the expected shape of the peaks in the *HoughMap*. As discussed previously, special considerations were taken to assure that most of the peaks in the Hough space are square. Although the purpose is mainly related to the proper function of the convolution mask, this characteristic of the peaks can also be used to remove wrongly detected peaks – peaks with an aspect

ratio much larger than unity can be eliminated. In short, this operation takes advantage of the proper selection of the Hough transform resolutions and offers the possibility to clean the detected peaks based on their shape.

4.5.4 Peak Identification

To perform indexing and the calculation of certain quality metrics, the position and the intensity of the peaks must be accurately measured. Many different methods can fulfill this task. Two are currently implemented in EBSD-Image: the local centroid and the center of mass. From the binary image of the detected peaks, the first method finds the centroid of each peak and takes this value as the position of the peak. The intensity is either measured as the maximum pixel intensity inside the detected peak or simply the intensity of the closest pixel to the centroid. The second method was proposed by Krieger Lassen [52]. It consists of the weighted average of the pixels inside a peak divided by the average intensity of the peak as given by Equation 4.7.

$$\langle(\theta,\rho)\rangle = \left(\frac{\sum_{i}^{N} \theta_i I_i}{\sum_{i}^{N} I_i}, \frac{\sum_{i}^{N} \rho_i I_i}{\sum_{i}^{N} I_i} \right) \tag{4.7}$$

The sums are performed on all the pixels inside each detected peak. The intensity of the closest pixel to the center of mass is taken as the peak intensity.

Chapter 5

Applications

Possible applications of the EBSD technique in the fields of materials engineering and geology are endless. Phase identification, grain mappings, strain measurements, and texture analysis are just a few examples. To illustrate potential applications of the simulation and analysis engine developed in this work, this chapter discusses two projects where the EBSD-Image software was successfully used: (i) the identification of the α-Zr and β'-Zr phase in Zr-2.5Nb pressure tubes, and (ii) the quantitative measurement of the deformation induced during metallographic specimen preparation These applications are selected to emphasize the advantages of this new EBSD software over its commonly used commercial counterparts. The explanations, results and discussions given in the following paragraphs therefore aim to showcase the features of EBSD-Image, rather than presenting a in-depth description of the projects.

5.1 Zr-2.5Nb Pressure Tubes

5.1.1 Background

The pressure tubes are at the heart of the CANDU-6 reactor [53]. They are responsible for the transport of heavy water inside the reactor which extracts the energy from the nuclear reaction. Their deformation, primarily creep, governs the power output and ultimately the life of the reactor [54]. The material used for this purpose is a Zr alloy containing 2.5 wt% Nb. The microstructure is composed of primary α-Zr regions ($\approx$ 80 %) separated by secondary phases (β-Zr and metastable phases), which we shall refer to as β'-Zr. Pressure tubes are manufactured via extrusion resulting in an elongated and strongly textured microstructure of the α-Zr regions [55]. Figure 5.1 shows a typical

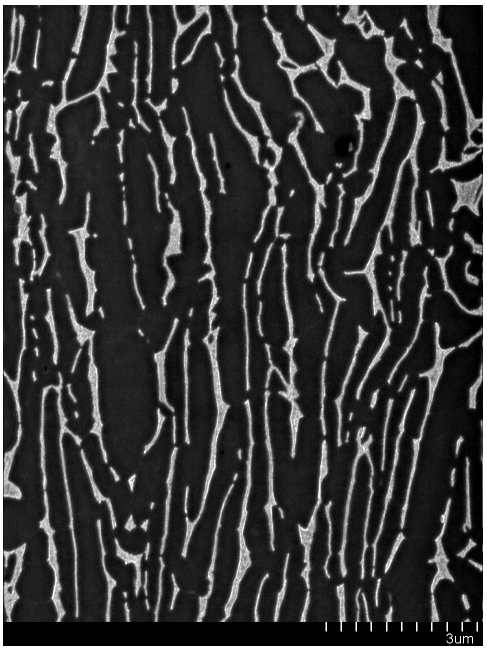

Figure 5.1: Typical microstructure of Zr-2.5Nb pressure tube. α-Zr phase appears in black and β'-Zr in white. The contrast between the two phases is obtained by a reactive ion etching ($CH_4^+O_2$) of the sample.

microstructure in the radial-tangential plane of the tube obtained by reactive ion etching.

The average dimensions of the α-Zr domains are approximately 500 nm by 1500 nm whereas the β'-Zr domains are less than 50 nm wide. Using EBSD, the β'-Zr regions were only partially identified ($< 2\,\%$). The low quality of the diffraction patterns obtained can explain the small index rate of this phase. Possible factors for the decrease in diffraction quality could be: the size of the phase (resolution limit), the sample preparation favoring the diffraction of α-Zr, the presence of metastable phases and a higher dislocation density. To perform accurate grain analysis of the α-Zr phase, pixel cleaning and dilation are needed to obtain the correct size of the α-Zr grains [56]. However, these procedures must be done carefully so as not to artificially increase the size of the α-Zr grains. In other words, a boundary between the α-Zr and β'-Zr regions must be drawn to allow non-indexed pixels on either side to be filled.

5.1.2 Method

The chemical composition and sample preparation of the pressure tubes are detailed in Hovington et al. [57]. The diffraction patterns were acquired using a Hitachi S-4700 cold field-emitter equipped with Nordlys II camera and the HKL Channel 5 software. An

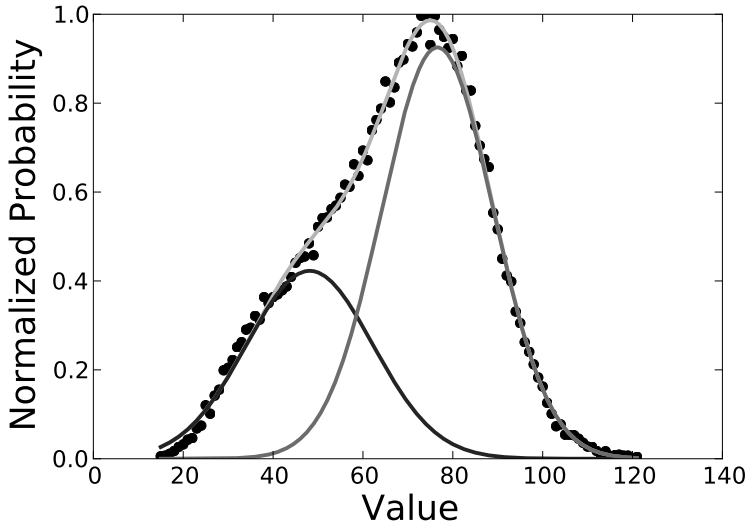

Figure 5.2: Band contrast distribution of an EBSD mapping.

accelerating voltage of 15 keV, binning of 8x8 with a 20 ms dwell time and a step of 30 nm were used for the mappings. Diffraction patterns were saved without any compression.

5.1.3 Results

Hovington et al. [57] used the band contrast quality metric to discriminate between the two phases. The band contrast distribution (Figure 5.2) shows the superposition of two Gaussian distributions. The pixels with a value below the intersection of the two curves were thresholded to select regions with a low quality diffracting index. These regions were then assigned to the β'-Zr phase in accordance with the hypothesis that β'-Zr regions were not properly identified due to the lower quality of their diffraction patterns. It was, however, understood that since the two Gaussian distributions overlapped each other, the thresholding also selected pixels corresponding to the α-Zr phase.

The same analysis was performed using EBSD-Image. Other quality metrics such as the average, standard deviation, entropy, image quality, peaks count, *etc.*were calculated to identify distributions where the two Gaussian peaks would be less convoluted. The same diffraction patterns were fed to the analysis engine of EBSD-Image and the histograms of each resultant map were plotted. The different quality metrics provided a different look at the results. Figure 5.3 to 5.8 give examples of some of the results. Certain metrics exhibit similar features as the band contrast (*e.g.* Hough Range), whereas

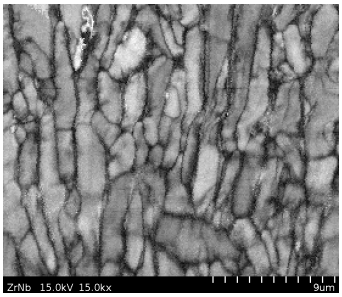

Figure 5.3: Band contrast.

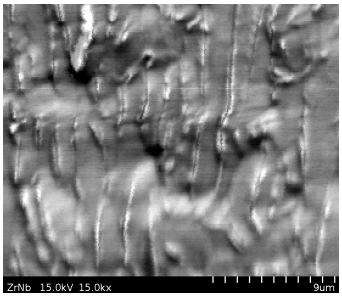

Figure 5.4: Average.

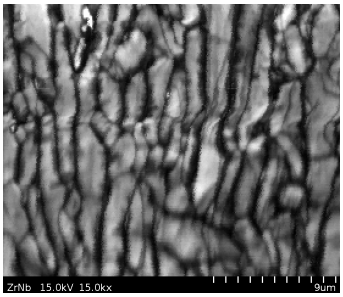

Figure 5.5: Standard deviation.

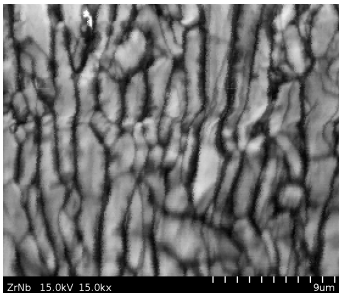

Figure 5.6: Entropy.

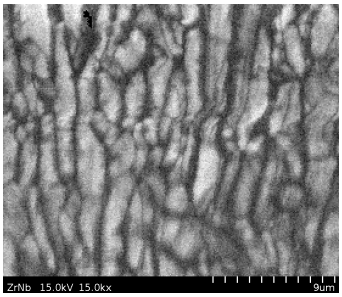

Figure 5.7: Fourier.

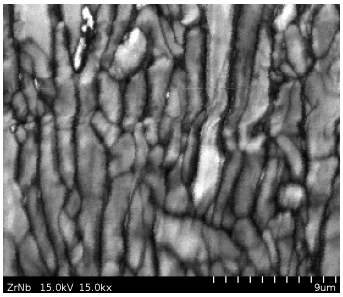

Figure 5.8: Hough range.

others could not be used for discriminating the two phases (*e.g.* Average). In other words, the undiscriminating metrics could not resolved the two Gaussian distributions in the histogram better than for the band contrast. However, the entropy was found to give a slightly better result than the band contrast (Figure 5.9) because the two peaks are more distant, although there is still some subjectivity regarding the choice of the threshold level.

As before, the latter was chosen to be the intersection of the two Gaussian distributions. Figure 5.10 and 5.11 shows the results of the thresholding. The regions identified are more continuous using entropy than with band contrast.

5.1.4 Discussion

EBSD-Image also offers the possibility of using boolean image analysis routines to visually evaluate results. In this instance, the location of the pixels common and differing between the two thresholding methods can be visualized by performing a series of AND and inversion operations on the two binary maps. In Figure 5.12, the regions in green are common pixels between the entropy and band contrast methods, whereas the blue pixels are unique to entropy and the red pixels to band contrast. The entropy thresholded

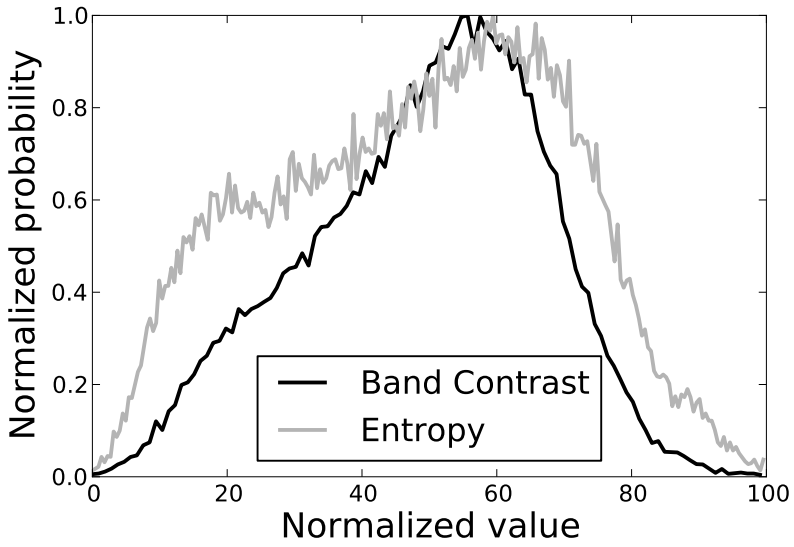

Figure 5.9: Comparison between the band contrast and entropy distribution.

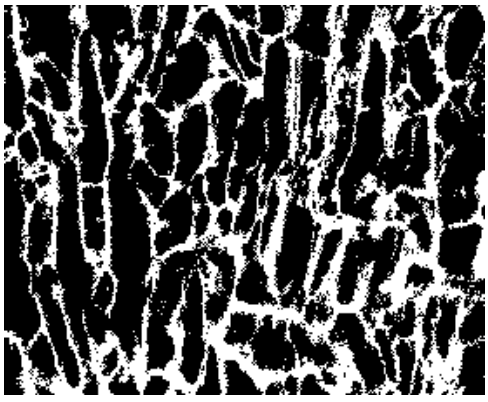

Figure 5.10: Binary map resulting from the thresholding of the β'-Zr phase from the band contrast quality metric.

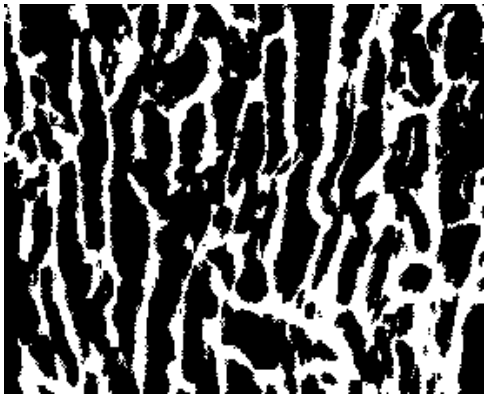

Figure 5.11: Binary map resulting from the thresholding of the β'-Zr phase from the entropy quality metric.

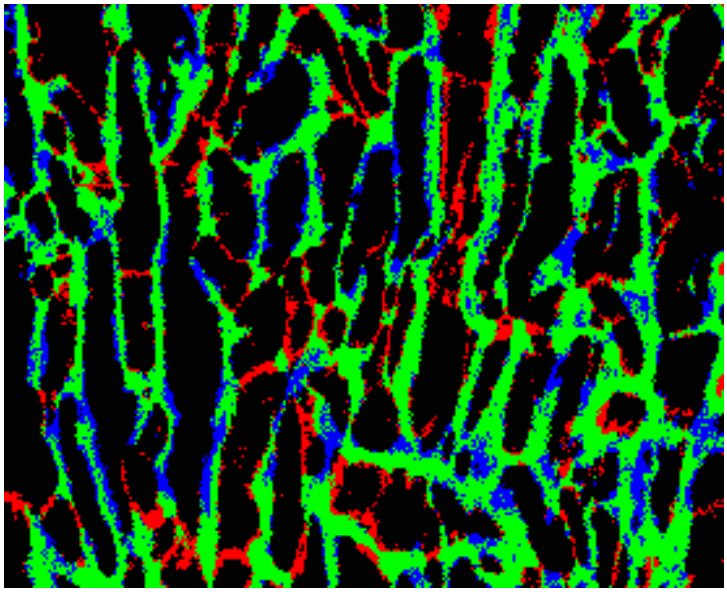

Figure 5.12: Difference between the band contrast and entropy thresholding (green: common pixels, blue: only in entropy, red: only in band contrast).

map contains more pixels of the β'-Zr phase (blue), although band contrast also finds β'-Zr regions (red) where entropy does not. Further investigation of the orientation map indicates that most of these pixels (red) correspond to α-Zr grain boundaries rather than the β'-Zr phase. These pixels are therefore incorrectly associated to the β'-Zr phase when band contrast is used.

This observation can be further validated by verifying the number of pixels that correspond to both the thresholded map and the α-Zr phase. Ideally, no pixels in the α-Zr phase should be present in the thresholded map. This comparison is obtained by first selecting the α-Zr phase from the *PhasesMap*, performing an AND operation with the thresholded map and finally counting the number of pixels with a value of 1. The results are 978 pixels using the band contrast metric and 679 pixels using the entropy metric, corresponding respectively to 2.5 % and 2.1 % of the total surface fraction of the α-Zr phase. This confirms that entropy is better at discriminating between the α-Zr and β'-Zr phase than band contrast.

5.1.5 Conclusion

The improvement on discrimination accuracy shows one advantage of calculating more quality metrics to further evaluate an EBSD mapping. In the case of Zr-2.5Nb pressure tubes, the use of the entropy quality metric allows for a more accurate analysis of the α-

Zr grains and relates the changes in microstructure to the creep behavior of the pressure tubes.

5.2 Quantitative Measurement of the Deformation During Metallographic Specimen Preparation

5.2.1 Background

The golden rule of metallographic specimen preparation is to always remove the surface damage induced by each step of the preparation in the following one [58]. The quantification of the extent of damage is useful information to establish proper specimen preparation methods, especially for samples analyzed with EBSD, as this technique is surface sensitive. Such measurements have been performed by Samuels [59] using light optical microscopy (LOM) observations of chemically etched samples. He also used transmission electron microscopy (TEM) to observe highly deformed regions using a higher resolution. With its submicron resolution, EBSD can quantitatively analyze deformation at a smaller length scale than LOM while providing higher statistics than TEM. The objective of this work is twofold: determination of the amount of deformation induced during two sectioning and two grinding preparation steps, and the evaluation of the ability of several quality metrics to detect deformation from diffraction patterns.

The deformation occurring during either sectioning, grinding or polishing is created by high compression loadings at a low temperature (close to room temperature). The material removal comes from the action of a "tool" (*i.e.* blade, abrasive particles, *etc.*) on the surface of a specimen [60]. The tool indents the surface due to its higher hardness. The relative motion of the tool and the specimen (typically rotational movement) shears chips of material from the surface. This action leaves behind a deformation zone below the indentation depth. The depth of this deformation zone depends on the type of tool used and the nature of the material.

With his measurements, Samuels identified two distinct regions in the deformation zone: the shear band layer (SBL) and the deformed layer (DL) (Figure 5.13). The shear band layer is located below the damaged surface: it is the most deformed region with an estimated strain level of up to $\epsilon = 7$ near the surface down to $\epsilon = 2.5$ near the beginning of the deformed layer. This high level of deformation is caused by the shearing action of the tool. For pure metals, relaxation and partial recrystallization are responsible for the presence of small equiaxed grains ($\approx 30\,\text{nm}$) near the surface. The shear band

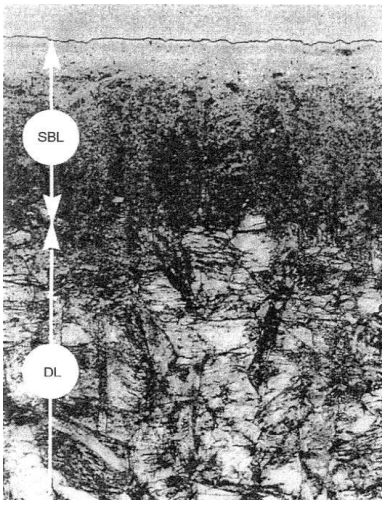

Figure 5.13: LOM micrograph of the shear band layer (SBL) and the deformed layer (DL) for a 30% Zn brass sample deformed by a planning tool [59].

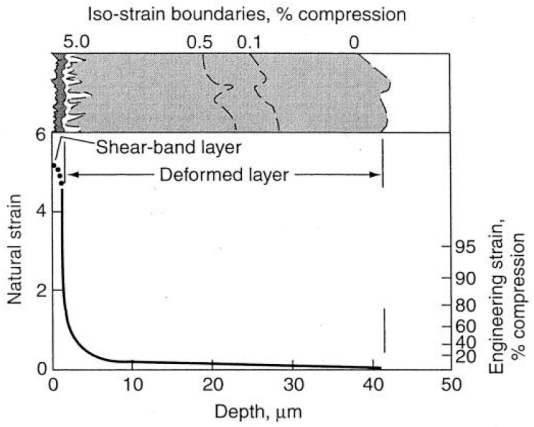

Figure 5.14: Schematic of the strain level in the shear band layer (SBL) and deformed layer (DL) [59].

layer is primarily dependent on the material: hardness, recrystallization temperature, slip systems, *etc*. Its depth is the most important parameter from the point of view of a metallographic preparation procedure as it is this deformation that must be removed between the different steps [59].

The deformed layer extends for 5 to 10 times the depth of the shear band layer up to the elastic-plastic deformation boundary. However, the strain level is much smaller as the deformation is induced by the compression of the tool on the material. Figure 5.14 schematically illustrates the decrease of the strain level and delimitation of the two layers.

As discussed in section 2.3, quality metrics calculated from diffraction patterns can be used to evaluate the level of deformation. Distortion in the lattice by the accumulation of dislocations diffuses the edges of the Kikuchi bands thus creating a lower quality diffraction pattern [22, 23]. With the high level of strain (especially in the shear band layer), the quality of the diffraction patterns is often too low for precise localization of the Kikuchi bands which leads to incorrect or impossible indexing. Misorientation kernels [61] and metrics [62, 63] developed to visualize strain fields are based on the local variation of crystal orientation. As accurate indexing is required, these methods are therefore difficult to use in this particular application.

The analysis engine of EBSD-Image provides a useful platform to calculate different quality metrics from the same set of diffraction patterns. Using the image analysis

routines in the software, a detailed analysis of the results can be achieved to identify deformed regions. These results will also allow us to determine which quality metrics are able to evaluate the level of deformation in a material.

5.2.2 Method

5.2.2.1 Specimen Preparation

This study evaluates the deformation behavior of two pure metals: copper and iron. As specified by the supplier, their purity is at least 99.99%. Each sample was deformed using four different methods: (i) a manual hack saw (ii) an abrasive cutting wheel designed for metallographic preparation (iii) a SiC 80 grit grinding paper (iv) a SiC 220 grit grinding paper. To observe the deformation induced by these different methods, the samples must be carefully prepared. It is important to prevent any further deformation of the sample during the subsequent preparation for EBSD analysis. We shall elaborate more on the preparation of these samples. Apart from the polishing method, the same steps were used for the copper and iron samples. The following explanations therefore apply to both metals.

From the stock block, five samples of each metal were cut out using the proper abrasive cutting wheel, and sectioned as small prisms. Having right angles between the faces of the sample will be important for the later steps. Three samples out of five were mounted in Bakelite and polished up to 0.05 μm colloidal silica to remove any deformation induced during sectioning. Two of these samples were then ground for one minute and half on either the 80 grit or 220 grit grinding paper. A force of 20 N was used with a polishing disk rotation speed of 300 rpm in the complementary direction with respect to the polishing head. The third sample serves as a control sample to verify that no deformation is introduced by the specimen preparation. The samples were then unmounted from the Bakelite. The remaining two samples were deformed using a manual hack saw and a programmable saw using abrasive cutting wheel, respectively. Polishing these samples up to colloidal silica is not necessary since the induced deformation is greater or equal to the deformation created during sectioning.

To protect the deformed surface from subsequent operations of the preparation, all five samples were nickel plated. A solution composed of 150 g of $NiSO_4 \cdot 6\,H_2O$, 1800 μL of a 0.01 M H_2SO_4 and 500 mL of H_2O, a voltage of 3 V and a current of approximately 20 mA were used. To create a 3 to 5 μm thick layer, the plating time is in the order of one hour.

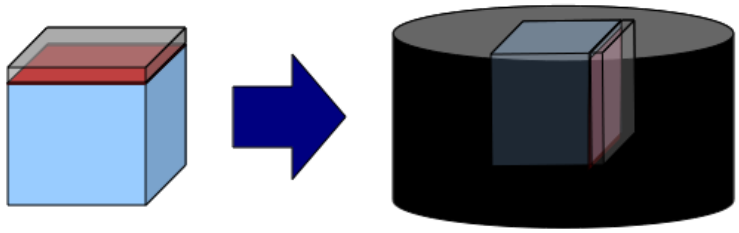

Figure 5.15: Arrangement of a deformed sample inside the Bakelite mount.

Surface	Abrasive	Speed (rpm)	Load (N)	Time (min)
SiC	320 grit	150[1]	20	Until plane
MD-Largo[3]	9 μm	150[2]	20	5
MD-Dur[3]	3 μm	150[2]	20	4
MD-Dur[3]	1 μm	150[2]	20	3
MD-Chem[3]	Mastermet[4]	150[2]	20	3

[1] Complementary rotation
[2] Contrary rotation
[3] Consumable trademark from Struers Inc.
[4] Consumable trademark from Buehler Inc.

Table 5.1: Sample preparation method for copper [64].

The samples were then mounted sideways in Bakelite. In other words, the deformed surface is perpendicular to the polishing surface of the mount. Figure 5.15 illustrates the positioning of a sample inside the Bakelite mount. The deformed surface is shown in red. The samples were polished up to colloidal silica following the procedures established especially for EBSD sample preparation by George Vander Voort [64]. These procedures require no chemical attack or electro-polishing and produce high quality diffraction patterns. Table 5.1 summarizes the mechanical polishing procedure for copper. The same procedure is used for iron except that a polishing step with MasterPrep for 3 min was added before the final step. All the steps were performed on automated polishing equipment to eliminate any human intervention. Finally, the samples were unmounted from the Bakelite and cleaned prior to observation inside the SEM.

5.2.2.2 Acquisition Parameters

In total, between the five copper and five iron samples, one hundred maps (260 Gb of data) were acquired on two EBSD systems: (i) a Hitachi S-4700 (cold field emitter) equipped

with a NordlysS (sensitive) camera and the HKL Channel 5 software package (ii) a Hitachi SU-70 (Schottky field emitter) equipped with a NordlysF+ (fast) camera and the HKL Channel 5 software package. This large data set is essential to obtaining a statistically representative sampling of the deformation layer of each sample. Despite the differences between the two systems, the resolution of the diffraction patterns is roughly the same (168 px by 128 px for the sensitive camera and 160 px by 120 px for the fast camera). All the diffraction patterns were stored on the hard drive without any compression. Inside the microscope, the samples were aligned to position the deformed surface perpendicular to the tilt axis. This ensured the best resolution along the deformation profile.

5.2.2.3 Stitching

For each sample, EBSD mappings were acquired to cover a continuous area along the deformation surface. Typically, the area covered is composed of one or two mappings along the deformation profile and several mappings in the direction parallel to the deformation surface. The mappings along the deformation profile are set-up to ensure that the deformation layer is fully included in the mappings as well as a region of the undeformed zone. In other words, the mappings cover the highly deformed regions near the deformation surface to the undeformed region inside the sample. The mappings in the direction parallel to the deformation surface serve to increase the statistics of the deformation depth measurements. They are also useful to show possible inhomogeneities in the deformation region.

For analysis, the mappings must be stitched together to create one single mapping covering the whole collected area. The stitching operation refers to the action of positioning images with respect to each other and joining them together. In the case of an EBSD data set, stitching involves the combination of the information contained in each mapping (orientation, quality metrics, *etc.*) as well as the diffraction patterns. Commercial software provides tools to stitch different mappings together, but they do not offer the same possibility for diffraction patterns. A routine was written in EBSD-Image to overcome this limitation and allow a better analysis of our results. The stitching algorithm utilizes EBSD-Image's open formats (EBSD multi-map and SMP file) to simultaneously combine the information contained in the mappings and diffraction patterns. The number of diffraction patterns matches the number of pixels in a map of the multi-map. If two mappings overlap each other, diffraction patterns of only one mapping are kept in the SMP. Conversely, if there is a gap in between two mappings, blank diffraction patterns (black images) are created and saved in the SMP. The result is a single EBSD

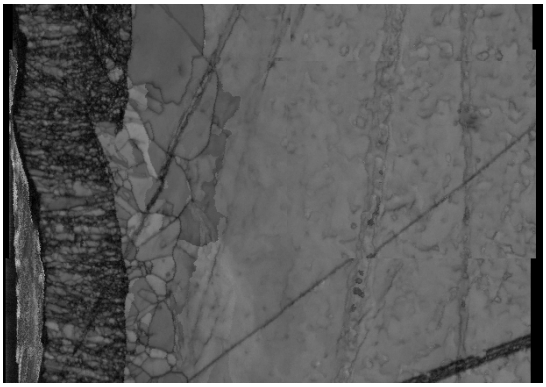

Figure 5.16: Mapping based on the band contrast quality metric showing regions of low diffraction quality. These regions corresponds to scratches and grain boundaries.

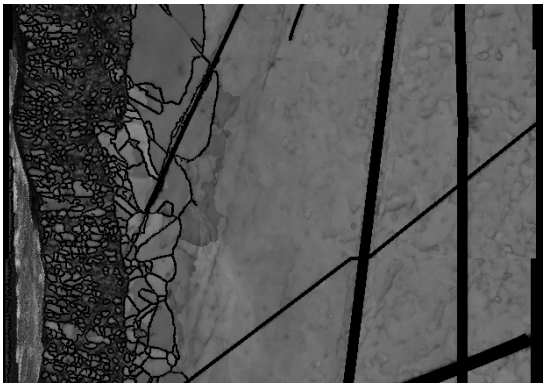

Figure 5.17: Mapping based on the band contrast where scratches and grain boundaries are removed (appear in black).

multi-map and SMP file which are completely independent from the original mappings before stitching.

5.2.2.4 Removal of Artifacts

As mentioned by Wu et al. [26], grain boundaries and surface defects are regions in a mapping where diffraction patterns have a lower quality. To eliminate the effect of these elements on the calculation of deformation depth, they are excluded using a mask. Surface defects such as scratches and debris are easily identifiable and can be manually removed. As for grain boundaries, a two pixels wide region along each grain boundary is added to the mask. The detection of grain boundaries was performed with the HKL Channel 5 software using a 5° misorientation criteria. This information was then processed using EBSD-Image to create the two pixels wide region. The final mask to be applied on each map is a combination of the mask of the surface defects and the one of the grain boundaries. Figure 5.16 shows an EBSD map of the band contrast where scratches and grain boundaries can be found. Figure 5.17 is the result after applying the mask. The excluded pixels appear in black.

5.2.2.5 Deformation Profile

For all of the samples in this study, the level of deformation should be at its maximum near the deformed surface. From the maps of quality metrics the level of deformation can be estimated, as it is inversely related to the quality of the diffraction patterns. The

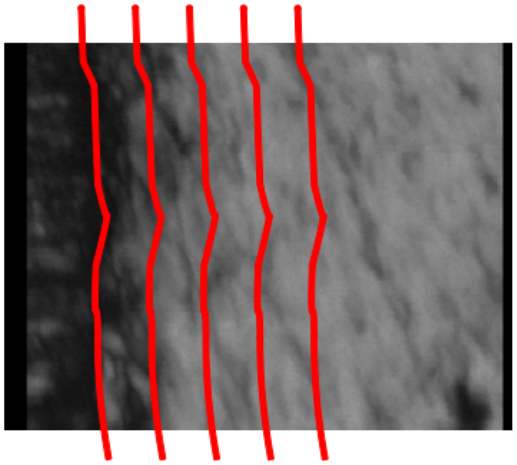

Figure 5.18: Schematic representation of the slices to calculate the deformation profile. The mapping shows the band contrast quality metric.

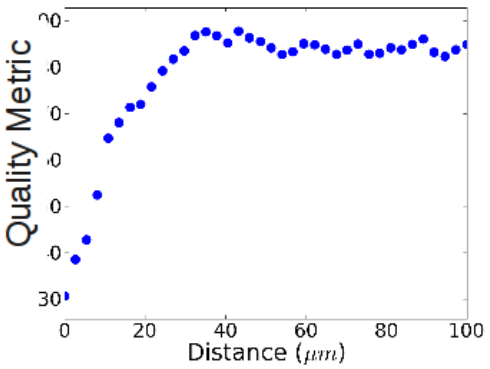

Figure 5.19: Typical deformation profile calculated from the slices in Figure 5.18.

values in the quality maps are expected to increase as a function of the distance from the deformed surface up until the undeformed region. This variation should increase monotonically as the samples were uniformly deformed by saws or grinding paper.

To obtain such a profile, the following steps were performed on each map of the different samples. The first step is to precisely determine the coordinates of the deformed surface, because of the electroplated layer of Ni, the latter does not correspond to the edge of the sample. In addition, the surface is not a straight line due to the deformation induced by the hack saw, abrasive saw or grinding papers. A zig-zag line made out of several points is used to delineate the surface. The second step is to segment the map into successive vertical slices starting from the deformed surface. All of the slices have the same thickness and therefore the same number of pixels. Figure 5.18 schematically shows four slices of a given map. The first red line from the left corresponds to the deformed surface. In reality, about twenty-five 10 px wide vertical slices are taken per map. The final step is to calculate the mean value of the pixels inside each slice. This value is plotted as a function of the distance of the slice from the deformed surface. The greater the number of pixels in a slice, the better the statistics of the profile. Figure 5.19 gives an example of a typical profile.

The deformation depth can be defined as the distance from the deformed surface, where the quality is at 90% of the plateau. In other words, the depth extends from the deformed surface up to a region with a deformation level of 10%. To find the deformation

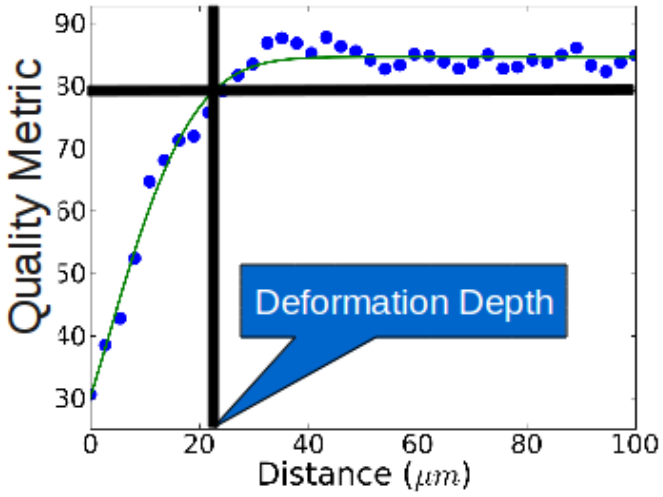

Figure 5.20: Fit of the error function over a typical deformation profile.

level on the profile, the error function (erf) was fit to the data. This sigmoid function has no scientific relationship with the actual variation in deformation level. Nonetheless, it characterizes well the trend observed in the deformation profiles. The error function allows the 90% value of the plateau to be properly identified and the deformation depth to be calculated as shown in Figure 5.20.

The deformation profile obtained with some quality metrics does not respect the initial assumption of monotonically increasing variation. Some are insensitive to the deformation while others have large fluctuating variations. In these cases, the fit between the error function and the data is poor: these quality metrics do not provide a good measure of the level of deformation. The criteria used to judge the sensitivity of a quality metric to deformation was the coefficient of determination, R^2, of the error function. If the coefficient is below 0.5, we can conclude that a quality metric cannot be used for deformation determination.

5.2.2.6 Deformation Contours

The profiles give an average deformation depth along the deformed surface. Inhomogeneities and variation of the deformation depth are averaged out by the vertical slides. This means that higher deformation values near scratches on the deformed surface and

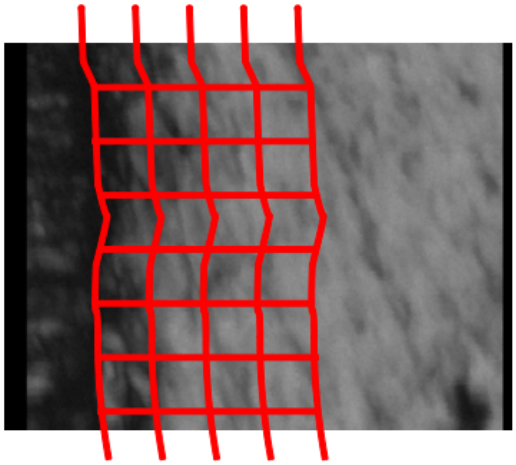

Figure 5.21: Schematic representation of the grid to calculate the deformation contours. The mapping shows the band contrast quality metric.

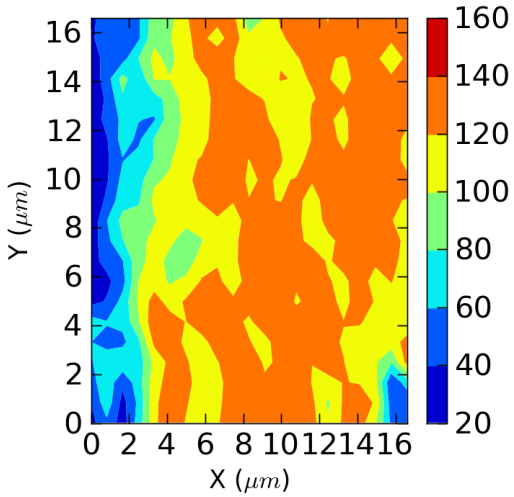

Figure 5.22: Typical contour plot calculated from the grid in Figure 5.21.

the effects of surface roughness cannot be studied using these profiles. Another way to look at the data is to create contour plots of equal diffraction quality. Similar to the profiles, the mapping of a given quality metric was segmented into small areas of equal width and height, that is the vertical slices of a profile were horizontally split, creating a grid as shown in Figure 5.21. The mean value of the pixels in each square was calculated. The position of a square is determined by its horizontal distance from the deformed surface and its vertical distance from the bottom left corner of the mapping. A contour plot was generated by interpolation between the mean values of all the squares. A color coded legend is used to show the variation in the quality going from blue to red. Figure 5.22 illustrates the contour plot of Figure 5.21.

5.2.3 Results

5.2.3.1 New Quality Metrics

An objective of this study was to determine which quality metrics are more suitable to detect variation in deformation level. In section 2.3, several quality metrics found in the literature were described. Some of them were successfully used to study deformed samples, while others did not give any deformation information. Based on the concepts used in the elaboration of these quality metrics, new ones can be defined in EBSD-Image.

The flexible structure of the software facilitates the implementation and the evaluation of any quality metric.

We shall use a systematic approach to define these new quality metrics. As mentioned in section 2.3, the quality of diffraction patterns can be directly estimated from the diffraction patterns or calculated from the intensity of the peaks in Hough space. From an implementation point of view, these two categories use different information to calculate quality metrics, one is based on the diffraction pattern and the other on the detected peaks and their intensity. The intermediate step between these two types of information is the Hough transform. Logically, the result of the Hough transform, the Hough space, can provide a useful evaluation of diffraction quality. Different mathematical and statistical operations can be performed on these sources of information to obtain a value expressing the diffraction quality. For instance, Tao [8] used the average, standard deviation and entropy of the diffraction patterns. Other simple operations are the range (the difference between the maximum and the minimum value of a data set), the sum (the addition of all the values of a data set), or the number of items in the data.

By combining the three sources of information (diffraction pattern, Hough space and detected peaks) with these operations, we obtain a table of 18 possible quality metrics. Taking the average operation as an example, quality metrics can be calculated from the mean of the pixels of the diffraction pattern, the pixels of the Hough space or the intensities of the detected peaks. Interestingly, the latter quality metric is equivalent to the aforementioned image quality. Two quality metrics can however be removed from the list: the operation evaluating the number of items in the data does not apply to the diffraction pattern and Hough space since the number of items, in occurrence with the number of pixels is constant. It is only valid for the detected peaks.

Apart from these 16, we introduce four other quality metrics in this study. They are based on the difference between the maximum and minimum value inside each detected peak, *i.e.* the range operation is applied on every detected peak. From the Bloch wave theory, Kikuchi bands are characterized by a bright center and dark edges (see section 2.1). The difference between the center of a band and its edges is a measure of the sharpness of the band, and is therefore an estimation of the deformation level. In Hough space, this is translated into an intense peak corresponding to the center of the band and two dark regions corresponding to the dark edges. The difference between the maximum and minimum value inside a peak is therefore equivalent to the contrast between the center and edges of a band. It is important for these calculations that the area of the detected peaks includes both the bright and dark regions of the peak. In

EBSD-Image, the area of the detected peaks can be increased by performing one or two opening operations on the binary image obtained from the peak detection operation.

From the difference values obtained for each detected peak, the average and standard deviation can be used to evaluate the overall diffraction quality. As the deformation level increases, the average difference should decrease as the band sharpness decreases. A similar trend is expected for the standard deviation. For a high quality, undeformed diffraction pattern, the sharpness of the bands will have a large dispersion due to the variation of intensity in the Kikuchi bands. The Kikuchi bands of crystallographic planes with a high diffraction intensity have greater contrast than those of lower symmetry planes. However, for a diffraction pattern from a deformed region, the sharpness of all Kikuchi bands are decreased, thus decreasing the dispersion and lowering the standard deviation. Other quality metrics from these difference values can be the maximum and minimum difference between all the peaks. We shall refer to this group of four quality metrics as the local difference metric.

5.2.3.2 Deformation Depth

After the quality metrics were calculated for every diffraction pattern of every mapping, deformation profiles were generated to evaluate the deformation depth using the method described in the experimental procedure. The profiles of the iron and copper control samples show no apparent deformation. Figure 5.23 compares the profile of the control and SiC paper 220 grit (smallest deformation). The values are calculated from the Fourier quality metric. There are small variations in the profile of the control sample which could be related to surface cleanness and polishing relief. These effects combined with the difficulty of properly identifying the edge of the sample (after the nickel plated layer) may become an issue in the evaluation of smaller deformation depths. For instance, it may not be possible to reliably determine the deformation induced by finer grit paper or by diamond polishing with this method of analysis. These effects are not critical in the four deformation methods studied in this work as they all produce a relatively large deformed region in the order of a few microns.

Different deformation depths are obtained depending on the quality metric used, even if we exclude the quality metrics that do not evaluate deformation. The variation in the deformation depth indicates that some quality metrics may underestimate the deformation while others may overestimate it. A range of deformation depth is therefore reported in Table 5.2 which summarizes the deformation induced by the four metallographic preparation steps on copper and iron.

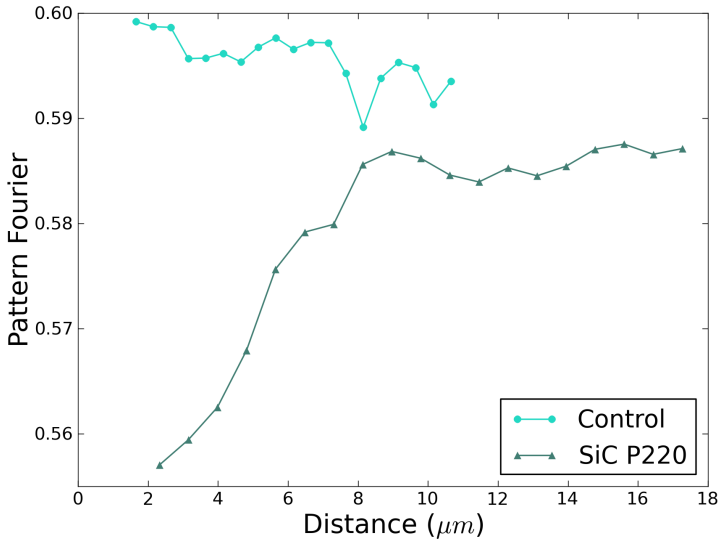

Figure 5.23: Comparison between the deformation profile of the control and 220 grit SiC paper. The profiles are from the copper samples. The Fourier quality metric is shown.

Deformation depth (μm)	**Copper**	**Iron**
Hack saw	40–70	20–40
Abrasive wheel cutting saw	30–40	15–20
SiC paper 80 grit	8–12	10–15
SiC paper 220 grit	4–6	2–4

Table 5.2: Deformation depths measured from the profiles of the quality metrics.

For a given metal, the deformation depth is approximately reduced by half between each step. From a sample preparation point of view these measurements show the advantage of using a precision saw with an abrasive cutting wheel to section the samples instead of a hack saw. The deformation induced by the latter may be difficult to completely remove with the subsequent preparation steps. Another observation from these results is that the deformation in the copper samples is always greater than that of the iron samples. This could be explained by the higher hardness of pure iron (150 HV [65]) versus that of copper (50 HV [65]) and the presence of more slip planes in the face centered cubic crystal (Cu) than the body centered cubic crystal (Fe).

These measurements are comparable with those obtained by Samuels [59]. In his book, he reported the depth of the significant deformation layer (approximately equal to the depth of the shear band layer) and the depth of the deformed layer of a 30% Zn

Depth (μm)	Significant deformation	Deformed layer
Hack saw	55	750
Abrasive wheel cutting saw	16	700
SiC paper 220 grit	7.5	77

Table 5.3: Depths of the signification deformation layer and deformed layer reported by Samuels [59] for a 30% Zn brass.

brass deformed using different techniques. The significant deformation depth is defined as the deformed region that "would noticeably affect the observations to be made on the finished surface" [59]. The Samuels' results are given in Table 5.3. The depths of the significant deformation layer are in the same range as those reported in Table 5.2 for copper.

Apart from the fact that the measurements were performed on two materials with different hardnesses, differences can be explained by two other factors. First, the EBSD measurements do not differentiate between the shear band, the significant deformation or the deformed layers. The measured deformation depth is only based on the variation of the quality of the diffraction patterns. This comparison shows that the EBSD measurements give a good estimate of the significant deformation layer, although a portion of the deformed layer may be included in the values reported in Table 5.2. It also demonstrates the limitations of current technique to measure small strain levels. Secondly, Samuels' values were obtained by visual inspection of the LOM and TEM micrographs instead of a quantitative determination of the deformation profile. It is therefore difficult to assess possible variation in the deformation depths in his measurements. However, one could argue that visual inspection may help to identify small strained regions in the quality mappings.

5.2.3.3 Inhomogeneities

Inhomogeneities in the deformed region were evaluated using the contour plots. Figures 5.24 to 5.27 show the contour plots of the iron samples deformed with the hack saw, abrasive wheel cutting saw, 80 grit SiC paper and 220 grit SiC paper, respectively. The entropy calculated directly from the diffraction patterns is the quality metric used in the four figures. The deformed surface is located on the left side of the figure ($x = 0\,\mu$m). The deformation profile can be visually inspected by the gradual change from low quality regions (blue) to higher quality regions (red). The white regions in the figures are due to the removal of artifacts. Only a portion of the area collected for each sample is shown

in the figures due to space limitations.

Inhomogeneities in the deformation depth is apparent in all four deformation methods. The deformation front is not always parallel to the deformed surface. For example, regions with a higher level of deformation can be seen in Figure 5.24 around $y = 550\,\mu$m or in Figure 5.27 around $y = 19\,\mu$m. These results show the importance of collecting many mappings since the deformation in one mapping may not be representative of the whole sample.

5.2.4 Discussion

5.2.4.1 Evaluation of Quality Metrics

By comparing the different deformation profiles and contour plots produced for each sample, the different quality metrics can be evaluated based on their ability to assess the level of deformation. This study did not look at the influence of the experimental conditions on the quality metrics. The beam energy, the size of the diffraction patterns, *etc*.could change the sensitivity of the quality metrics. Despite using two different microscopes for the acquisitions, these parameters were kept constant. Furthermore, the same Hough transform resolution ($\Delta\theta = 1\,^\circ/\text{px}$) as well as the same algorithms for peak detection (top hat thresholding) and peak identification (local centroid) were used for all the quality metrics. It is certainly possible that the algorithms used could influence the value obtained from the quality metrics. For instance, the peaks detected from a diffraction pattern and consequently the intensities used in the quality metrics calculations may change based on the selected peak detection algorithm. Our comparison is therefore qualitative and closely linked with the scope of this work which is to measure the deformation depth induced during different steps of a sample preparation procedure.

We shall define three categories of quality metrics based on their ability to evaluate deformation. A good quality metric must meet the following requirements for all iron and copper samples: (i) a good fit of the error function to its deformation profile, (ii) similar deformation depth to other quality metrics for a given sample, and (iii) low number of inhomogeneities in its contour plot. A fair quality metric would comply with some of these requirements but not all of them or only for some samples, whereas a bad quality metric does not meet any requirements. Table 5.4 summarizes the evaluation of some of the quality metrics. Other good quality metrics are the band contrast, the band slope and the one calculated from the Fourier transform. The pattern quality index gives a fair response to deformation as it could not correctly evaluate the deformation depth

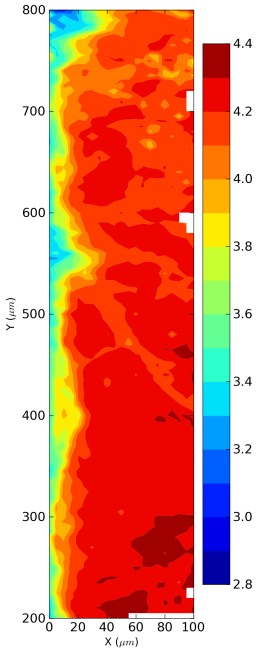

Figure 5.24: Contour plot of iron deformed with a hack saw. The pattern entropy quality metric is shown.

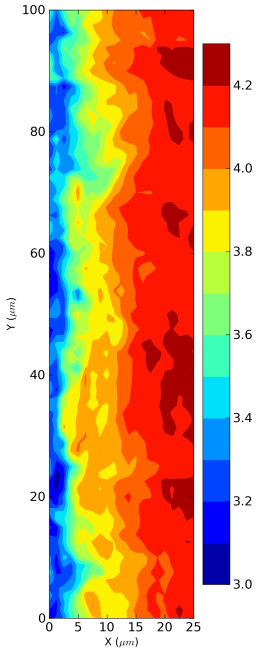

Figure 5.25: Contour plot of iron deformed with a abrasive wheel cutting saw. The pattern entropy quality metric is shown.

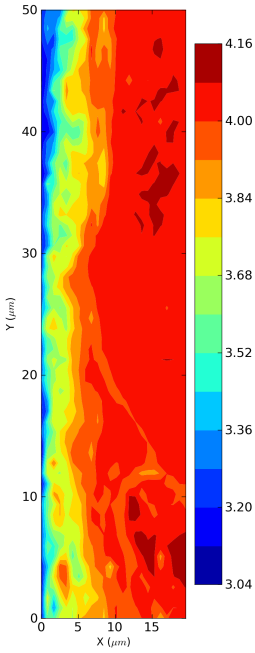

Figure 5.26: Contour plot of iron deformed with a 80 grit SiC paper. The pattern entropy quality metric is shown.

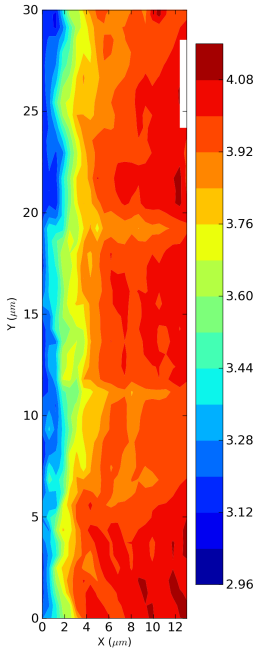

Figure 5.27: Contour plot of iron deformed with a 220 grit SiC paper. The pattern entropy quality metric is shown.

	Average	Standard deviation	Entropy	Range	Sum	Count
Pattern						N/A
Hough						N/A
Detected Peaks						

Table 5.4: Evaluation of the quality metrics on their ability to assess the level of deformation (green: good quality metric to evaluate the deformation, yellow: fair response to the deformation, works in some cases and not in others, red: quality metric gives no deformation information).

for all samples: its value was found to decrease in the undeformed region. The signal to noise ratio was not able to properly evaluate the deformation: this quality metric was inversely proportional to the deformation depth, having its maximum value at the deformed surface. The image quality (equivalent to the average of the detected peaks) is classed as fair since the deformation depth measured is always smaller than with the other metrics. It is however capable of determining the deformation depth for all samples. From the literature, different authors used this quality metric from the TSL EBSD software for deformation measurements [23, 28]. Discrepancies between the actual implementation of this quality metric and the published equation could explain the different behavior. Another explanation could be the algorithms used to detect the peaks in Hough space and identify their intensity. Figures 5.28 to 5.30 illustrates the contour plot of a good, fair and bad quality metric, in occurrence the Hough range, the image quality and the pattern average. All three figures are from a copper sample deformed with an abrasive wheel cutting saw.

The quality metrics based on the local difference within the detected peaks are also able to detect the level of deformation. It was found that the average and the standard deviation of the local difference values give similar deformation depth and distribution. On the other hand, a slightly greater deformation depth is measured if the maximum local difference is taken as a measure of quality (10% increase on average local difference). The minimum intensity difference does not seem to carry any deformation information. Quality mappings for the average, standard deviation and maximum local difference are respectively shown in Figures 5.31 to 5.33 for an iron sample deformed with an hack saw.

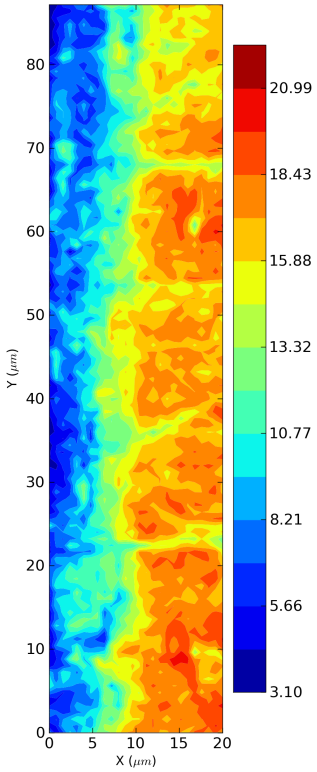

Figure 5.28: Contour plot of a good quality metric (Hough range) for the copper sample deformed by an abrasive wheel cutting saw.

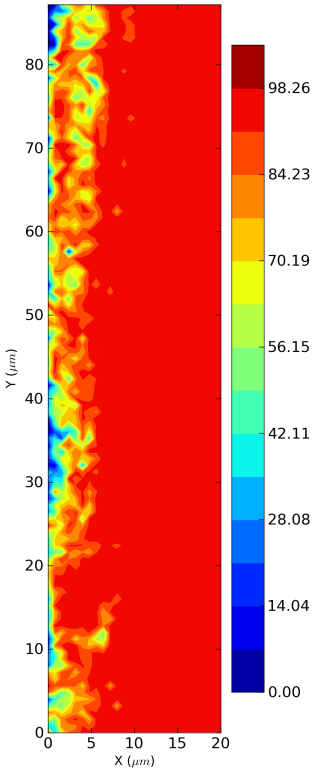

Figure 5.29: Contour plot of fair quality metric (peaks average, *i.e.* image quality) for the copper sample deformed by an abrasive wheel cutting saw.

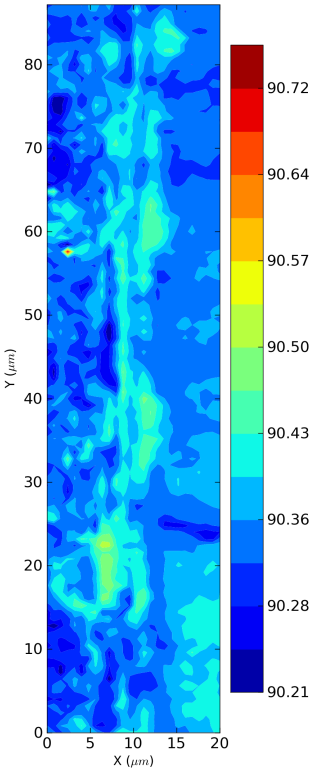

Figure 5.30: Contour plot of bad quality metric (pattern average) for the copper sample deformed by an abrasive wheel cutting saw.

The comparison of mappings from quality metrics using the diffraction patterns or the Hough space reveals some similarity between these two sources of information. For instance, calculating the entropy and the standard deviation on either of these two sources of information is almost equivalent. On the other hand, the contrast in the Hough range mapping is more enhanced than for pattern range mapping. It is interesting to point out that the Hough range has a similar appearance to the band contrast (calculated in HKL Channel 5), and that the local difference average approaches a similar contrast to the band slope (calculated in HKL Channel 5). These similitudes are however sample dependent. Of the two proprietary quality metrics from Oxford HKL systems, a greater deformation depth was obtained using the band slope (20-40% more) as it displays the level of deformation with a better contrast.

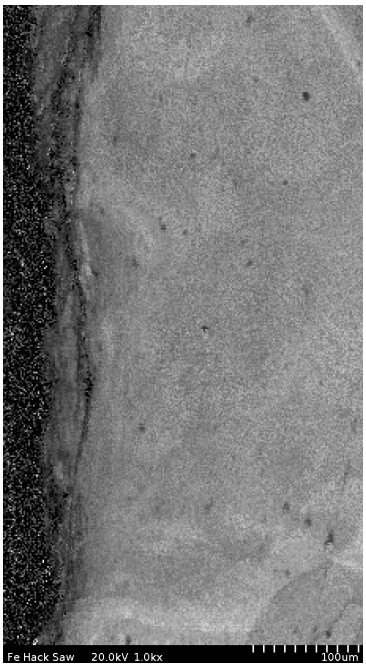

Figure 5.31: Mapping of the average local difference quality metric.

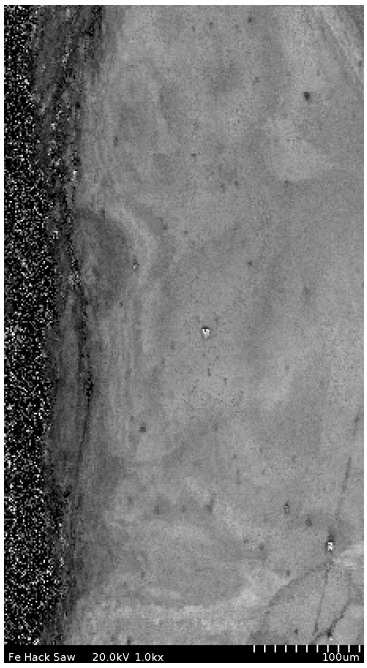

Figure 5.32: Mapping of the standard deviation local difference quality metric.

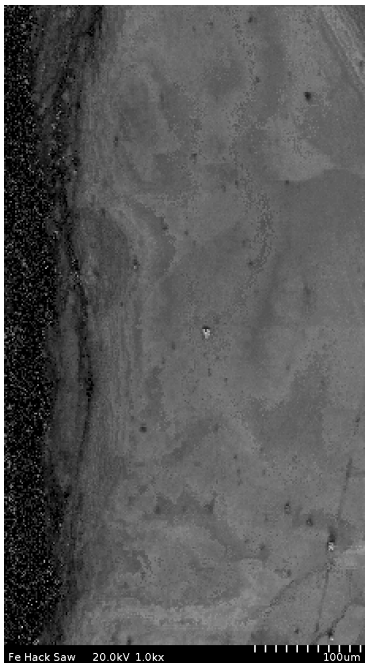

Figure 5.33: Mapping of the maximum local difference quality metric.

5.2.4.2 Comparison with Simulated Patterns

The classification of the quality metrics based on their ability to evaluate the level of deformation is in line with the results obtained using simulated diffraction patterns in section 3.3. The metrics found to be good experimentally match those which are strongly influenced by the sharpness of the Kikuchi bands in the simulations. This correlates with the observations of Wilkinson [22] and Keller [23] which reported blurring of the edges of the Kikuchi bands under plastic deformation. Figure 5.34 shows the effect of a smoothing filter of different sizes on all good quality metrics. All of them have a decreasing ratio as the size of the smoothing filter increases. In comparison, the fair quality metrics show a greater variation and have difficulty correctly evaluating low quality diffraction patterns (Figure 5.35).

This comparison demonstrates the utility of simulated patterns in the elaboration of new quality metrics to detect deformed regions within a sample. It also shows that quality metrics designed for deformation measurements should focus on evaluating the sharpness (or inversely the blurriness) of the edges of the Kikuchi bands.

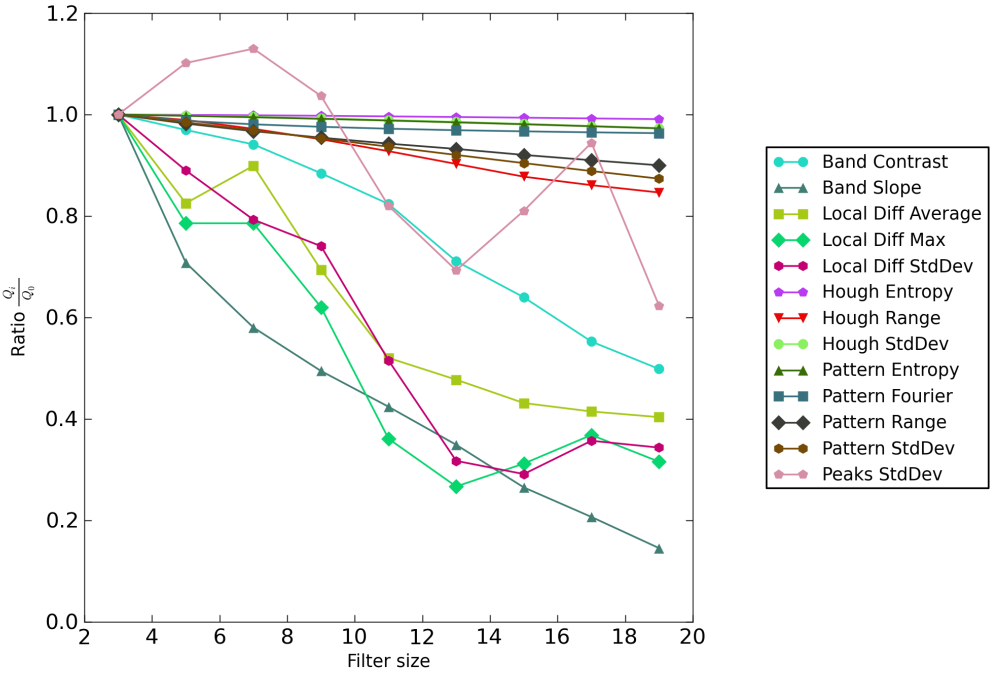

Figure 5.34: Variation of the good quality metrics as a function of the size of the kernel for the smoothing filter.

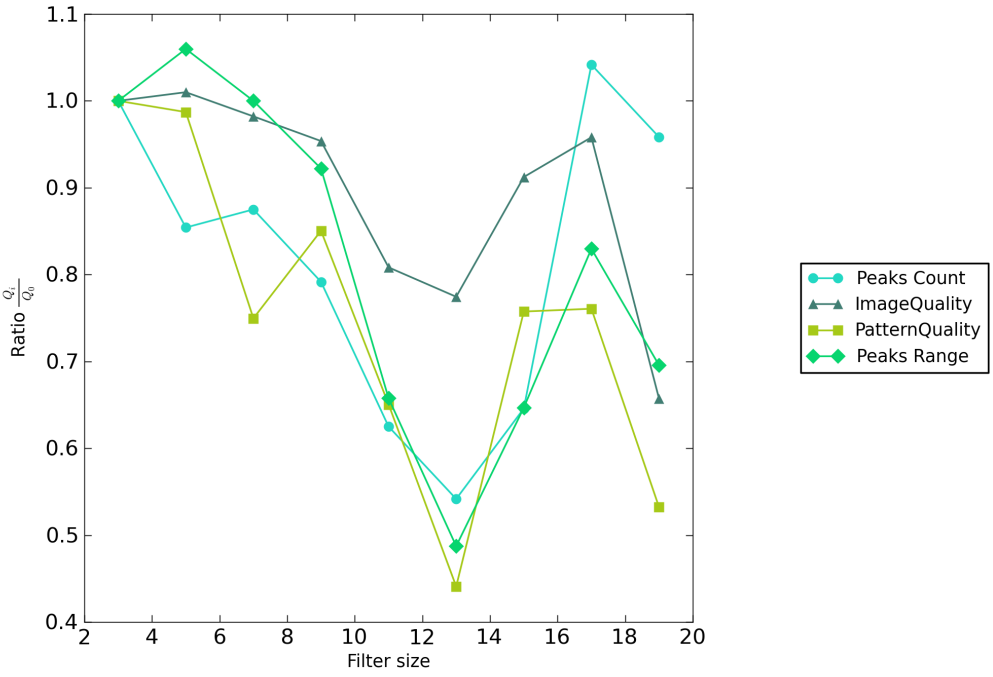

Figure 5.35: Variation of the fair quality metrics as a function of the size of the kernel for the smoothing filter.

5.2.5 Conclusion

This application illustrates the flexibility of the analysis engine to perform new calculations on diffraction patterns and extract more information from them. This study of the different quality metrics would not have been possible with commercially available software. The results reveal that several metrics can be used to detect deformation. Deformation information can be extracted directly from the diffraction pattern, the Hough transform or the detected peaks. Inhomogeneities in the deformation front illustrated by the contour plots show the importance of collecting data covering a large area to measure a statistically relevant deformation depth.

In this work, the effect of orientation on the quality metrics [28] was neglected for two reasons: (i) due to the high strain level, the effect of deformation to the diffraction quality is assumed to be greater than that of orientation (ii) samples with large grains ($> 1\,\mathrm{mm}^2$) were used. Nevertheless, these assumptions limit the scope of the results to very specific samples. The quality of a diffraction pattern changes with orientation because all crystallographic planes do not diffract with the same intensity. Depending on how a crystal is oriented, more or less intense Kikuchi bands are present in the diffraction pattern. This effect could be theoretically eliminated by tracking the Kikuchi bands of specific crystallographic planes in the diffraction patterns and using their intensity and sharpness in the calculations of the quality metrics. For example, in a face centered cubic crystal, only the intensity of the (111) planes could be used regardless of the position of these planes in a diffraction pattern. This stratagem, however, requires an accurate indexing of the diffraction patterns to identify the crystallographic planes. It would therefore only be applicable to map low to medium level of deformation.

Chapter 6

Conclusion

Diffraction patterns are the raw data of the EBSD technique. It has been shown by several authors that quality metrics can be used to extract more information from diffraction patterns than just orientation and phase. Although some quality metrics are implemented inside commercial EBSD acquisition software, the implementation of new metrics is not possible, leaving the users to design their own system. EBSD-Image provides an alternative solution to this problem. Its flexible analytical structure is designed to facilitate the implementation of recognized algorithms and the development of new ones. For instance, sixteen variants of the four quality metrics proposed by Tao, Wright and Nowell [8, 28] were used to analyze the deformation induced during sample preparation of two metallic samples. The simulation engine of EBSD-Image allowed for better understanding of these quality metrics and their ability to evaluate deformation. Simulated diffraction patterns are a useful tool for this type of analysis as they are easily generated using a known and controlled set of parameters. In line with the observations of Wilkinson and Dingley [22], we found — by using simulated diffraction patterns — that the level of plastic strain in a sample is linked with the sharpness of the Kikuchi bands. This result led to the development of new quality metrics based on the local intensity variation of the Hough peaks.

The flexibility of the analysis engine is not limited to the calculation of quality metrics: all of the operations used to process diffraction patterns are left to the user's discretion as well as the order in which these operations are performed. In the current version of EBSD-Image, basic algorithms are already implemented. However, the analysis engine is designed to allow the implementation of different new algorithms to meet the specific analytical needs of the user. Since EBSD-Image is an open source project, the number of available operations will grow with the collaboration of the EBSD community.

The integration of the simulation and analysis engines inside image analysis software gives users access to different routines to analyze samples. In the case of Zr-2.5Nb pressure tubes, the analytical functionalities of EBSD-Image were useful to confirm that the entropy quality metric provides better discrimination between the α-Zr and β'-Zr phases. The image analysis procedures already incorporated in the software also simplify the development of new operations.

In this work, the implementation of the Hough transform as described by Krieger Lassen [3] was adapted to ensure that the Hough peaks have an aspect ratio matching the butterfly filter. By selecting the increment of the Hough transform in θ, the resolution in ρ is automatically calculated for diffraction patterns of any size based on Equation 4.6 on page 63. Another improvement is the implementation of a method to properly identify the position of vertical Kikuchi bands. The representation of the continuous and circular Hough space in a discrete and bounded image leads to the problem of double peaks for these bands. The proposed method consists of expanding the upper θ boundary of the Hough space pass 180°. This strategy eliminates double peaks and ensures that there is no negative bias on the detection of vertical Kikuchi bands.

With the advancement of faster EBSD cameras, the size and/or the quantity of EBSD acquisitions, and consequently the number of diffraction patterns will increase in coming years. Utilities have been introduced in this work to process and analyze large data sets: (i) the SMP file (ii) the stitching of mappings and their diffraction patterns (iii) the use of a distributed computing grid. The SMP is a simple file format to store, transfer and process diffraction patterns. It solves problems encountered with the individual diffraction pattern storage method presently used by commercial software. In order to analyze a large area of a sample, a common practice is to stitch several mappings together. EBSD-Image allows the combination of the results of mappings as well as the diffraction patterns, thus facilitating the re-processing of a whole mosaic. An interesting avenue to process large data sets is to distribute the processing on several processors. The structure of the analysis engine was designed so that it could be used for this case and provides specific tools to run an analysis on a distributed computing grid.

One important aspect of processing diffraction patterns is the indexing algorithm. As discussed in Appendix A, the latter plays a large role in the determination of the resolution. Its ability to find a reliable indexing solution of a diffraction pattern containing Kukuchi bands of two grains or two phases will determine the effective resolution of EBSD. The benchmarking of current indexing algorithms would be an interesting avenue for future research and provide an opportunity for improvement. It would also give

way to a more standard approach to compare the experimental resolution measurements performed on different EBSD systems.

In summary, EBSD-Image offers a research and development platform to improve the EBSD technique and ultimately allow for the characterization of smaller features and more complex materials. The philosophy of the software is to encourage collaboration within the EBSD community to develop better and more appropriate algorithms for solving common problems in the fields of materials engineering and geology. The presented work is the first iteration towards this objective.

Appendix A

Resolution

A.1 Resolution

The precision of an EBSD mapping depends on two resolutions. First, the ability of EBSD to characterize small phases or grains in a microstructure is related to its spatial resolution. As in the case of X-ray microanalysis, it corresponds to the volume in the sample from which the signal in a diffraction pattern originates. Secondly, the precision of the orientation measurements of EBSD depends on its angular resolution. We shall elaborate on the factors influencing these two resolutions and summarizes the measurements performed in the literature to quantify them.

A.1.1 Spatial

The interaction volume of the diffracted backscatter electrons is closely related to that of the incident electrons. It is well known that the latter increases with the energy of the incident electrons, decreases with the material's density and decreases with the atomic number [66]. Furthermore, the shape of the volume varies if the sample is tilted as is the case for EBSD analysis (Figure A.1). The high tilt angle brings the electron interaction volume closer to the surface, thus improving the depth component of the spatial resolution (δ_z) as well as increasing the backscattering yield. The tilt also creates an anisotropic spreading of the incident beam. From the sample surface, the electrons are effectively travelling more inside the sample in the direction perpendicular to the tilt axis (δ_y) than they are in the direction parallel to the tilt axis (δ_x). The spatial resolution is therefore better along the tilt axis.

Ren et al. [67] as well as Zaefferer [1] used Monte Carlo simulations to evaluate

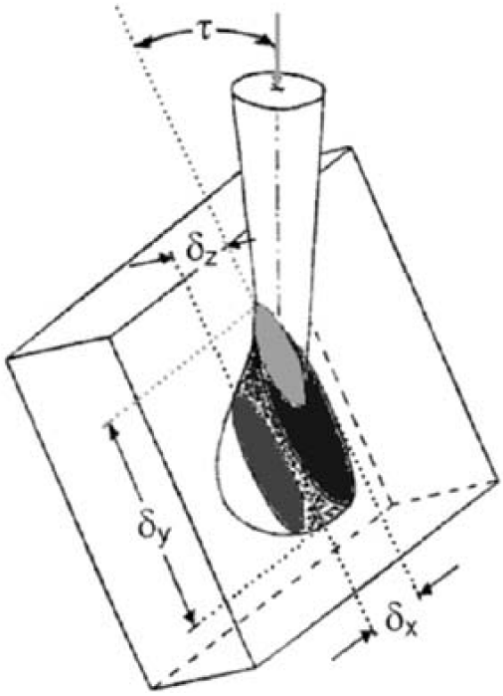

Figure A.1: Schematic representation of the interaction volume for a sample tilted by an angle τ where δ_x is the resolution parallel to the tilt axis, δ_y the resolution perpendicular to the tilt axis and δ_z the depth resolution [7].

the spatial resolution of EBSD. They made the assumption, which was experimentally re-assessed by Deal et al. [68], that the electrons responsible for the formation of the Kikuchi bands are backscattered electrons having an energy very close to the energy of the primary beam. The simulations confirmed the expected dependence of the resolution on the beam energy, the material's density and average atomic number, and the direction with respect to the tilt axis. The longitudinal resolution (perpendicular to the tilt axis) is about 3-4 times greater than the lateral resolution (parallel to the tilt axis) [1, 67, 69]. A limit of the Monte Carlo simulations is that all the current models do not consider the crystalline nature of the matter: from the simulation point of view, the sample is amorphous. Channeling effects are not considered.

Experimental measurements of the spatial resolution have been performed by many authors [1, 69–72]. Apart from the operating conditions of the microscope (beam energy, type of emitter, probe diameter) and the sample used, another important factor in the determination of the spatial resolution is the algorithm used to detect and index the diffraction patterns [69]. For instance, if the lateral spatial resolution is measured across the boundary of grain $\mathcal{A}$ and $\mathcal{B}$, the diffraction pattern collected exactly at the grain

Energy (keV)	Al	Fe	Ni	CuZn	Au
10			50 (FEG)[1-3][71]		
15		35 (FEG)[1-4][1]			
20	250 (W)[1][73] 20 (FEG)[2][35] 60 (W)[2][35]	10 (FEG)[2][35] 30 (W)[2][35]	100 (FEG)[1-3][71]	9 (FEG)[2][35] 25 (W)[2][35]	
25	6 (FEG)[2][70]				
30	400 (FEG)[1-3][71]				20 (FEG)[1][72]
40	600 (W)[1][73]				

[1] Qualitative observation of diffraction patterns (no indexing)
[2] Using an acquisition software (with indexing)
[3] Step size of 50 nm
[4] Step size of 10 nm

Table A.1: Spatial resolutions along the direction of tilt axis reported in the literature.

boundary is the combination of the diffraction pattern of grain $\mathcal{A}$ and the one of grain $\mathcal{B}$. As the beam moves away from the grain boundary into either grain, the diffraction signal coming from the other grain decreases until a point where only the signal of one grain is present in the diffraction pattern. The absolute resolution is therefore defined as the distance between these points in grain $\mathcal{A}$ and $\mathcal{B}$. However, the effective resolution is smaller since "if there is a significant difference in intensity of the patterns, the acquisition software can successfully analyze the stronger pattern" [69]. Herein lies the importance of band detection and indexing algorithms in the determination of the effective spatial resolution. The difference in the measurements due to this factor can be seen in Table A.1 where the reported experimental spatial resolution along the tilt axis direction of different authors are summarized.

Fewer experimental measurements were performed on depth resolution. Zafferer found that the quality of the diffraction pattern was reduced by half after the deposition of a 2 nm thick layer of amorphous Cr on a Ni sample (beam energy of 15 kV). With 5.5 nm thick layer, only 10% of the original pattern intensity was left. This demonstrates the high surface sensitivity of EBSD.

A.1.2 Angular

The angular resolution can be evaluated as a function of its accuracy and precision. The factors influencing these two aspects of the angular orientation can be easily understood by considering an EBSD mapping of a single crystal with a known orientation. First, the value of the orientations reported by the EBSD software should all be equal to

the expected orientation of the single crystal. Misalignment of the sample or internal calibration of the camera with respect to the microscope reference frame are responsible for the difference between the experimental and theoretical orientation [69]. This error is evaluated to approximately 0.5-2° [5, 69]. A good accuracy is particularly desirable for texture analysis.

On the other hand, the precision is an important factor for the measurement of grain boundaries, especially low angle grain boundaries. From the example, a mapping of a single crystal should always return the same orientation for all the pixels. Variation within the reported orientations is related to the acquisition parameters such as the size of the diffraction pattern (i.e. binning), the calibration, the resolution of the Hough transformation and the bands detection algorithm [69, 70]. The precision of the angular resolution is around 1° for a well selected set of parameters [35]. It could be further improved with high quality diffraction patterns [74].

Appendix B

Acquisition of Diffraction Patterns

The acquisition of high quality diffraction patterns requires the optimization of the microscope and camera operating conditions. The selection of the acquisition parameters will depend on the sample to be analyzed, how it was prepared, what are its constituents, the type of analysis, etc. Understanding the parameters and limitations of EBSD is paramount to correctly setting-up the automated acquisition. Another aspect of an EBSD acquisition is the calibration of the system to obtain reliable orientation results. In short, the calibration is the relationship between the reference frame of the camera and the one of the sample.

B.1 Hardware

The required hardware to perform an EBSD acquisition can be summarized as two main components: (i) a scanning electron microscope (ii) an EBSD camera.

B.1.1 Microscope

The microscope is the source of the incident electrons that will diffract in the sample and create the diffraction pattern. Ideally, the microscope should be able to produce a high and stable probe current while maintaining a small beam diameter — the latter becomes critical for high resolution applications. The current is important since it is directly linked with the time required to acquire a diffraction pattern. The higher the current, the greater the number of electrons hitting the sample and diffracting onto the camera. This only applies if the sample is conductive, else charging effects on the surface will eliminate any benefits of a high current. Unstability in the current will create

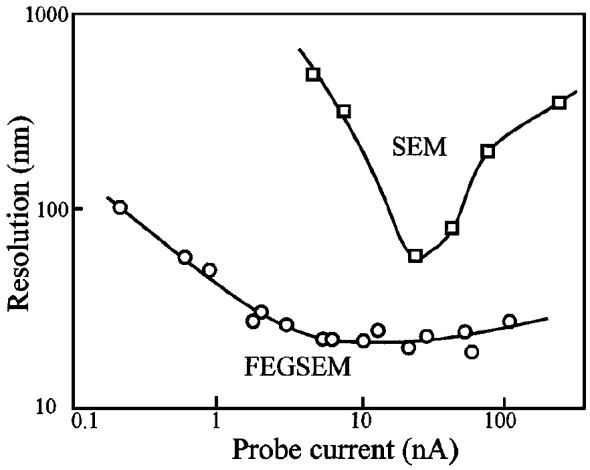

Figure B.1: The effect of the probe current on the EBSD spatial resolution between a W-filament microscope (labeled SEM) and a field emission microscope (labeled FEGSEM) on an aluminum sample [69].

fluctuations in the quality of the diffraction patterns and may lead to mis-indexing [5].

Humphreys compared the spatial resolution achievable with EBSD using a W-filament and a field emission gun (FEG) microscope [69]. As shown in Figure B.1, the resolution is less influenced by the probe current on a FEG than on a W-filament SEM. Schottky field emitter microscopes, which are common analytical microscopes used for EBSD, have a similar behavior to FEG SEMs at the energy range of EBSD [5]. As described in Appendix A, the spatial resolution also depends on other factors beside the type of microscope.

Another consideration is the arrangement of the stage and different detectors inside the chamber of the microscope. The stage must be able to tilt to a high angle (60-70° from the horizontal) and remain stable at this position for extended periods of time — drift of the sample would completely ruin an acquisition. A pre-tilted holder is often used to eliminate this problem for high resolution mapping. It however limits the movement of the sample once inside the chamber. The EBSD camera must be positioned very close to the sample in order to receive as much of the signal as possible [9]. This necessitates the chamber to be designed to provide a free path to the EBSD camera when inserted. The positioning of the X-ray detector should also be considered to achieve a high count rate if a simultaneous EBSD-EDS acquisition is performed. Most modern microscopes are designed to have such an arrangement.

The accelerating voltages used for EBSD maps range between 10 to 30 keV [5]. This is easily achievable by any microscope. Using an energy filtering apparatus, Deal et al.

[68] showed that backscattered electrons that principally contribute to the formation of a diffraction pattern have an energy greater than 97% of the incident beam energy. Lower energy electrons have a small contribution and mainly cause blurring of the Kikuchi bands. Since electrons loose energy as they travel inside the sample, the ones with a small energy loss are located close to the incident beam. With a low accelerating voltage, the interaction volume is decreased, and smaller features can be analyzed. However, the sensitivity of the camera also decreases with the accelerating voltage, thus limiting the benefit of the small interaction volume.

B.1.2 Camera

The EBSD camera consists of a phosphorous screen, a charge coupled device (CCD) and a frame grabber. The phosphorous screen converts the backscattered electrons to photons that are detected by the CCD which then converts them to an electrical signal. The electron to photon conversion requires the electrons to have a minimum energy. The efficiency of this process drops with the accelerating voltage [69]. After the amplification of the electrical signal, the frame grabber converts this signal to a 12-bit image [20, 21, 75]. The background noise, coming from backscattered electrons that do not carry diffraction information, is removed by subtraction or division [9]. The image of the background noise is recorded by scanning the electron beam over several grains.

The parameters of the camera vary from one manufacturer to another, but the common parameters are: the integration time, the image resolution, the gain and the number of averaged frames. The integration time is the time required to acquire a diffraction pattern. This quantity is also often expressed as a speed in patterns per second. In other words, it corresponds to the amount of time the CCD is collecting photons to create an image. If the integration time is too long, the camera will be over-saturated and the image will completely white. Conversely, if it is too short, the image will be noisy and the Kikuchi bands will be barely recognizable: the signal to noise ratio will be low since an insufficient amount of diffracted electrons were collected.

To increase the speed of the camera, the different channels of the EBSD camera can be binned together [70]. For instance, a modern high sensitivity camera has a typical resolution of 1300x1000 pixels (i.e. 1300 channels wide and 1000 channels high) [20, 21, 75]. By combining the information of neighboring channels, the integration time can be decreased. A 4x4 binning implies than the resolution of the camera was reduced by a factor of sixteen which results in an increase of its speed. For well diffracting samples and standard EBSD analysis, this does not influence the final results. However strain

[38] or lattice parameters measurements [76] require high resolution diffraction patterns and high binning should be avoided. Most manufacturers of EBSD systems offer two types of camera: a high sensitivity and a high speed camera [20, 21]. The increase in speed (approximately 800 patterns per second [75]) is achieved by a smaller CCD, a different type of phosphorous screen, high speed electronic control and specially designed acquisition software [5]. A high probe current is mandatory to take full advantage of such camera.

The gain changes the amplification of the signal detected by the CCD. A high gain increases the sensitivity to electrons meaning fewer electrons are required to form a diffraction pattern and the integration time can be reduced. It is important to realize that the intensity of all electrons are amplified, not only those that form the Kikuchi bands. An over-increase in gain leads to noisy diffraction patterns. By lowering the gain, the integration time increases to allow for the collection of more electrons. In short, the integration time increases the signal to noise ratio, but the gain increases the signal as well as the noise [6]. One way to lower the noise level is to average several frames of the same diffraction pattern. This increases the total time required for the acquisition of a diffraction pattern but the noise level decreases without changing the integration time. The user must often choose between a longer integration time with a low gain and 1-2 averaged frames versus a shorter integration time with a high gain but with more averaged frames [21]. Experience has shown that for a well diffracting sample the total time of the two procedures is similar.

The set-up of the camera is an optimization of the parameters to obtain diffraction patterns with a good signal to noise ratio while keeping the recording time to a minimum. The acquisition of good quality diffraction patterns is important since they are the raw data used by the following software-based processing stages.

B.2 Calibration

As with any measurement apparatus, the EBSD system must be calibrated for the operating conditions before an acquisition. The calibration consists of three parameters to locate the position (x, y and z) of the camera with respect to the sample. Regardless of the system of axes used, the software refers to these parameters as the pattern center and detector distance (also known as camera length). The pattern center is defined as: "the foot of a perpendicular line from the phosphor screen to the beam spot on the tilted sample surface" [9]. Consequently, the detector distance is the smallest distance between

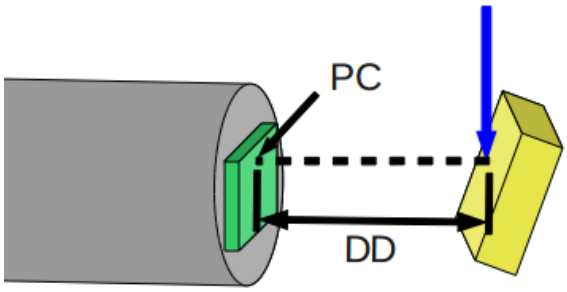

Figure B.2: Schematic representation of the pattern center (PC) and detector distance (DD).

the phosphorous screen and the beam spot on the tilted sample surface. Figure B.2 geometrically illustrates the definition of these parameters.

In other words, the calibration is the relative position of the camera with respect to the intersection point of the electron beam with the sample. This implies that if the camera or the sample are moved, the calibration must be adjusted. The movement of the camera is uniaxial; it can be inserted and retracted along one axis. On the other hand, the sample can be moved in three directions using the mechanical stage. From the point of view of the calibration, the only displacement of the sample that needs to be considered is the one along the axis of the electron beam, i.e. the working distance of the microscope. The movement of the sample in the other directions does not influence the relative position between the camera and the sample. Furthermore, the calibration is independent of the beam energy, probe current, type of sample and tilt. Based on these principles, it is common to have multiple stored calibrations for different working distances and camera insertion positions [20, 21].

The accuracy of the pattern center and detector distance is crucial for the indexing since they are required in the calculations of the angles in between the Kikuchi bands. An incorrect calibration can lead to errors in the indexing or simply to a lower indexing rate. There are different techniques to properly calibrate the EBSD system depending on the EBSD software used. A common technique is to iteratively refine the indexing of a diffraction pattern coming from a known crystal lattice orientation, typically a single crystal [9]. The calibration parameters are optimized to obtain the best fit between the experimental and calculated Kikuchi bands.

During a mapping, the pattern center and the detector distance will change based

on the vertical position of the electron beam on the sample. This is more apparent in a low magnification mapping. In a sense, the calibration is only valid at the center of the map. To compensate for this effect, EBSD software offers the possibility to dynamically change the calibration depending on the beam position and tilt of the sample.

Appendix C

Orientation Representation

There are many different ways to represent a rotation in three dimensional space. Some representations are easier to visualize and understand whereas others are simpler for performing calculations. These representations include Euler angles, rotation matrix, axis-angle and quaternion. In EBSD-Image, the quaternion is the default representation for rotations. Although utilities allow to convert quaternions to any other types of representation, rotation information are always internally stored as quaternions.

A quaternion is an algebraic system composed of one real dimension and three complex dimensions [77]. It is often expressed as a scalar value (real dimension) and a vector (complex dimensions). Quaternions have the following advantages over the other rotation representations: (i) simple algebra [46] (ii) less computation required than rotation matrix to combine two rotations [78] (iii) easy to determine geometrically (similar to axis-angle) [77] (iv) behave correctly near the identity (as opposed to Euler angles which have singularities). [77, 79]

In this appendix, the quaternion algebra used in EBSD-Image will be presented, followed by the applications of this algebra to common operations on rotations. Furthermore, a summary of the conversion methods between the different types of representation will be given. The derivations and demonstrations of the concepts presented in the following paragraphs are intentionally not included as they can be found in the cited literature.

C.1 Algebra

Quaternions can be represented with different notations; the scalar-vector and the coefficients notation will be used in the following explanations. As mentioned previously,

a quaternion is composed of a real scalar number a and a vector $\vec{A}$ of three complex numbers. The scalar-vector notation expressed a quaternion $\mathcal{A}$ as $[\![a, \vec{A}]\!]$, whereas the coefficients notation expressed the same quaternion as a vector with four coefficients $[\![a, A_x, A_y, A_z]\!]$. Note that in the latter notation, the real number is the first coefficient (the position of this coefficient can change from one reference to another).

Quaternions are not only used to represent rotations. Their algebra therefore includes many operations that are beyond the scope of this project. An excellent reference for a detailed description of the complete quaternion algebra is the book *Rotations, quaternions and groups* by Altmann published by the Oxford University Press [77]. Another reference is the online encyclopedia developed by Baker on 3D mathematics and their applications [79].

Four main operations are necessary for rotation manipulations using quaternions: the product, the norm, the conjugate and the inverse. In the following definitions, $\mathcal{A}$, $\mathcal{B}$ and $\mathcal{C}$ are three quaternions.

C.1.1 Product

As for matrix multiplication, the product of two quaternions is associative but non-commutative [77].

$$\begin{aligned} \mathcal{A}(\mathcal{B}\mathcal{C}) &= (\mathcal{A}\mathcal{B})\,\mathcal{C} \\ \mathcal{A}\mathcal{B} &\neq \mathcal{B}\mathcal{A} \end{aligned} \tag{C.1}$$

The product is performed as followed:

$$\mathcal{A}\mathcal{B} = [\![a, \vec{A}]\!][\![b, \vec{B}]\!] = [\![ab - \vec{A} \bullet \vec{B}, a\vec{B} + b\vec{A} + \vec{A} \times \vec{B}]\!] \tag{C.2}$$

where "$\bullet$" indicates a dot product and "$\times$" the cross product between two vectors.

C.1.2 Norm

The norm (also known as the magnitude) is calculated by the square root of the sum of the coefficients squared:

$$\|\mathcal{A}\| = \sqrt{a^2 + A_x^2 + A_y^2 + A_z^2} \tag{C.3}$$

As for complex numbers, the norm can also be calculated by the multiplication of a quaternion and its conjugate.

$$\|\mathcal{A}\| = \mathcal{A}\mathcal{A}^* \tag{C.4}$$

C.1.3 Conjugate

The conjugate is defined by the negation of the vector part (complex dimensions) of the quaternion.

$$\mathcal{A}^* = [\![a, -\vec{A}]\!] \tag{C.5}$$

C.1.4 Inverse

The inverse of a quaternion is its conjugate divided by the square of its norm.

$$\mathcal{A}^{-1} = \frac{\mathcal{A}^*}{\|\mathcal{A}\|^2} \tag{C.6}$$

C.2 Rotation Operations

To represent a rotation a quaternion must be a unit quaternion; its norm must be equal to unity [77]. This implies that the conjugate and the inverse are equivalent operations. Furthermore, for any given rotation (except the identity rotation), two quaternions can represent the same rotation [79]. This is analogous to the clockwise and counter-clockwise rotations in two dimensions. In the case of quaternions, these two representations are referred to the positive and negative rotations. A positive quaternion is defined as a quaternion where the first non-zero coefficient is positive (i.e. greater than 0). Unless specified, only positive quaternions are considered in EBSD-Image to simplify the calculations. Note that the transformation of a quaternion to a positive quaternion is different than taking its conjugate; the sign of all four coefficients are changed instead of only the complex coefficients. For the purpose of EBSD-Image, four types of operation are performed on rotations: (i) combination of rotations (ii) change of reference frame (iii) misorientation (iv) rotation of a vector.

C.2.1 Combination of Rotations

For two successive rotations $\mathcal{A}$ and $\mathcal{B}$, the resultant rotation $\mathcal{C}$ is equal to the multiplication of the two quaternions. The order of the multiplication depends if the resultant rotation is expressed in the reference frame of the rotation object (Equation C.7) or in the absolute reference frame (Equation C.8) [79, 80].

$$\mathcal{C} = \mathcal{A}\mathcal{B} \tag{C.7}$$

$$\mathcal{C} = \mathcal{B}\mathcal{A} \tag{C.8}$$

C.2.2 Change of Reference Frame

Another typical operation is to change the reference frame in which a rotation is given. Let $\mathcal{Q}$ be the rotation from the old to the new reference frame. A rotation $\mathcal{A}$ given in the old reference frame can be expressed in the new reference frame as follow:

$$\mathcal{A}' = \mathcal{Q}^{-1}\mathcal{A} \tag{C.9}$$

Consequently from Equation C.9, the rotation $\mathcal{Q}$ between the old reference frame $\mathcal{Q}_1$ and the new reference frame $\mathcal{Q}_2$ is:

$$\mathcal{Q} = \mathcal{Q}_1^{-1}\mathcal{Q}_2 \tag{C.10}$$

C.2.3 Misorientation

By definition, the misorientation corresponds to the rotation between two reference frames [81]. For a crystal, its symmetry must be considered to find the smallest misorientation angle between two rotations, the disorientation [81, 82]. The crystal symmetry brings a rotation in the crystal's fundamental zone and reduces the possible disorientation angles. For example, the maximum disorientation between two cubic crystals is 62.8° [81]. For a set of symmetry operators $\mathcal{O}_c$, the misorientation is given as

$$\mathcal{Q} = \left(\mathcal{Q}_1\mathcal{O}_c\right)^{-1}\mathcal{Q}_2\mathcal{O}_c \tag{C.11}$$

and the disorientation θ as

$$\theta = 2\arccos\left(a\right) \tag{C.12}$$

where a is the real scalar coefficient of the quaternion $\mathcal{Q}$ [81].

C.2.4 Vector Rotation

Finally, quaternions can be used to rotate a vector in 3D space. For this operation, the vector $\vec{v}$ is converted to a pure quaternion $\mathcal{V} = [\![0, \vec{v}]\!]$ (the real scalar number is zero and the complex coefficients correspond to the components of the vector). This new quaternion is then respectively pre and post-multiplied by the rotation quaternion and its conjugate [77]. Let $\mathcal{A}$ be the rotation quaternion and $\mathcal{V}'$ the result of the rotation. The rotated vector is the complex part of the $\mathcal{V}'$ quaternion.

$$\mathcal{V}' = \mathcal{A}\mathcal{V}\mathcal{A}^* \tag{C.13}$$

From a computational point of view, quaternions require less operations than matrices for combining rotations, changing reference frame and finding misorientation. However, vector rotation is more efficient with matrices.

C.3 Conversion

The conversion methods are centered around the quaternion as it is the default representation of EBSD-Image. In other words, to convert from Euler angles to a rotation matrix, the Euler angles must be converted to a quaternion and then to a rotation matrix.

C.3.1 Euler Angles

The Bunge convention is used for the Euler angles. Equation C.14 gives the definition of the four quaternion coefficients from the three Euler angles (θ_1, θ_2, θ_3). To simplify the notation c_i and s_i signify respectively the cosine and the sine of the angle θ_i.

$$\begin{aligned} a &= c_1c_2c_3 - s_1c_2s_3 \\ A_x &= c_1s_2c_3 + s_1s_2s_3 \\ A_y &= c_1s_2s_3 - s_1s_2c_3 \\ A_z &= c_1c_2s_3 + s_1c_2c_3 \end{aligned} \tag{C.14}$$

Due to the singularity at $\theta_2 = 0$ or π, three cases exists for the conversion of a quaternion to Euler angles.

1. $\theta_2 = 0$ (i.e. $A_x = A_y = 0$)

$$\begin{aligned} \theta_1 &= 2\arctan\left(\frac{A_z}{a}\right) \\ \theta_2 &= 0 \\ \theta_3 &= 0 \end{aligned} \tag{C.15}$$

2. $\theta_2 = \pi$ (i.e. $A_x^2 + A_y^2 = 1$)

$$\begin{aligned} \theta_1 &= 2\arctan\left(\frac{A_y}{A_x}\right) \\ \theta_2 &= \pi \\ \theta_3 &= 0 \end{aligned} \tag{C.16}$$

3. $0 < \theta_2 < \pi$

$$\begin{aligned} \theta_1 &= \arctan\left(\frac{A_x A_z - A_y a}{A_y A_z + A_x a}\right) \\ \theta_2 &= \arccos\left(1 - 2A_x^2 - A_y^2\right) \\ \theta_3 &= \arctan\left(\frac{A_x A_z + A_y a}{A_x a - A_y A_z}\right) \end{aligned} \tag{C.17}$$

C.3.2 Axis-Angle

The conversion of the axis-angle representation $(\phi, \vec{n})$ is straightforward since both are closely related [79].

$$(\phi, \vec{n}) \rightarrow [\![\cos\frac{1}{2}\phi, \frac{\sin\frac{1}{2}\phi}{\|\vec{n}\|}\vec{n}]\!] \tag{C.18}$$

To convert a quaternion to an axis-angle, the angle is calculated by taking the arccosine of the scalar value and the complex vector of the quaternion:

$$\begin{aligned} \phi &= 2\arccos a \\ \vec{n} &= \frac{1}{d}\vec{A} \end{aligned} \tag{C.19}$$

where d is equal to $\sqrt{1-a^2}$. If d is equal to zero, the vector $\vec{A}$ is the axis.

C.3.3 Matrix

A matrix that represents a rotation is a special kind of 3x3 matrix. Rotation matrices form the special orthogonal group (SO3) which implies that: (i) the transpose and inverse are equal ($M^T = M^{-1}$) (ii) the determinant is equal to 1.

To convert a rotation matrix to a quaternion, the method proposed by Morawiec and implemented in orientation library, Orilib, by Quey is used. The elements of the matrix are referred by their indices ij in the following equations, where i is the row position and j the column position. The position varies from 0 to 2. The first step of the conversion is to calculate the scalar coefficient of the quaternion using Equation C.20.

$$a = \frac{\sqrt{m_{00} + m_{11} + m_{22} + 1)}}{2} \tag{C.20}$$

If a is different than zero, the complex coefficients of the quaternion are calculated as follow:

$$\begin{aligned} A_x &= \frac{m_{12} - m_{21}}{4a} \\ A_y &= \frac{m_{20} - m_{02}}{4a} \\ A_z &= \frac{m_{01} - m_{10}}{4a} \end{aligned} \tag{C.21}$$

On the other hand, if a is equal to zero, the latter equation is undetermined due to the division by zero. The absolute value of quaternion coefficients is given by Equation C.22.

$$\begin{aligned} A_x &= \frac{m_{00} + 1}{2} \\ A_y &= \frac{m_{11} + 1}{2} \\ A_z &= \frac{m_{22} + 1}{2} \end{aligned} \tag{C.22}$$

The sign of the coefficients depends on the sign of a specific element in the matrix. The following procedure explains how the latter is found. First, the complex coefficients of the quaternion are assigned an index i: 0 for A_x, 1 for A_y, and 2 for A_z. Then, the index of the coefficient with the maximum value is assigned to the variable s. With this information, the sign of the coefficient i is equal to the sign of the matrix element located in row i and column s, unless i is equal to s. In other words, the latter exception implies that the sign of the coefficient with the maximum value is never changed. For example, let consider a situation where s is equal to 1 (i.e. A_y is the maximum coefficient). The sign of the coefficient A_x is therefore equal to the sign of the matrix element m_{01}, the sign of A_y is positive and the sign of A_z is equal to the sign of m_{21}.

The conversion of a quaternion to a special orthogonal matrix is simpler as shown in

Equation C.23.

$$\begin{aligned}
m_{11} &= a^2 + A_x^2 - A_y^2 - A_z^2 \\
m_{12} &= 2(A_x A_y + a A_z) \\
m_{13} &= 2(A_x A_z - a A_y) \\
m_{21} &= 2(A_x A_y - a A_z) \\
m_{22} &= a^2 - A_x^2 + A_y^2 - A_z^2 \\
m_{23} &= 2(A_y A_z + a A_x) \\
m_{31} &= 2(A_x A_z + a A_y) \\
m_{32} &= 2(A_y A_z - a A_x) \\
m_{33} &= a^2 - A_x^2 - A_y^2 + A_z^2
\end{aligned} \tag{C.23}$$

Bibliography

[1] Stefan Zaefferer. On the formation mechanisms, spatial resolution and intensity of backscatter Kikuchi patterns. *Ultramicroscopy*, 107(2-3):254–266, 2007. doi: 10.1016/j.ultramic.2006.08.007.

[2] Niels-Henrik Schmidt and Niels O. Olesen. Computer-aided determination of crystal-lattice orientation from electron-channeling patterns in the SEM. *Canadian Mineralogist*, 27:15–22, 1989.

[3] Niels C. Krieger Lassen. *Automated determination of crystal orientations from electron backscattering patterns*. PhD thesis, The Technical Univsersity of Denmark, 1994.

[4] Stuart I. Wright. *Individual lattice orientation measurements development and application of a fully automatic technique*. PhD thesis, Yale University, 1992.

[5] Robert A. Schwarzer, David P. Field, Brent L. Adams, Mukul Kumar, and Adam J. Schwartz. *Present state of electron backscatter diffraction and prospective developements*, chapter 1, pages 1–20. Springer, New York, 2nd edition, 2009. ISBN 978-0-387-88135-5.

[6] I. Brough and F. J. Humphreys. Evaluation and application of a fast EBSD detector. *Materials Science and Technology*, 26(6):636–639, 2010. doi: 10.1179/026708309X12468927349415.

[7] R. A. Schwarzer and J. Hjelen. Orientation microscopy with fast EBSD. *Materials Science and Technology*, 26(6):646–649, 2010. doi: 10.1179/026708309X12512842324515.

[8] Xiadong Tao. *An EBSD study on mapping of small orientation differences in lattice mismatched heterostructures*. PhD thesis, Lehigh University, 2003.

[9] Robert A. Schwarzer. Automated crystal lattice orientation mapping using a computer-controlled SEM. *Micron*, 28(3):249–265, 1997. doi: 10.1016/S0968-4328(97)00010-3.

[10] David B. Williams and C. Barry Carter. *Transmission Electron Microscopy: A Textbook for Materials Science*. Springer, New York, 2nd edition, 2009. ISBN 0-306-45274-2.

[11] Angus J. Wilkinson and Peter B. Hirsch. Electron diffraction based techniques in scanning electron microscopy of bulk materials. *Micron*, 28(4):279–308, 1997. doi: 10.1016/S0968-4328(97)00032-2.

[12] Aimo Winkelmann. *Dynamical simulation of electron backscatter diffraction patterns*, chapter 2, pages 21–33. Springer, New York, 2009. ISBN 978-0-387-88135-5.

[13] Adam J. Schwartz, Mukul Kumar, Brent L. Adams, and David P. Field, editors. *Electron backscatter diffraction in materials science*. Springer, New York, 2nd edition, 2009. ISBN 978-0-387-88135-5.

[14] Rafael C. Gonzalez and Richard Eugene Woods. *Digital image processing*. Prentice Hall, Upper Saddle River, third edition, 2007. ISBN 9780131687288.

[15] P. V. C. Hough. A method and means for recognizing complex patterns. U.S. Patent No. 3,069,654, 1962.

[16] R. O Duda and P. E. Hart. Use of hough transform to detect lines and curves in picture. *Communications of the ACM*, 15(1):11–15, 1972. doi: 10.1145/361237.361242.

[17] J. Radon. Uber die bestimmung von funktionen durch ihre integralwerte langs gewisser mannigfaltigkeiten. *Reports on the proceedings of the Saxony Academy of Science*, 69:262–277, 1917.

[18] Stanley R. Deans. *The Radon transform and some of its applications*. Wiley, New York, 1983. ISBN 0894647180.

[19] M. Boisen and G. V. Gibbs. *Mathematical crystallography (Reviews in mineralogy)*. Mineralogical Society of America, Chantilly, 15th edition, 1990. ISBN 978-0939950263.

[20] EDAX TSL, 2010. URL `http://www.edax.com/products/tsl.cfm`. [Online; accessed 10-September-2010].

[21] *Channel 5*. Oxford Instruments HKL Technology, 2010. User manual.

[22] Angus J. Wilkinson and David J. Dingley. Quantitative deformation studies using electron backscatter patterns. *Acta Metallurgica et Materialia*, 39(12):3047–3055, 1991. doi: 10.1016/0956-7151(91)90037-2.

[23] R. R. Keller, A. Roshko, R. H. Geiss, K. A. Bertness, and T. P. Quinn. EBSD measurement of strains in GaAs due to oxidation of buried AlGaAs layers. *Microelectronic Engineering*, 75(1):96–102, 2004. doi: 10.1016/j.mee.2003.11.010.

[24] L. Ryde. Application of EBSD to analysis of microstructure in commercial steels. *Materials Science and Technology*, 22(11):1297–1306, 2006. doi: 10.1179/174328406X130948.

[25] Roumen Petrov, Leo Kestens, Anna Wasilkowska, and Yvan Houbaert. Microstructure and texture of a lightly deformed TRIP-assisted steel characterized by means of the EBSD technique. *Materials Science and Engineering A*, 447(1-2):285–297, February 2007. doi: 10.1016/j.msea.2006.10.023.

[26] Jinghui Wu, Peter J. Wray, Calixto I. Garcia, Mingjian Hua, and Anthony J. Deardo. Image quality analysis: A new method of characterizing microstructures. *ISIJ International*, 45(2):254–262, 2005. doi: 10.2355/isijinternational.45.254.

[27] P. J. Szabó and I. Szalai. Effect of monotonic and cyclic deformation on the IQ-maps of austenitic stainless steel. *Materials Science Forum*, 473-474:267–272, 2005. doi: 10.4028/www.scientific.net/MSF.473-474.267.

[28] Stuart I. Wright and Matthew M. Nowell. EBSD image quality mapping. *Microscopy & Microanalysis*, 12(1):72–84, 2006. doi: 10.1017/S1431927606060090.

[29] C. E. Shannon. A mathematical theory of communication. *The Bell System technical journal*, 27:379–423, 1948.

[30] J. Frank and L. Al-Ali. Signal-to-noise ratio of electron micrographs obtained by cross correlation. *Nature*, 256:376–379, July 1975. doi: 10.1038/256376a0.

[31] David C. Joy. SMART - a program to measure SEM resolution and imaging performance. *Journal of Microscopy*, 208(1):24–34, 2002. doi: 10.1046/j.1365-2818.2002.01062.x.

[32] K. Kunze, S. I. Wright, Brent L. Adams, and David J. Dingley. Advances in automatic EBSP single orientation measurements. *Textures and Microstructures*, 20 (1-4):41–54, 1993. doi: 10.1155/TSM.20.41.

[33] Oxford Instruments. Electron back-scattered diffraction explained. Technical report, Oxford Instruments Analytical, 2004.

[34] Niels-Henrik Schmidt. personal communication, 2010.

[35] F. J. Humphreys. Characterisation of fine-scale microstructures by electron backscatter diffraction (EBSD). *Scripta Materialia*, 51(8):771–776, 2004. doi: 10.1016/j.scriptamat.2004.05.016.

[36] H. Hielscher and Helmut Schaeben. A novel pole figure inversion method: specification of the MTEX algorithm. *Journal of Applied Crystallography*, 41(6):1024–1037, 2008. doi: 10.1107/S0021889808030112.

[37] Cyril Cayron. ARPGE: a computer program to automatically reconstruct the parent grains from electron backscatter diffraction data. *Journal of Applied Crystallography*, 40(6):1183–1188, 2007. doi: 10.1107/S0021889807048777.

[38] Angus J. Wilkinson, Graham Meaden, and David J. Dingley. High-resolution elastic strain measurement from electron backscatter diffraction patterns: New levels of sensitivity. *Ultramicroscopy*, 106(4-5):307–313, 2006. doi: 10.1016/j.ultramic.2005.10.001.

[39] Werner Massa. *Crystal structure determination*. Springer, New York, 2nd edition, 2004. ISBN 978-3540206446.

[40] Aimo Winkelmann, Carol Trager-Cowan, Francis Sweeney, Austin P. Day, and Peter Parbrookd. Many-beam dynamical simulation of electron backscatter diffraction patterns. *Ultramicroscopy*, 107(4-5):414–421, 2007. doi: 10.1016/j.ultramic.2006.10.006.

[41] J. Painter and E. A. Merritt. mmLib Python toolkit for manipulating annotated structural models of biological macromolecules. *Journal of Applied Crystallography*, 37(1):174–178, 2004. doi: 10.1107/S0021889803025639.

[42] E. Prince, editor. *Mathematical, physical and chemical tables*, volume C of *International Tables for Crystallography*. Wiley, New York, 3rd edition, 2004. ISBN 978-1-4020-1900-5.

[43] Eric W. Weisstein. Point-line distance–3-dimensional. MathWorld–A Wolfram Web Resource, 2010. URL `http://mathworld.wolfram.com/Point-LineDistance3-Dimensional.html`. [Online; accessed 2-September-2010].

[44] Saulius Gražulis, Daniel Chateigner, Robert T. Downs, A. F. T. Yokochi, Miguel Quirós, Luca Lutterotti, Elena Manakova, Justas Butkus, Peter Moeck, and Armel Le Bail. Crystallography open database – an open-access collection of crystal structures. *Journal of Applied Crystallography*, 42(4):726–729, 2009. doi: 10.1107/s0021889809016690.

[45] Robert T. Downs and M. Hall-Wallace. The American mineralogist crystal structure database. *American Mineralogist*, 88(1):247–250, 2003.

[46] J. Gruber. Introduction to group theory and rotations in microstructural analysis. Lecture notes from 27-750 course at Carnegie Mellon University, 2007. URL `http://neon.materials.cmu.edu/rollett/27750/lecture2.pdf`.

[47] Wilson C. Y. Lam, Lam T. S. Lam, Kelvin S. Y. Yuen, and Dennis N. K. Leung. An analysis on quantizing the hough space. *Pattern Recognition Letters*, 15(11): 1127–1135, 1994. doi: 10.1016/0167-8655(94)90128-7.

[48] Robert H. Dodier. *Unified prediction and diagnosis in engineering systems by means of distributed belief network*. PhD thesis, University of Colorado, 1999.

[49] Robert Piessens, Elise deDoncker-Kapenga deDoncker Kapenga, Christian Ueberhuber, and David Kahaner. *QUADPACK: a subroutine package for automatic integration*. Springer, New York, 1983. ISBN 3540125531.

[50] J. Kittler and J. Illingworth. Minimum error thresholding. *Pattern Recognition*, 19 (1):41–47, 1986. doi: 10.1016/0031-3203(86)90030-0.

[51] J. N. Kapur, P. K. Sahoo, and A. K. C. Wong. A new method for gray level picture thresholding using the entropy of the histogram. *Computer Vision, Graphics, and Image Processing*, 29(3):273–285, 1985. doi: 10.1016/0734-189X(85)90125-2.

[52] Niels C. Krieger Lassen. Automatic high-precision measurements of the location and width of Kikuchi bands in electron backscatter diffraction patterns. *Journal of Microscopy*, 190(3):375–391, 1998. doi: 10.1046/j.1365-2818.1998.00330.x.

[53] G. D. Moan and P. Rudling, editors. *Zirconium in the nuclear industry*, West Conshohocken, 2002. ASTM International. ISBN 978-0-8031-2895-8.

[54] R. A. Holt, G. A. Bickel, and N. Christodoulou. Effect of fast neutron fluence on the creep anisotropy of Zr-2.5Nb tubes. *Journal of Nuclear Materials*, 373(1-3):130–136, 2008. doi: 10.1016/j.jnucmat.2007.05.033.

[55] M. Griffiths, R. A. Holt, J. Li, and S. Salmoto. Microtexture analysis of Zr-2.5Nb pressure tubing. *Microstructural Science*, 26:293–302, 1998.

[56] L. N. Brewer and J. R. Michael. Risks of cleaning electron backscatter diffraction data. *Microscopy Today*, 18(02):10–15, 2010. doi: 10.1017/S1551929510000040.

[57] Pierre Hovington, P. T. Pinard, M. Lagacé, L. Rodrigue, R. Gauvin, and M. L. Trudeau. Towards a more comprehensive microstructural analysis of Zr-2.5Nb pressure tubing using image analysis and electron backscattered diffraction (EBSD). *Journal of Nuclear Materials*, 393(1):162–174, 2009. doi: 10.1016/j.jnucmat.2009.05.017.

[58] George Vander Voort. *Metallography, principles and practice*. ASM International, Materials Park, 1999. ISBN 0-87170-672-5.

[59] L. E. Samuels. *Metallographic polishing*. ASM International, Materials Park, 4th edition, 2003. ISBN 0-87170-779-9.

[60] D. M. Turley and E. D. Doyle. On the art of cutting metals - 75 years later. In L. Kope and S. V. Ramalingan, editors, *Winter Annual Meeting of the American Society of Mechanical Engineers*, page 85, New York, 1982. American Society of Mechanical Engineers.

[61] L. N. Brewer, M. A. Othon, L. M. Young, and T. M. Angeliu. Misorientation mapping for visualization of plastic deformation via electron back-scattered diffraction. *Microscopy & Microanalysis*, 12(1):85–91, 2006. doi: 10.1017/S1431927606060120.

[62] E. M. Lehockey, Y. Lin, and O. E. Lepik. *Mapping residual plastic strain in materials using electron backscatter diffraction*, chapter 20. Springer, New York, 2000. ISBN 978-0306464874.

[63] Masayuki Kamaya, Angus J. Wilkinson, and John M. Titchmarsh. Quantification of plastic strain of stainless steel and nickel alloy by electron backscatter diffraction. *Acta Materialia*, 54(2):539–548, 2006. doi: 10.1016/j.actamat.2005.08.046.

[64] G. Vander Voort and William Van Geertruyden. Specimen preparation for electron backscattered diffraction. Technical report, Buehler Ltd., 2006.

[65] MatWeb – Material property data, 2010. URL `http://www.matweb.com`. [Online; accessed 29-September-2010].

[66] Joseph I. Goldstein, Dale E. Newbury, David C. Joy, Charles E. Lyman, Patrick Echlin, Eric Lifshin, Linda Sawyer, and J. R. Michael. *Scanning electron microscopy and X-ray microanalysis*. Springer, New York, 3rd edition, 2003. ISBN 978-0306472923.

[67] S. X. Ren, E. A. Kenik, K. B. Alexander, and A. Goyal. Exploring spatial resolution in electron back-scattered diffraction experiments via Monte Carlo simulation. *Microscopy and Microanalysis*, 4(1):15–22, 1998. doi: 10.1017/S1431927698980011.

[68] Andrew Deal, Tejpal Hooghan, and Alwyn Eades. Energy-filtered electron backscatter diffraction. *Ultramicroscopy*, 108(2):116–125, 2008. doi: 10.1016/j.ultramic.2007.03.010.

[69] F. J. Humphreys. Grain and subgrain characterisation by electron backscatter diffraction. *Journal of Material Science*, 36(16):3833–3854, 2001. doi: 10.1023/A:1017973432592.

[70] David J. Dingley. Progressive steps in the development of electron backscatter diffraction and orientation imaging microscopy. *Journal of Microscopy*, 213(3):214–224, 2004. doi: 10.1111/j.0022-2720.2004.01321.x.

[71] Thomas C. Isabell and Vinayak P. Dravid. Resolution and sensitivity of electron backscattered diffraction in a cold field emission gun SEM. *Ultramicroscopy*, 67(1-4):59–68, 1997. ISSN 0304-3991. doi: 10.1016/s0304-3991(97)00003-x.

[72] C J Harland, P Akhter, and J A Venables. Accurate microcrystallography at high spatial resolution using electron back-scattering patterns in a field emission gun scanning electron microscope. *Journal of Physics E: Scientific Instruments*, 14(2):175, 1981. doi: 10.1088/0022-3735/14/2/011.

[73] J. Hjelen and E. Nes. Spatial resolution measurements of electron backscatter diffraction. In *12th International Congress on Electron Microscopy*, pages 404–405, San Francisco, 1990. San Francisco Press.

[74] P. S. Bate, R. D. Knutsen, I. Brough, and F. J. Humphreys. The characterization of low-angle boundaries by EBSD. *Journal of Microscopy*, 220(1):36–46, 2005. doi: 10.1111/j.1365-2818.2005.01513.x.

[75] Bruker QUANTAX EBSD CrystAlign, 2010. URL `http://www.bruker-axs.de/crystalign-ebsd.html`. [Online; accessed 10-September-2010].

[76] David J. Dingley and Stuart I. Wright. Determination of crystal phase from an electron backscatter diffraction pattern. *Journal of Applied Crystallography*, 42(2): 1–8, 2009. doi: 10.1107/S0021889809001654.

[77] Simon L. Altmann. *Rotations, quaternions, and double groups*. Oxford University Press, Oxford, 1986. ISBN 978-0198553724.

[78] Wikipedia. Quaternions and spatial rotation — Wikipedia, The Free Encyclopedia, 2010. URL `http://en.wikipedia.org/w/index.php?title=Quaternions_and_spatial_rotation&oldid=357495304`. [Online; accessed 9-May-2010].

[79] Martin Baker. Euclidean space, 2008. URL `http://www.euclideansplace.com`.

[80] Romain Quey. *Orientation Library: A collection of routines for orientation manipulation (Version 2.0)*, 2008. URL `http://sourceforge.net/projects/orilib`.

[81] A. D. Rollett. Texture, microstructure & anisotropy. Lecture notes from 27-750 course at Carnegie Mellon University, 2009. URL `http://neon.materials.cmu.edu/rollett/27750/27750.html`.

[82] U. F. Kocks, C. N. Tomé, and H.-R. Wenk. *Texture and anisotropy*. Cambridge University Press, Cambridge, 1998. ISBN 0-521-46516-8.